Imperial College
London

A New Approach to the Fault Location Problem: Using the Fault's Transient Intermediate Frequency Response

Nicolás Cifuentes Otto

Submitted in partial fulfillment of the requirements for the degree of
Doctor of Philosophy
July 2021

Imperial College of Science, Technology and Medicine
Department of Electrical and Electronic Engineering
Control and Power Research Group

Statement of originality and Copyright Declaration

I hereby declare that this work is the result of my own endeavour, and that any ideas or quotations from the work of other people, published or otherwise, are appropriately referenced.

Nicolás Cifuentes Otto
Department of Electrical and Electronic Engineering
Imperial College London, London, U.K.
November 9, 2021

Abstract

The fault location problem has been tackled mainly through impedance-based techniques, the travelling wave principle and more recently by machine learning algorithms. These techniques require both current and voltage measurements. In the case of impedance-based methods they can provide multiples solutions. In the case of the travelling wave approach it usually requires high sampling and synchronized frequency measurements together with sophisticated identification algorithms. Machine learning techniques require training data and re-tuning for different grid topologies. In this work we propose a new fault location method based on the fault's transient intermediate frequency response of the system immediately after a fault occurs.

The transient response immediately after the occurrence of a fault is characterized by the travelling wave phenomenon together with intermediate frequencies of oscillation in the range of 5 to 500 kHz. These intermediate frequencies of oscillations are associated with the natural response of the cable/line system to the fault event. Their frequencies of oscillation are dependent on the faulted section and the fault location within that section. The proposed fault location methodology aims to leverage on that dependency, by firstly identifying these intermediate frequencies for different fault location scenarios for a given network. This process is performed offline using a linear time invariant (LTI) representation of the network. To compute this LTI representation, as part of this work an impedance representation in the modal domain is established for cable/line sections, which is able to capture the frequency-dependence and distributed nature of its electrical parameters. The offline methodology identifies these intermediate frequencies for different fault location scenarios, and then proceeds to fit the fault location dependence of each intermediate frequency using a polynomial regression.

An online methodology is also proposed to perform the fault location in real time by solving the polynomial regressions computed during the offline methodology using measurements of the intermediate frequencies present in the frequency spectrum of transient signals. The fault location is thus solved by using voltage or current measurements of the fault's transient response at different locations in the network, together with simple signal processing techniques such as the Fast Fourier Transform. The full method is tested with an EMT simulation in PSCAD, using the detailed frequency dependent model for underground cables, together with realistic load models in a low voltage distribution network test system.

Acknowledgements

I would like to start by thanking Professor Bikash C. Pal for giving me the opportunity to pursue my PhD with him at Imperial College, for his supportive words of encouragement throughout this process and for believing in my skills to complete my postgraduate journey.

Since the beginning, the PhD has been full of interesting and sometime dreadful challenges; moving to a new country 11.653 kilometers away from home, making a great group of friends and having the certainty to fail on coming up with a new fault location methodology. In every one of these steps, my family has always been there to support me, to celebrate with me every small achievement and to reassure me in the face of difficult moments. I will be forever grateful for all that unconditional support Mom, Dad and Moni.

Before arriving to London, I was concerned that the PhD journey would be a lonely and isolating one, after saying goodbye to so many friends and loved ones at the airport. Little did I know I would meet some of the best people and friends I could have asked for; certainly one, if not the, best experience of the entire postgraduate challenge. For your friendship, support, pints and travels together I will always be thankful Eva, Luca, Jochen, Marc, Alex, Caspar, Ankur, Diptargha, Thiago, Joel, Alberto, Anastasis, Eugenie, Michael, James and Luis. I also need to thank the CAP group, particularly, Firdous, Stratis, Jerôme, Kevin together with the other members of the group for always being supportive, creating a welcoming environment during this process.

I also need to thank my fellow wardens at Wilkinson Hall, Matina, Charlie and Eve for their help, support and friendship in one the most unexpected yet maturing experience over the last three years.

Finally, the biggest reward of this entire process was having the chance to meet you Clara, the best partner I could have asked for. This Thesis would not have been possible without your unconditional support and care. Thanks for reminding me of the good things in life, for that necessary enthusiasm and optimism when faced against uncertainty, for always being there even when the rest of the world seems unreachable during a Pandemic.

List of Abbreviations

ANN	Artificial Neural Network
AVR	Automatic Voltage Regulator
CIs	Customer Interruptions
CIG	Converter Interfaced Generation
CMLs	Customer Minutes Lost
CWT	Continuous Wavelet Transform
DG	Distributed Generation
DNO	Distribution Network Operator
DWT	Discrete Wavelet Transform
ELM	Extreme Learning Machine
EMT	Electromagnetic Transient
ERLM	Exponential Recovery Load Model
FFT	Fast Fourier Transform
FRT	Fault Ride Through
HIF	High Impedance Fault
HV	High Voltage
LTI	Linear Time Invariant
LV	Low Voltage
MMC	Modular Multilevel Converter
MV	Medium Voltage
PCC	Point of Common Coupling
pdf	probability density function
PLL	Phase Locked-Loop
PMU	Phasor Measurement Unit
PV	Photovoltaic
PWM	Pulse Width Modulation
SCR	Short-Circuit Ratio
SVM	Support Vector Machine
TSO	Transmission System Operator
ULM	Universal Line Model
VSC	Voltage Source Converter

Contents

List of Tables

List of Figures

CHAPTER 1

Introduction

1.1 Context and Motivation

In today's distribution networks, power supply must comply with each country's quality of service normative. These normative are set to ensure the continuity of supply to final customers and to guarantee standards of performance meant to protect them. In the case of the UK, these normative are set in the statutory regulations *"The Electricity (Standards of Performance) Regulations 2015"*, which allow customers to claim compensation fees from the distribution network operators (DNO) after suffering power supply interruptions that last over regulated periods of time [1]. In distribution networks, these power supply interruptions are caused in 80% of cases because of fault events in the distribution grid [2–4]. In the occurrence of a fault event, the conventional outage management system followed by DNOs to restore power supply can last from tens of minutes to hours [2]. With the aim to reduce the restoration time and improve distribution network's reliability, an Interruptions Incentive Scheme (IIS) has been implemented in the new RIIO-ED1 electricity distribution price control framework developed by The Office of Gas and Electricity Markets (Ofgem) [5]. In the IIS model the reliability of different distribution network operators is measured using the number of customer interruptions (CIs) per 100 customers, as well as the average customer minutes lost (CMLs) due to unexpected fault events. The CMLs scored by DNOs across the UK according to the *"RIIO electricity distribution annual report 2016-17"* published by Ofgem [6] is shown in Figure 1.1. As can be seen in the map, the longest power supply interruptions currently last on average an hour in the Scottish Hydro Electric Power Distribution network, while customers in the city of London experience the shortest interruptions that last around 20 minutes [6].

Today's supply interruption times are the result of an improvement trend in DNOs' performance over the last years. This trend can be seen in Figure 1.2, where the CML reliability index evolution is plotted for UK's DNOs [7]. According to [7], since 2010 the duration of power supply interruptions in distribution networks across the UK has seen a significant 40% drop, with an initial national average of an hour in 2010 to 35 minutes in 2016. This time reduction has been partially achieved because of the Interruption Incentive Scheme which seeks to promote improvements in the reliability of DNOs. More specifically, DNOs can receive addi-

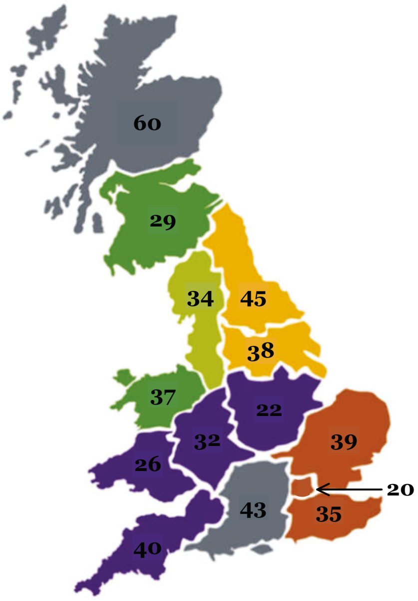

Figure 1.1: Customer minutes lost over the UK in 2016.

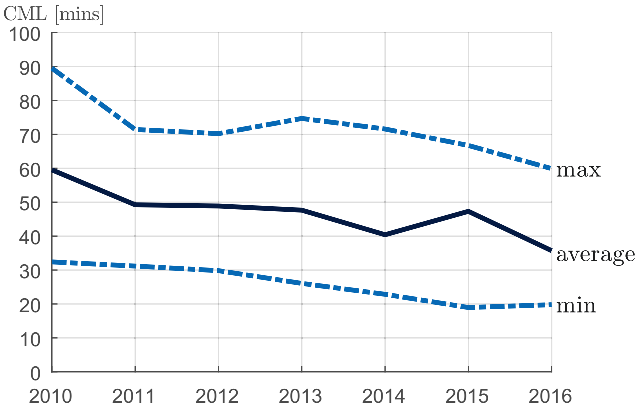

Figure 1.2: Evolution of interruption's duration in the last years.

tional revenue or pay penalties defined as 1.2 cents per CI together with 1.8 cents for CML [8]. This interruption incentive scheme translated in an extra £m 160 for all DNOs in 2016, with a maximum additional gain of £m 21.6 in the case of the Eastern Power Network equivalent to 3.8% of its allowed revenue [6].

The previous numbers are a clear sign of the current importance given to improving DNO's outage management system, which can be done according to the Ofgem's 2016 annual report with investments in both distribution assets to reinforce the network and in operational practices: *"[...] Investment in network assets can reduce the number of customer interruptions (CIs), and improvements to operational practices (such as fault location and repair) can reduce customer minutes lost (CMLs). [...]"* [6]. Unfortunately, this approach has a foreseeable limit once additional investments in distribution assets and operational practices start having a negligible improvement in reliability, compared to the additional cost transferred to final customers. Despite this financial limit, the time delay that takes to identify faulted sections in the distribution grid can be further reduced by following a different approach. Usually, fault location is done by visual inspection by repair crews in overhead lines, or by trial and error switching of different network sections in the case of underground cables [2, 3]. To shorten this interruption delay, instead of furthering more investments in operational practices such as incorporating additional repair crews, it is possible to implement fault location methodologies that use data obtained from measurements devices spread across the network.

This alternative using centralized fault location methodologies based on measurements has been researched at least since the 70's [9], and remains an important topic for distribution grid's restoration [10]. Since then, the fault location research field working on centralised algorithmic solutions clustered in three dominant areas [11–13]: Impedance-based solutions [14–19], Travelling wave approaches [20–25] and Machine learning algorithms [26–29]. An extensive review of each methodology is provided in [11–13]. Given the ever-evolving and diverse characteristics of current HV and MV networks, fifty years on there is still no universal agreement for a truly applicable and reliable solution. This is evident in the fact that there are currently no centralised fault location methodologies available in transmission or distribution grid protections [11–13]. As such, there is still ongoing research to improve each technique into a reliable and applicable methodology [30–32].

The first category of impedance-based solutions employs the fundamental frequency behaviour of the grid's currents and voltages during a fault event [11–13]. By using RMS measurements of the voltages and currents, it is possible to compute the grid's apparent impedance as seen from the measuring location. If the network's topology is known together with the per-unit impedance of each feeder, then it is possible to define a set of algebraic equations to match the measured impedance to the expected one having the fault location as the unknown variable. The solutions to this set of algebraic equations are thus dependent on the measurement location, the fault location and also the fault impedance [11–13]. This approach is limited by two main factors. First, it is necessary to estimate the fault impedance to solve the system of equations. Secondly, depending on the number of available measurements and on their locations, the set of algebraic equations can have multiple fault location solutions [11–13].

Regarding travelling wave approaches (also known as transient-based approaches) to the fault location problem, they rely on high-frequency measurements. More specifically, immediately after a fault occurs, pulse-like signals will start propagating from the fault and throughout the system. These pulse waves propagate at a constant speed which is defined by the electrical parameters of the lines and cables, and it is usually around 60% to 90% of the speed of light [11–13]. Examples of recent works using this approach can be found in [33–35]. On their propagation, each wave will experience reflection and refraction at each discontinuity that they find on lines and cables, creating additional propagating waves. By measuring the travelling time of each pulse-like signal and their respective reflections, it is possible to estimate the fault location from where they started propagating assuming their travelling speed is known [11–13]. Due to their high travelling speed, it is necessary to have high sampling frequency devices of at least 100 kHz [36], together with synchronized measurements to accurately identify each travelling pulse and to measure their travelling times. This approach has been successfully implemented in the transmission level, for long transmission lines and underground cables. For distribution systems however this approach remains impractical, since it is necessary to distinguish between all the travelling wave signals, which can be cumbersome in real system with several discontinuities [11–13] such as LV grids.

Finally, with the advent of machine learning techniques and its growing potential in several fields, some recent research has tried to apply it to the fault location problem. In a similar line of thoughts, new data-driven algorithms have also been developed to tackle the fault-location problem. These algorithms leverage on the wide-area deployment of smart meters in both MV and HV [37–39]. In this case, the main drawback is the necessity of having available training data for most machine learning algorithms. In most cases there might not be enough historical data for the training, and synthesizing reliable additional data is most times impractical. Furthermore, the training process needs to be re-tuned for each topological change in the grid [11–13].

While several years of research have been dedicated to establishing an accurate fault location methodology, this has not been applied in a universally accepted commercial solution. In actuality, the current practice that most DSOs use is to initially group customer outage calls to estimate the faulted section/area of the network [2]. Then, repair crews are deployed on-site to identify the fault location. For overhead lines, this can be done by visual inspection [2]. In the case of underground cables, several techniques have been developed depending on the fault type [40, 41]. In the case of underground short-circuits for example, the Thumper method is

Figure 1.3: Thrumper method for underground short-circuit location.

usually employed [40, 41], where a high voltage surge generator is used to apply a high voltage to the faulted cable, generating a high current-arc which creates a loud spark noise that can be detected on the surface by repair crews using microphone sensors as shown in Figure 1.3. This entire process can take from several minutes to multiples hours. As such, a centralized real-time fault location algorithm is still necessary for LV and MV networks.

So far, the fault location problem, both in transmission and distribution networks, has been tackled by considering the low or very high frequency behaviour of the system, leaving an unused window of intermediate frequency electromagnetic phenomena as shown in Figure 1.4. In just a few cases [42–44], the transient behaviour dominated by intermediate frequencies in the range of 5 to 500 kHz as defined in [45] have been used to tackle the problem. For example, in [43], they extend the impedance behaviour approach to frequencies up to 3 kHz to avoid the disturbances created by DGs. In [44], the authors use PMUs data to identify when the zero-sequence current lags the zero-sequence voltage during a fault event to identify the location. This idea is further developed by the authors in [42], however the proposed methodology requires a significant deployment of D-PMU across the grid to measure the currents flowing in each cable/line section. PMU devices are still expensive and not widely available in distribution networks, thus their access remains restricted mostly for transmission networks until the cost of μPMU becomes cost-effective for DSOs. These recent works show that there is an active effort in developing a fault location methodology based on the intermediate frequency transient behaviour of the grid during a fault event.

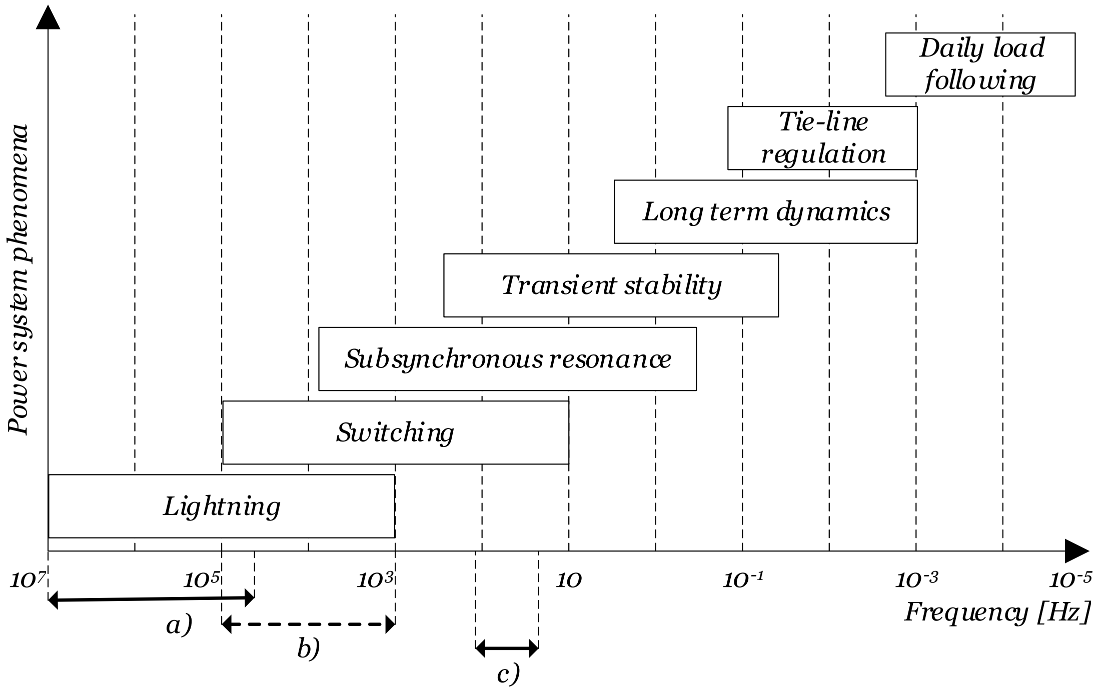

Figure 1.4: Frequency classification for fault location methodologies: a) Travelling wave approaches, b) Intermediate frequencies proposal, c) Impedance-based techniques.

This thesis aims to develop a new fault location methodology that makes use of the intermediate frequencies present in the transient response of the system immediately after the occurrence of a fault. To achieve this goal, three questions need to be addressed:

1. Is it possible to use intermediate frequencies to solve the fault location problem? If so, what is the mathematical and physical foundation of such approach?

2. What are the modelling considerations that need to be considered in order to use the intermediate frequencies transient response in a fault location methodology?

3. Is it possible to define a methodology that tackles the drawbacks of standard methods and that is applicable to real systems?

To answer the previous questions, this thesis will work on the basis of the following hypothesis.

1.2 Hypothesis

On one hand, impedance-based fault location methodologies are based on the variations caused by fault events in the fundamental frequency component of both voltage and current signals in the grid. On the other hand, traveling wave approaches consider the dependence that exists between the propagation delay of extremely high frequencies pulse-like signals and the location of the fault which originated them. There is therefore an unused window of intermediate frequencies of the signals generated by the fault events that hasn't been considered to establish a mathematical formulation for a fault location methodology. The thesis of this works relies on the hypothesis that:

The intermediate frequencies in the transient response characteristics of distribution networks after a fault event should depend on the fault location, just like the fundamental and higher frequencies do.

1.3 Objectives

1.3.1 Overall objective

The goal of this PhD work is to validate the previous hypothesis by designing a fault location methodology based on the intermediate frequency manifested during the distribution's network transient response after a fault event. This methodology must be applicable to underground distribution systems and must preserve a good level of accuracy given today's available measurement devices, noise level and considering different credible and possible fault scenarios.

1.3.2 Specific objectives

To design the fault location methodology it is necessary to:

- Formulate a dynamic model considering the differential equations governing the transient response of voltages in underground distribution networks during fault events.
- Define which transient response characteristics are dependent on the fault location and how other fault parameters, such as fault impedance, might affect them.
- Characterize the relationship between the fault location and the previously defined transient response characteristics.
- Determine the signal processing techniques necessary to extract the transient response characteristics from the measured signals.
- Design a comprehensive methodology to correctly identify, extract and process the transient response characteristics from voltage measurements to estimate the fault location under the presence of noise and considering today's measuring devices capabilities in distribution networks.
- Validate the proposed methodology by means of dynamic simulations in PSCAD and considering data from a real distribution network and fault events.

The rest of this Thesis is structured as follows. In the next sections of Chapter 1, a brief review of the different fault location methodologies available in the literature is presented. Chapter 2 provides the intuition and theoretical background behind the proposed fault location methodology. In Chapter 3, an LTI impedance modelling of cable/line sections is provided to be used in the fault location methodology. Chapter 4 describes the proposed fault location methodology based on the intermediate frequency transient behaviour of the grid, together with numerical results in a test system in PSCAD. Chapter 5 tackles the LTI modelling of black-box converters, to emulate their dynamics aiming to incorporate them in the proposed fault location methodology. Conclusions are presented in Chapter 6.

1.4 Publications

- N. Cifuentes and B. C. Pal, ”A New Approach to the Fault Location Problem: Using the Fault’s Transient Intermediate Frequency Response,” in *IEEE Open Access Journal of Power and Energy*, doi: 10.1109/OAJPE.2021.3089678.
- N. A. Cifuentes Otto, M. Sun, R. Gupta and B. C. Pal, ”Black-Box Impedance-Based Stability Assessment of Dynamic Interactions Between Converters and Grid,” in *IEEE Transactions on Power Systems*, doi: 10.1109/TPWRS.2021.3128812.

1.5 Current fault location solutions

In this section an overview of the different fault location methodologies available in the literature is presented, highlighting their main characteristics and limitations when implemented in distribution systems.

1.5.1 Impedance based fault location methodologies

The single-end impedance based methodologies for fault location use the fundamental frequency measurements of both voltage and current signals usually measured at the header substation of the distribution network [11–13]. If the feeder's impedance is known and we consider a single-line infinite-bus model of the distribution grid as the one shown in Figure 1.5 (adapted from [12]), then the fundamental frequency voltage and current measurements are dependent in the fault location and fault impedance according to equation (1.1) [11–13].

$$V_{f0} = i_{f0} \cdot d \cdot Z_{Line} + R_F \cdot i_F \tag{1.1}$$

Where Z_{Line} is the feeder's impedance, R_F is the fault resistance, d is the fault location as a percentage of the total feeder length, Z_{load} is the load of the network, i_F is the fault current, V_{f0} and i_{f0} are the fundamental frequency rms values of the voltage and current being measured at the feeder's header node. In the complex equation (1.1) there are three unknown variables:

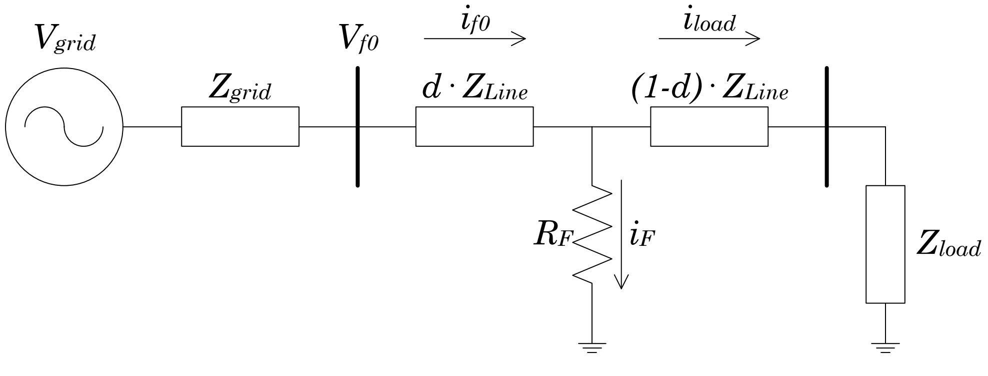

Figure 1.5: Single-line infinite-bus diagram.

i_F, R_F and d. It is thus necessary to firstly obtain the fault current i_F in order to solve equation (1.1), to estimate the fault location d and the fault impedance R_F. This has been addressed through assumptions such as considering that the fault resistance is small enough to be negligible [46], or by redefining the phasor equation (1.1) into it sequence form using the Fortescue transformation and then using fault current relationships depending on the fault type [47].

Although equation (1.1) provides a simple mathematical formulation to obtain the fault location, the single-line infinite-bus model of the distribution system used to derive it is not representative of real distribution grids. Real distribution networks are complex systems characterized by distribution feeders partitioned by many lateral branches with distributed loads, generally formed by short non-homogeneous lines being operated with unbalanced power flows and increasing levels of distributed generation [4, 12, 13]. The accuracy of impedance-based fault location methodologies can thus be affected by [46]:

- The combined effect of the load current and high fault impedances
- Inaccurate fault type identification
- Influence of zero-sequence mutual effects
- Presence of shunt and series compensation

Aside from the fault location inaccuracies originated from the fundamental assumptions on the distribution network modeling, one major drawback of single-end methods that consider measurements performed only in the distribution substation is the existence of multiple possible fault location solutions in a branched radial network as shown in Figure 1.6 (adapted from [2]) [2–4, 11–13]. What is being shown in Figure 1.6 is how in a branched network, it is possible that the impedance based formulation of equation (1.1) might have fault location candidate solutions in multiple branches. To overcome this drawback some works propose a multi-end impedance based methodology, which considers the deployment of additional measurement devices across the network [12], thus increasing the implementation costs of the methodology [3].

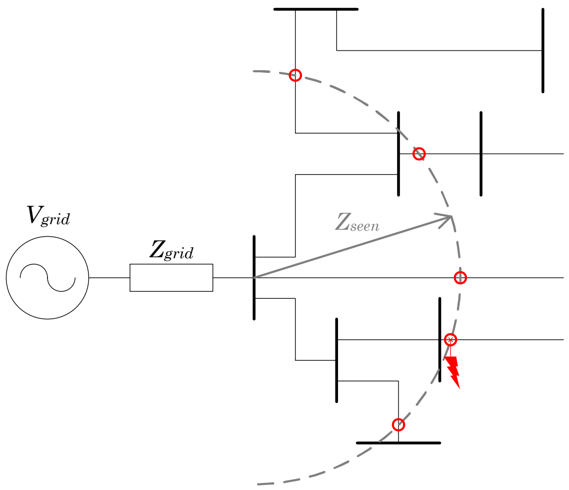

Figure 1.6: Multiple fault location problem.

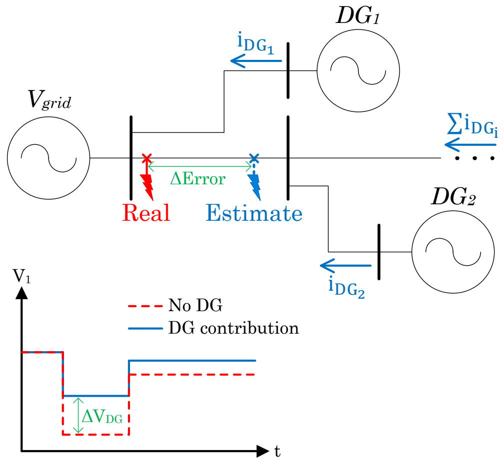

Figure 1.7: DG induced fault location inaccuracy.

Other options available in the literature consist in incorporating additional information such as voltage sag or current fluctuations to identify the real fault location from the set of candidates solutions [3, 4, 12].

In addition to the multiple fault estimation problem, the accuracy of single-end impedance-based fault location methodologies is affected by the presence of distributed generation in the network [3, 4, 12]. The fault location accuracy is affected by the current injected to the system by distributed generators, effectively modifying the impedance seen from the measuring point. This is illustrated in Figure 1.7, where it is possible to see how the voltage dip measured in the substation is smaller compared to a case without distributed generators, due to the current injected during the fault by DGs. This smaller voltage dip and current being measured at the substation is thus identified by fault location algorithms as a further away fault than the real one. These scenarios are possible if there are DGs in the grid with low voltage ride through capabilities that can provide voltage support during fault events, as well as in cases where the DGs are located further enough from the fault so they will remain connected and injecting power to the grid.

Despite the previous drawbacks, impedance based methodologies still attract researchers's attention for being the most promising methodology to be applied in fault location problems in actual power distribution systems. In [14], the authors propose a new fault location methodology for active distribution networks characterized by the presence of distributed generators. In their proposal, the authors consider the current contribution of inverter-based DGs during fault events by using an equivalent linear impedance model of the inverter's control scheme [14]. This in turn allows them to define an iterative impedance based methodology for fault location in active distribution grids. In [15] an impedance-based methodology is proposed to locate ground faults in the grid by considering distributed voltage measurement devices. More specifically, the authors use graph theory to define the measurement points in the network. The authors then proceed to use Kirchhoff's equations in the zero sequence representation of the grid to establish criteria to identify the closest node to the fault, from which they can deduce the faulted section of the network to finally apply an iterative procedure to estimate the fault location. In [16], the authors propose a fault location technique for resonant grounded networks. They use adaptive control to modify the impedance of an electromagnetic hybrid Petersen coil and then they proceed to measure the variation generated in the zero-sequence admittance along the faulty feeder to obtain the fault location.

1.5.2 Travelling wave approach

Immediately after the occurrence of a fault in the network, pulse-like signals are generated at the fault location and they start propagating through the system. The propagation velocity ν of these pulse signals is a constant defined by the electrical properties of the transmission line through which this collection of high frequency signals are travelling, known as travelling waves. More specifically, the propagation velocity is defined by the inductance and capacitance per unit of length of the transmission line [2–4, 11]. The travelling wave phenomenon is illustrated in Figure 1.8 (adapted from [11]), together with a lattice diagram which allows to understand the processes of reflection and refraction of the pulse signals.

At every discontinuity that the travelling wave encounters, a part of its energy is going to be reflected as a new travelling wave in the opposite direction while the remaining energy will continue travelling past the discontinuity as a refracted wave. These discontinuities in the network are defined as the boundaries where there is a change in the characteristic impedance

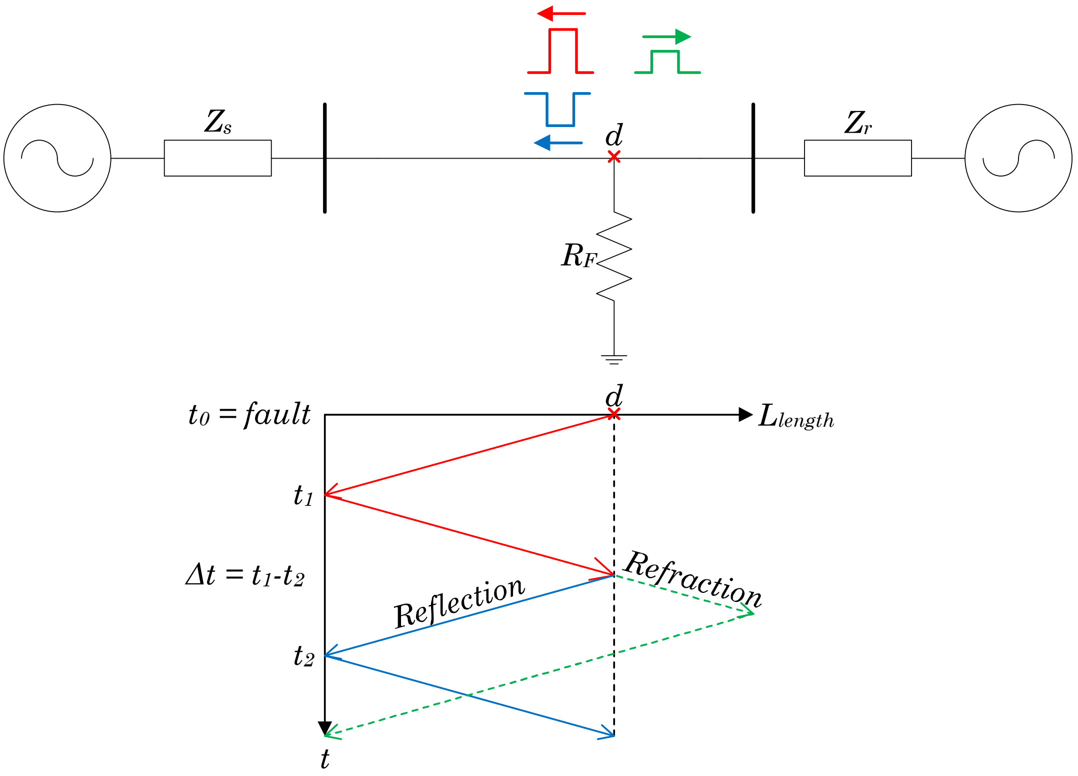

Figure 1.8: Travelling waves generated during a fault.

of the transmission medium. The resulting reflected wave can in some cases have an opposite polarity of the original travelling pulse, which can be detected by considering both voltage and current measurements [2–4, 11]. Single-end travelling wave methods rely on the concept of measuring the time delay Δt between the arrival-time t_1 of the original travelling pulse generated after the occurrence of the fault to the measuring device, and the time-arrival of its subsequent reflected wave in t_2. By knowing this time delay and the propagation velocity ν calculated using the electrical parameters of the transmission line it is thus possible to define the fault location using the expression:

$$d = \nu \cdot \Delta t \tag{1.2}$$

Although this fault location methodology has demonstrated to be effective at the transmission level, in distribution networks there are several obstacles for its implementation. The first problem relates to the high propagation velocity ν of electromagnetic waves in overhead lines and underground cables, which is usually in the range of 30 to 60% of that of the speed of light

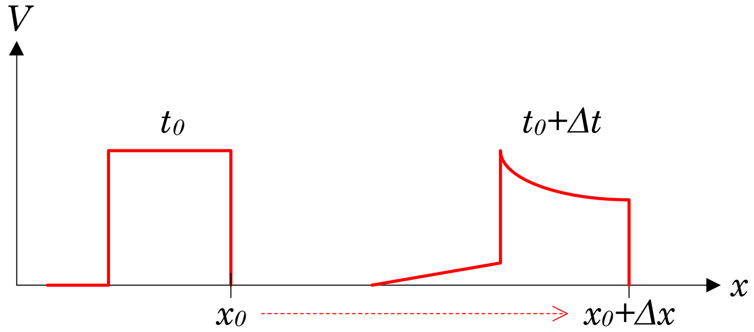

Figure 1.9: Distortion of a travelling wave.

$c \approx 3 \cdot 10^8$ $[m.s^{-1}]$ [23–25]. This in turns means that for distribution feeders which usually have a length ranging from a couple to tens of kilometers, the time delays being measured are in the order of the nanoseconds. To measure such short times it is necessary to deploy devices in the network with high sampling frequencies above 1 MHz, which are not currently available in distribution grids due largely to their high costs [2–4, 11].

Another major obstacle to travelling wave methods is the presence of laterals and sub-branches in distribution systems. Each lateral and sub-branch represents a discontinuity point in the network which will cause reflection and refraction of the travelling waves, making it increasingly difficult to correctly identify each pulse signal to measure its travel-time. To overcome this difficulty, some works have proposed to incorporate additional measurement devices in what is known as double-end methodologies. Other alternatives also consider the incorporation of frequency analysis of the positive sequence voltage signals generated after the fault, which is also refereed as aerial mode analysis [2–4, 11].

Finally, underground cables and overhead lines have a distorting behavior in the case of travelling waves. This means that the initial travelling pulse-like signal will suffer a change in its shape as it travels through the line [48]. An example of this phenomenon is shown in Figure 1.9 (adapted from [48]), where it is possible to see how a rectangular pulse-like signal will not remain square as it travels, being distorted by the line in such a way that the head of the wave losses energy transferring it to the tail of the wave [48]. This distorting process is related to the continuous reflection of a small amount of energy that occurs during the travelling of the electromagnetic wave. In addition, other phenomena such as the skin effect will also contribute to modify the shape of the signals. In the case of the skin effect, higher frequency current waves are distributed near the surface of the conductors, which translates in a smaller effective conducting section. This in turn means that higher frequency signals will experience a larger resistance and thus bigger losses. The front of the pulse-like travelling wave is a collection of high frequencies signals which will experience a larger resistance when travelling due to the skin effect, which further contributes to the distortion of the waveform by rounding the sharp corners of the wave front [48]. This distortion of the waveform is likely to make the identification process of the travelling signals more difficult.

The general approach used in research to tackle these issues is the use of wavelet-based analysis of the high frequency transients generated immediately after a fault occurrence [22–25,49]. The Wavelet transform maps a given function from the time domain into a time-scaling domain, which unlike the Fourier transform allows a localized analysis both in time and frequency. This property has promoted the Wavelet transform as an appropriate technique to detect the time occurrence of abrupt disturbances such as fault transients in the grid [49]. Initial research done in this field can be seen in [25], where the authors propose a travelling wave fault location method for three terminal lines. They apply the discrete wavelet transform (DWT) to the positive sequence voltages obtained by using the Clarke transform to the three-phase voltage measurements. From the coefficients obtained using the DWT, the authors can identify the travelling pulses by analyzing the time-evolution of the coefficient's maximum value. This in turn allows them to determine the faulted section in the network and then the fault location in the feeder using equation (1.2). In [24] the authors present a methodology for distribution networks that implements the continuous wavelet transform (CWT), with a mother wavelet generated from the initial transient signal generated after the fault. The works [22,23] continue in the tracks of the wavelet analysis, the first one using both the frequency and time domain information provided by the wavelet analysis, and the later combining both the DWT and CWT to improve the performance of the fault location technique. More recent works are focusing in new techniques, such as in [21] where the authors propose a fault location methodology using an adaptive extended Kalman filter to analyze the travelling wave signals instead of the wavelet transforms, while in [20] the authors propose to use a mathematical morphology technique to extract the information of high-frequency signals.

The travelling wave approach to solve the fault location problem in distribution systems is an active research field, but in the last years increasing attention is being redirected towards impedance-based methodologies and new machine learning algorithms described in the next section. This is due mainly to the highly complex behavior of travelling waves in short-branched lines as it is the case in distribution systems. This complex behaviour defines requirements for measurement devices such as: high sampling frequencies, high-speed communication channels with wide bandwidths and synchronized measurements. Such measurement devices are not currently available in distribution grids [2–4, 11].

1.5.3 Machine learning techniques

Machine learning techniques is a family of knowledge-based algorithms generally trained offline to recognize patterns in complex systems, which are generally not possible to analyze with more conventional mathematical techniques. Within this family, the most common machine learning algorithms used in fault location methodologies are artificial neural networks (ANN) and support vector machine (SVM) [2–4, 11].

In the case of artificial neural networks, they are designed according to known inputs and expected outputs, referred as a training set. In the case of the fault location problem, the known output is the fault location within a section, and the inputs can corresponds to the voltage and current waveforms measured at the distribution header. By using historical recorded data of fault location events and/or simulated ones, it is possible to design a ANN that solves the fault location problem for future fault location events. The design of the ANN is commonly referred as the training process in which the weights, activation functions, number of neurons and hidden layers are optimized based on the available training set to match the known inputs to their corresponding outputs. This can be done, for example, using the well-known Levenberg-Marquardt algorithm in feedforward neural networks. The general structure of the ANN as shown in Figure 1.10 (adapted from [3]) defined by the number of neurons, the number of hidden layers and the topology, is designed in such a way that the algorithm is capable to produce a

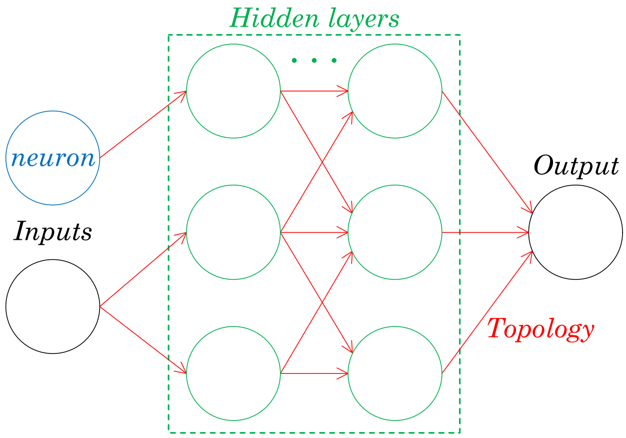

Figure 1.10: Artificial neural network structure.

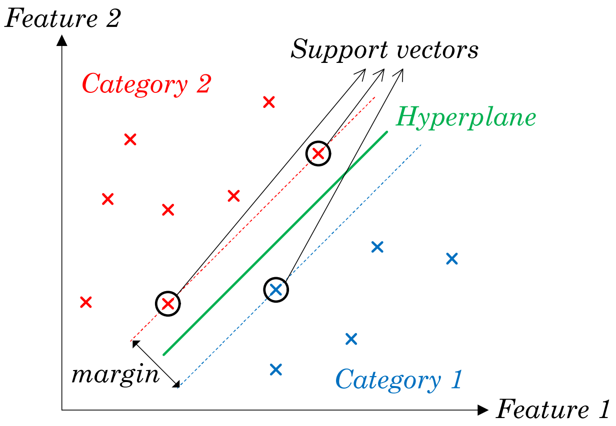

Figure 1.11: Support Vector Machine principle.

close estimation of the expected outputs in relation to the already known inputs obtained from simulations. In this case the expected output is the fault location in the network [2–4, 11].

Support vector machine is a supervised technique in which sparse data is already grouped and classified in different training sets according to a set of features. It is then possible to define a hyperplane that works as a boundary between the categories and maximizes the distance between the two sets, also known as margin. It is then possible to extract the features of interest from new measurements and use the known vectors and hyperplane to classify the new data into one of the already existing categories. This is illustrated in Figure 1.11 (adapted from [3]). For the fault location problem, SVM can be useful to identify types of fault; whether it is a balanced or unbalanced and if it is a fault to ground case or not. Using the same training set used for ANN, a SVM can be designed to classify different fault scenarios into their respective fault category. This can be achieve, for example, by pre-processing the input current and voltage waveforms and transforming them to the sequence domain. Once in the sequence domain, features such as the magnitude and phase angles of each symmetrical component can be used to design SVM to classify the event into its respective type which is known beforehand from the training set. SVM can thus be used on their own or in hybrid approaches together with ANN to solve the fault location problem [2–4, 11].

Machine learning algorithms can have similar or even better accuracy than impedance based methodologies and travelling wave approaches while maintaining short execution times. Unfortunately they also have some important drawbacks. The first major problem of machine learning techniques is the need of a training set to tune and design the algorithms. Ideally this can be achieved with a database containing historical data, which usually needs to be complemented with simulations to include other fault location scenarios. In the worst case there is no historical data available and thus the entire training set must be obtained through simulations [2–4, 11]. This in turn translates in a limiting factor when multiple features are needed for the algorithm, since more complex computational models and dynamic simulations are required. Given the high execution times and computational burden of such simulations, it is not possible to generate a large enough training set to ensure that the algorithms will perform correctly in all situations. In addition, for every topology change in the distribution network it might be necessary to repeat the training. Finally, some of the fault location algorithms are based on the mathematical principles of the impedance-based single-end methods, thus they can inherit some of their problems such as the multiple fault location estimate problem [2–4,11].

Some recent examples of research in fault location problems for distribution networks using ANN and SVM are reported in [26–29]. In [26] the authors use an artificial neural network to parameterize a polynomial function that models the fault voltage as a function of the fault current and location during a high impedance fault (HIF). They tested the proposed method in a single 13.8 kV feeder with seven lateral branches and they achieved a maximum fault location error estimation of 2.3%. In [27], the authors propose a fault location methodology for underground photovoltaic systems. In their work they use discrete wavelet decomposition to extract features from high frequency noise signals generated in the mid-point voltage of a DC-DC converter. The noise signal appears due to the switching of the PV inverters during the fault combined with the parasitic capacitance of PV panels and the underground cables. From different fault location simulations the authors infer that the high frequency spectrum of the noise signals is dependent on the fault location, so they propose to feed this high frequency features to a feedforward artificial neural network classifier to obtain the fault location. A similar approach is followed in [28], where the authors also use wavelet transform on the transient currents occurring after a fault to extract features to use as inputs for a feedforward neural network classifier, also refereed as extreme learning machine (ELM). They compare the performance of the proposed methodology using EML against traditional artificial neural networks and also support vector machine, showing that EML has statistically better generalization to estimate fault location in most cases. Finally, in [29] a fault location strategy is developed by considering a combination of different ANN. More specifically, the authors present a methodology for active distribution networks with distributed generation, and they propose the use of multiple neural networks. Each ANN estimates the fault distance from one of the generation unit, in addition to one ANN used to estimate the fault distance to the distribution substation. The final location is obtained by comparing the different estimates provided by the multiple ANNs.

From the literature review it is possible to conclude that the fault location problem in distribution networks is a subject of ongoing research. Current efforts to improve fault location strategies are continuing along three directions: impedance based methodologies, travelling wave approaches and machine learning techniques. In all three methods there are still unsolved problems that need to be addressed before achieving a scheme valid for today's distribution networks, together with their evolution towards more active and smart systems. In the next chapter, the mathematical and physical foundation for a new fault location methodology, based on the intermediate frequency contents of the system's transient response, is presented.

CHAPTER 2

Foundations for a New Solution

The objective of this chapter is to review the electromagnetic phenomena which define the transient response of a cable or transmission line. By carefully dissecting the transient response originated after the occurrence of a fault, key intuitions are derived in order to propose a new fault location methodology based on the intermediate frequency spectrum of the cable/line's transient response. These intuitions define the mathematical challenges that need to be addressed in order to establish the foundations of an applicable methodology to realistic distributing and transmission networks.

2.1 Transient response of a three-phase cable

In order to design a fault location methodology it is first necessary to understand the natural response of cables and transmission lines during a fault event. Immediately after the fault occurrence, an ensemble of signals covering a wide range of low to high frequencies will propagate while being damped over time according to the electrical characteristics of the transmission line. The period of time preceding the point that all non-fundamental frequency signals have been damped is termed the transient response regime. Once the transient response is over, the only signal remaining is the fundamental frequency of the system in what is defined as the steady state behavior of the line.

To help visualize the natural response of a cable/line section, a 10 km, 11 kV three-phase underground cable is modeled in PSCAD to represent a simple feeder configuration as shown in Figure 2.1. As will be explained in the next chapter, PSCAD allows to model the electromagnetic behaviour of underground cables up to the GHz range by means of the Universal Line Model (ULM). The ULM is considered to be the most accurate representation of cable and overhead line systems for EMT studies, and thus will be used as the benchmark model for all further theoretical and experimental discussions. The distribution substation is modeled as an infinite bus, i.e. as a voltage source behind an inductance that accounts for the high to medium voltage transformer from which the feeders starts. A three-phase fault is applied at the sending end of the feeder V_s and the phase voltages are measured at the receiving end of the cable V_r.

The natural response of the cable to the fault event is shown in Figure 2.2, where it is possible to appreciate both the transient and steady-state regimes with numbers 1) and 2) respectively.

Since the steady state behavior of the line is dominated by a single frequency, which corresponds to the fundamental frequency of the system as can be seen in zone 2) in Figure 2.2, the voltages and currents during this regime are defined by the impedance model of the components in the network. Within the transient response regime, three additional behaviours can be observed as shown in Figure 2.3, where a zoom has been performed to zone 1) of Figure 2.2. More specifically, as seen in Figure 2.3, the transient response to a fault event for a cable/line section is composed of:

1. The low frequency signals around the fundamental frequency and some of its harmonics. This range of frequencies are commonly used for impedance-based fault location methodologies.
2. An intermediate frequency response, which characterizes the natural oscillatory behaviour of the overall cable/line section.
3. The very high frequency signals, commonly used for the travelling wave phenomenon when considering pulse-like signals originated at the fault location and propagating in the system.

The results observed in Figures 2.1 and 2.3 were obtained using the frequency-dependent model for cables available in PSCAD, known in the literature as the Universal Line Model (ULM) which will be described in detail in the next Chapter. This model is able to accurately represent

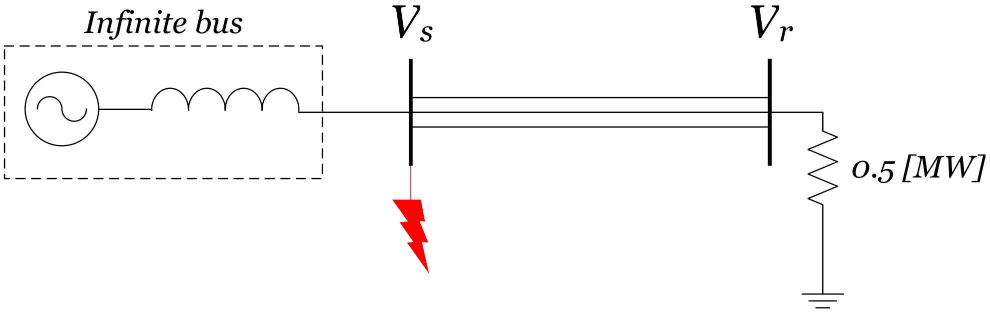

Figure 2.1: Underground cable fault simulated in PSCAD

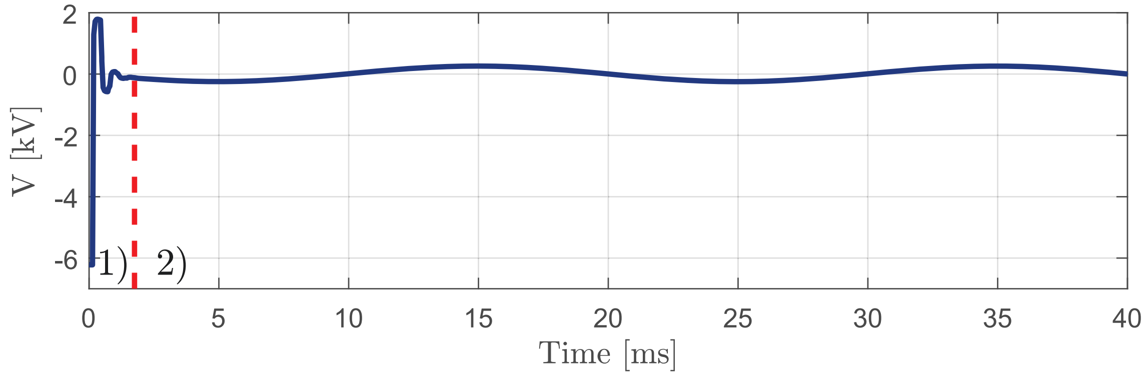

Figure 2.2: 11 kV underground cable's response for phase a after a fault which can be divided into: 1) The transient response regime 2) The steady state behavior.

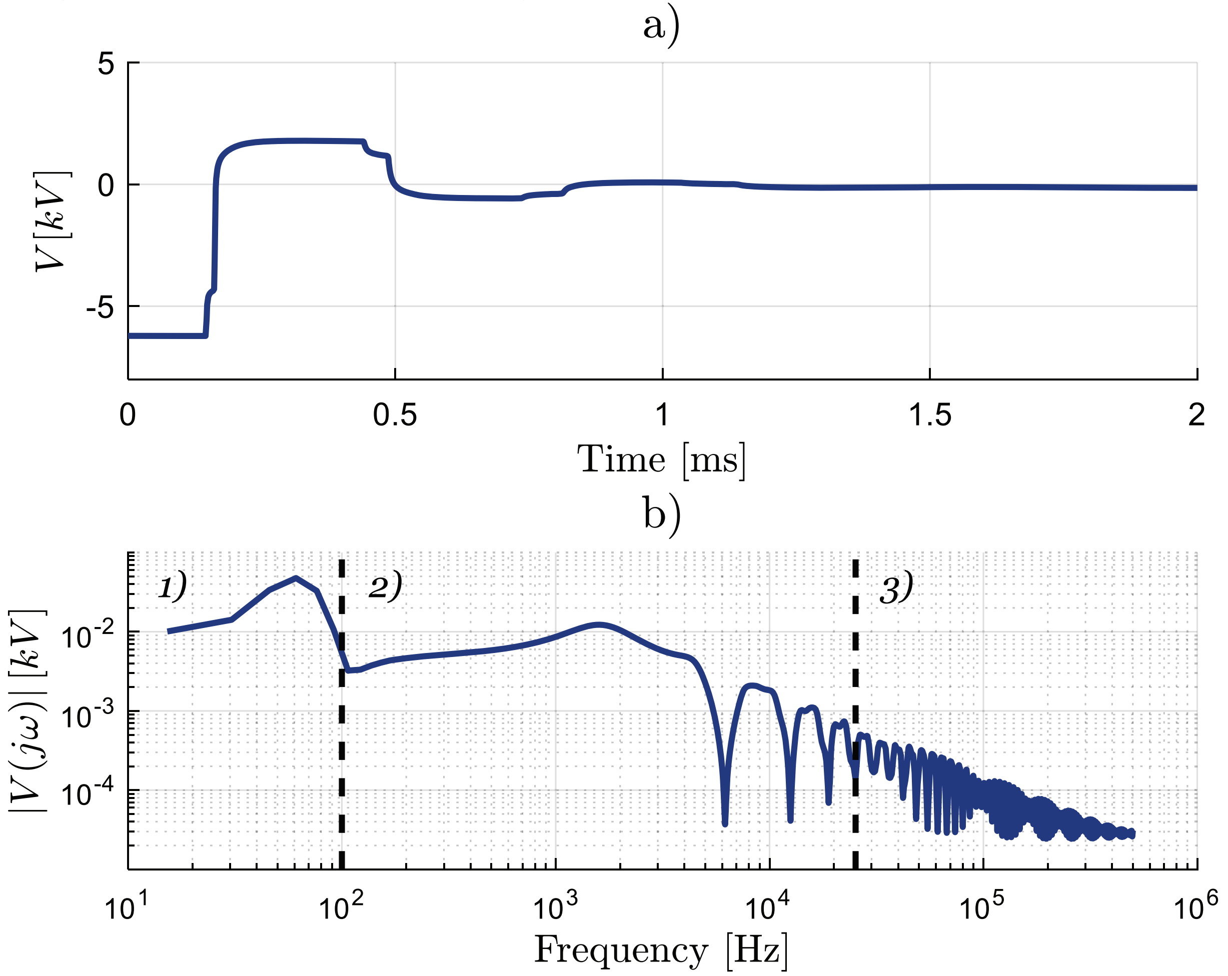

Figure 2.3: 11 kV underground cable's transient response for phase a: a) Full transient behaviour simulated in PSCAD, b) Frequency magnitude spectrum computed using the FFT.

the electromagnetic behaviour of cable/lines up to the GHz range, including the frequency-dependency of the cable/line's electrical parameters together with its distributed nature. Indeed, the electromagnetic behaviour of cable and transmission lines is frequency-dependent due to phenomena such as the skin and proximity effects. This in turn means that depending on the frequency range of interest, appropriate models for cable/lines need to be considered.

In the case of impedance-based fault location approaches for example, since a single frequency of 50 or 60 Hz is considered, and its associated wavelength is generally much larger than the length of the cable/line section (around 4000 to 8000 km), a Π - circuit lumped circuit model is sufficient. For travelling wave methods on the other hand, since extremely high frequencies are considered, the localized behaviour of electromagnetic waves is dominant. In these cases, the distributed nature of the electrical parameters is what defines the behaviour of the pulse-like signals travelling on the cable/line sections. For intermediate frequencies in the 5 to 500 kHz range, the frequency-dependent behaviour of the cable/line's electrical parameters should thus be expected to have a significant impact on its transient response. This is the first challenge that needs to be addressed to design a novel fault location methodology based on the intermediate frequencies present in the transient response. This modelling aspect will be discussed in detail in Chapter 3. In the next section, the relation between the fault location and the intermediate frequencies is explored with a non frequency dependent model to derived the mathematical foundations for a new fault location methodology.

2.2 Intermediate frequencies and fault location

The most basic modelling of a cable/line corresponds to its lumped Π-section representation. This model is valid for low frequencies, where the wavelength of the travelling EM waves is much longer than the length of the line. Although this modelling is not accurate enough for the transient fault location methodology proposed in this work, it provides insight on its theoretical foundation and challenges. During a fault event occurring at a percentage k of the line length D, it is possible to split the original Π-section with parameters R, L and C, into two new

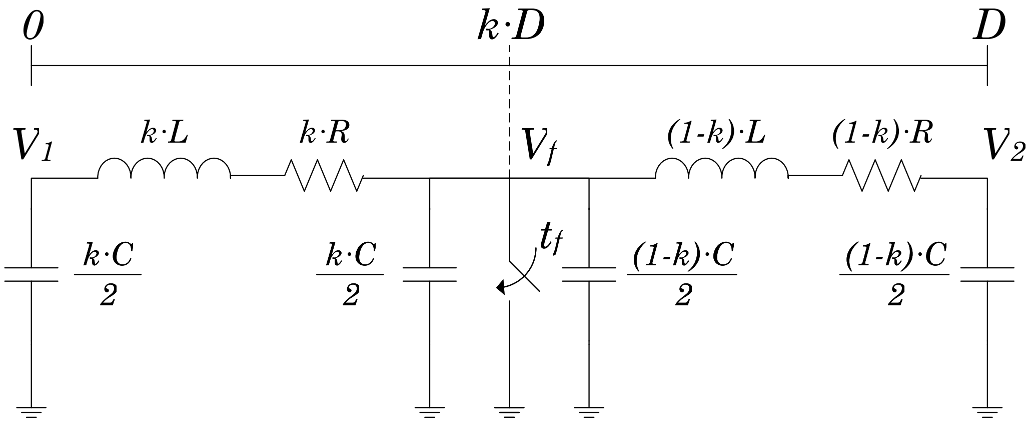

Figure 2.4: Π-section representation of a cable/line during fault event

sections with scaled electrical parameters as shown in Figure 2.4.

Considering an ideal fault to ground, i.e. $Z_f = 0\ \Omega$, each section will have a transient response defined by the differential equations (2.1)-(2.2). The solutions to these equations, defined by equations (2.3)-(2.4), show that the voltages' $V_1(t)$ and $V_2(t)$ transient response are oscillatory in nature. More importantly, the oscillations have the same damping $\tau = R/L$ but different frequencies ω_1 and ω_2, as defined in equations (2.5)-(2.6).

$$\ddot{V_1} + \frac{R}{L}\dot{V_1} + \frac{2}{k^2LC}V_1 = 0 \tag{2.1}$$

$$\ddot{V_2} + \frac{R}{L}\dot{V_2} + \frac{2}{(1-k)^2LC}V_2 = 0 \tag{2.2}$$

From equations (2.3)-(2.4) it is possible to see that the initial conditions $V_1(t_f)$, $V_2(t_f)$, $\phi_1(t_f)$ and $\phi_2(t_f)$ are defined by the fault's occurrence time t_f. The frequency of each transient response however, is dependent exclusively on the fault location and how it partitions the original cable/line section according to equations (2.5)-(2.6).

$$V_1(t) = V_1(t_f) \cdot e^{-\tau t} cos(\omega_1(k) \cdot t + \psi_1(t_f)) \tag{2.3}$$

$$V_2(t) = V_2(t_f) \cdot e^{-\tau t} cos(\omega_2(k) \cdot t + \psi_2(t_f)) \tag{2.4}$$

$$\omega_1(k) = \sqrt{\frac{2}{LC}} \cdot \frac{1}{k} = \sqrt{\frac{2}{LC}} \sum_{n=0}^{\infty} (-1)^n (k-1)^n \tag{2.5}$$

$$\omega_2(k) = \sqrt{\frac{2}{LC}} \cdot \frac{1}{1-k} = \sqrt{\frac{2}{LC}} \sum_{n=0}^{\infty} k^n \tag{2.6}$$

Although equations (2.5)-(2.6) are derived in a simplistic scenario, with a single cable section split by an ideal fault, four important observations can be made. Firstly, the intermediate frequencies associated with the transient response of the cable/line system during a fault event are dependent exclusively on the fault location. It is also important to note that, according to equations (2.5) and (2.6) the longer the cable/line section is, the lower the associated transient frequency will be. These frequencies are traditionally associated with switching and lightning electromagnetic phenomena in power system analysis as shown in Figure 1.4. To avoid confusion with travelling wave approaches and impedance-based methodologies, this frequency range will be referred in this work as intermediate frequencies, since they correspond to a middle ground between the high and low frequencies used in traditional techniques. The term switching frequency is also avoided since the proposed methodology does not rely on the switching of any specific equipment in the network, but rather on the natural response of the cable/line system to a fault event.

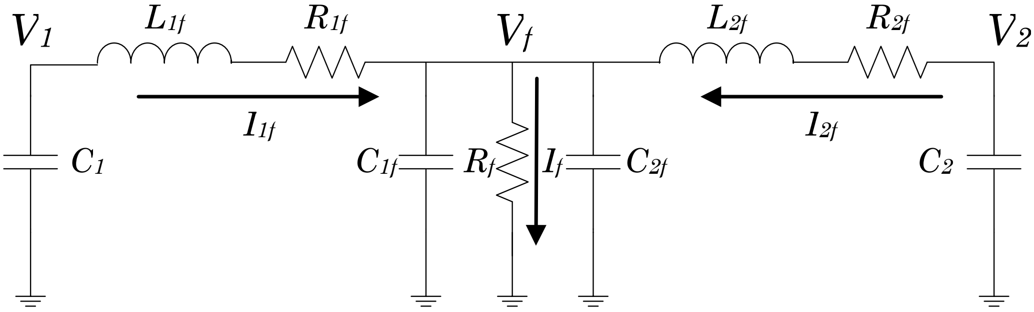

Figure 2.5: Coupled Π-sections during a fault event with fault impedance R_f

$$s \begin{bmatrix} I_{1f} \\ V_1 \\ I_{2f} \\ V_2 \end{bmatrix} = \begin{bmatrix} \frac{-R_{1f}}{L_{1f}} & \frac{1}{L_{1f}} & 0 & 0 \\ \frac{-1}{C_{1f}} & 0 & 0 & 0 \\ 0 & 0 & \frac{-R_{2f}}{L_{2f}} & \frac{1}{L_{2f}} \\ 0 & 0 & \frac{-1}{C_{2f}} & 0 \end{bmatrix} \begin{bmatrix} I_{1f} \\ V_1 \\ I_{2f} \\ V_2 \end{bmatrix} \tag{2.7}$$

$$s\begin{bmatrix} I_{1f} \\ V_1 \\ I_{2f} \\ V_2 \\ V_f \end{bmatrix} = \begin{bmatrix} \frac{-R_{1f}}{L_{1f}} & \frac{1}{L_{1f}} & 0 & 0 & \frac{-1}{L_{1f}} \\ \frac{-1}{C_{1f}} & 0 & 0 & 0 & 0 \\ 0 & 0 & \frac{-R_{2f}}{L_{2f}} & \frac{1}{L_{2f}} & \frac{-1}{L_{2f}} \\ 0 & 0 & \frac{-1}{C_{2f}} & 0 & 0 \\ \frac{1}{C_f} & 0 & \frac{1}{C_f} & 0 & \frac{-R_f}{C_f} \end{bmatrix} \begin{bmatrix} I_{1f} \\ V_1 \\ I_{2f} \\ V_2 \\ V_f \end{bmatrix} \tag{2.8}$$

Secondly, in a real system with loads and a non-ideal fault impedance, the different sections will behave as coupled-oscillators. This can be seen when considering Figure 2.5 and its dynamic equations (2.7) and (2.8) in the Laplace domain depending on the fault impedance conditions. When the fault is ideally grounded, i.e. $R_f = 0\ \Omega \Rightarrow V_f = 0V$, then equation (2.7) applies, which is equivalent to equations (2.1) and (2.1). From equation (2.7) it is clear that each oscillator can be solved independently, since there are no cross-coupling terms in the dynamic matrix of the system. When the fault impedance is non-ideal, i.e. $R_f \neq 0\ \Omega \Rightarrow V_f \neq 0V$, then equation (2.8) applies, where $C_f = C_{1f} + C_{2f}$. In this case, there are cross-coupling terms in the dynamic matrix of the system and so the oscillators are coupled. More specifically, the transient response in this case at each node will be a linear combination of the decoupled harmonic oscillators together with a DC component originated from the discharge of the capacitances to ground at the point of the fault. In addition, the frequency-dependence and distributed behaviour of each section's electrical parameters make it impossible to derive an analytical expressions for the fault location dependence of each frequency $\omega_i(k)$ as the ones in equations (2.5)-(2.6). However, a polynomial function $\hat{\omega}_i(k)$ with a sufficiently high order N_i, as defined in equation (2.9) where a_{in} is the real constant coefficient associated with the $n-1$ polynomial term of degree $n-1$, should be able to accurately represent the fault location dependence of each intermediate frequency $\omega_i(k)$. This is concluded from the series expansion of the intermediate frequencies functions shown in equations (2.5)-(2.6).

$$\omega_i(k) \approx \hat{\omega}_i(k) = \sum_{n=1}^{N_i} a_{in} \cdot k^{n-1} \tag{2.9}$$

While the previous analysis is intuitive in a deterministic approach, it is necessary for the

Table 2.1: Typical Impedances for Distribution Underground Cables

Size	L $[H/km]$	$C_{12.5kV}$ $[F/km]$	C_{25kV} $[F/km]$	$C_{34.5kV}$ $[F/km]$
2	8.95E-04	1.45E-07	1.30E-07	1.09E-07
1	8.62E-04	1.57E-07	1.40E-07	1.17E-07
1/0	8.40E-04	1.69E-07	1.51E-07	1.26E-07
2/0	8.16E-04	1.81E-07	1.61E-07	1.34E-07
3/0	7.93E-04	1.97E-07	1.74E-07	1.43E-07
4/0	7.69E-04	2.15E-07	1.90E-07	1.55E-07
250	7.50E-04	2.39E-07	2.10E-07	1.71E-07
350	7.16E-04	2.71E-07	2.38E-07	1.92E-07
500	6.80E-04	3.06E-07	2.68E-07	2.15E-07
750	6.37E-04	3.64E-07	3.18E-07	2.53E-07
1000	6.08E-04	4.17E-07	3.64E-07	2.87E-07

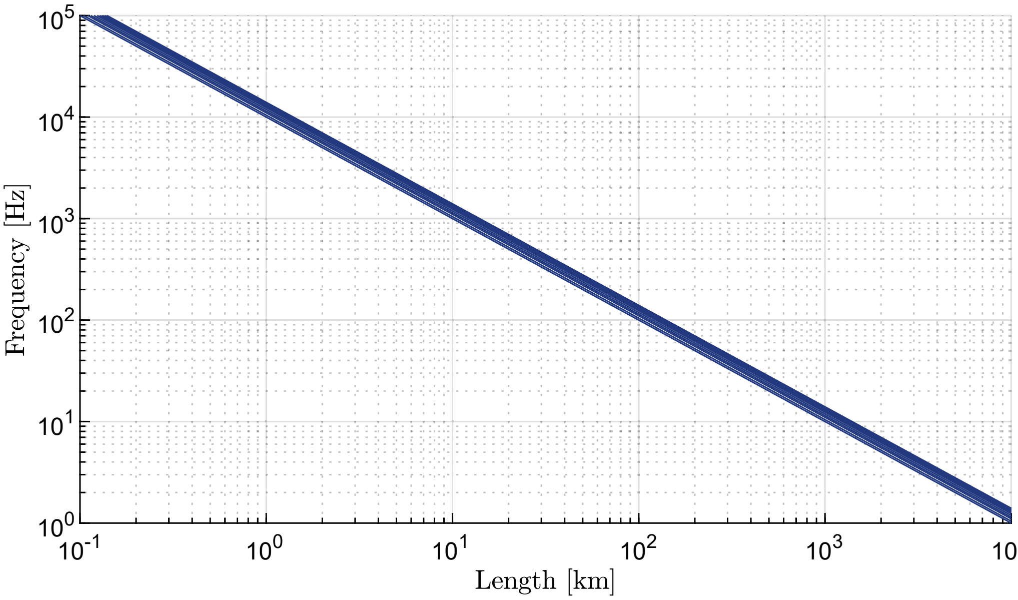

Figure 2.6: Typical frequencies of oscillation for 12.5 kV underground cables Π-Section models as a function of its length

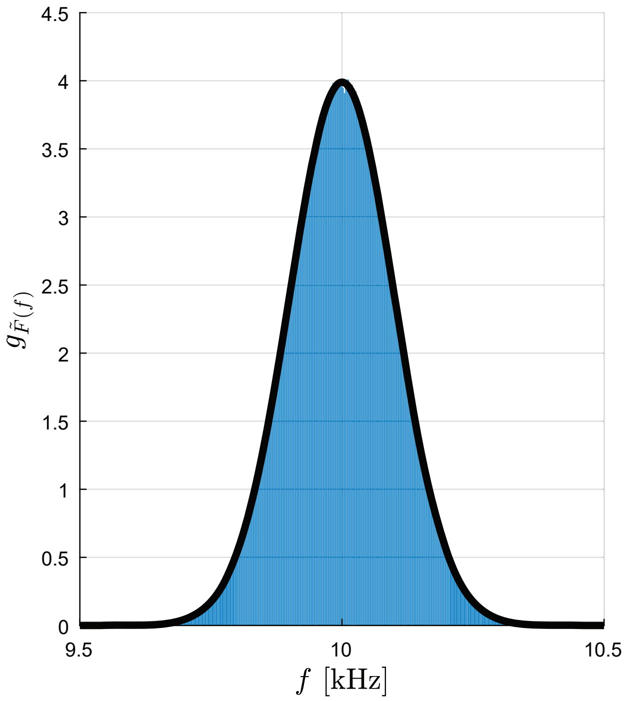

Figure 2.7: Example of random variable $\tilde{F}$. In light blue the histogram of 10^6 samples for $\tilde{F} \sim \mathcal{N}(10^4, 10^6)$.

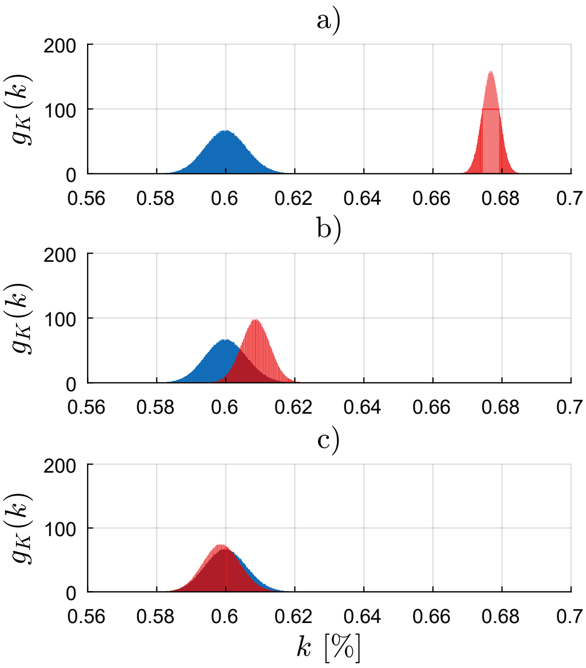

Figure 2.8: Probability density functions in light blue for $\tilde{K}$ and in light red for $\tilde{K}_{calc}$ for 10^6 samples when considering: a) $N_i = 4$, b) $N_i = 8$, c) $N_i = 12$.

polynomial approximation to handle frequency measurements as will be explained in the next sections. The intermediate frequency measurements used to solve the fault location problem will contain noise, which needs to be accounted for in the proposed methodology. Thus, it can be assumed that the frequency measurements are random variables which follow a normal distribution of the form $\tilde{W}_i \sim \mathcal{N}(\omega_i(k_r), \sigma_e^2)$ where $\omega_i(k_r)$ is the theoretical frequency corresponding to the real location k_r and σ_e is the measurement error associated with the presence of white noise. The typical L and C values for underground cables in distribution networks can be found in Table 2.1 [41]. The inductance will mainly depend on the core conductor cross-section size, while the capacitance depends mainly on the insulation layer thickness, which increases as a function of the rated voltage. From these values, the expected frequencies of oscillations $\omega_0(l)$ for different cable's lengths l are computed and shown in Figure 2.6. For distribution cable sections of typical length between 0.1 to 10 km, their associated transient frequencies will range from around 1 to 100 kHz respectively as can be seen in Figure 2.6. In the case of a simple oscillator as the one considered in Figure 2.4, the theoretical estimated location is defined by $\tilde{K} = \omega_0/\tilde{W}_1$. Thus, $\tilde{K}$ corresponds to a random variable that doesn't follow a normal distribution as $\tilde{W}_i$ does, but rather as a reciprocal normal distribution which corresponds to a binomial distribution [50]. On the other hand, the estimated location $\tilde{K}_{est}$ is obtained as one of the solutions to the polynomial equation (2.10) using the measured frequency $\tilde{W}_i$ as will be explained in more detail in the next sections.

$$\tilde{W}_i = \sum_{n=1}^{N_i} a_{in} \tilde{K}_{est}^{n-1} \tag{2.10}$$

It is thus important that the polynomial regression is performed considering a degree N_i high enough not only to obtain a good deterministic approximation of $\omega_i(k)$, but also so that $\tilde{K}_{est}$ has a probability distribution as close as possible to the reciprocal normal distribution of $\tilde{K}$, to minimize the estimation error of its expected value. An example of the impact that the polynomial regression degree N_i has on the probability density function (pdf) of $\tilde{K}_{est}$ is shown in Figure 2.8 when doing a Monte Carlo analysis. More specifically, Figure 2.7 and 2.8 are an example of 10^6 samples of the measured frequency $\tilde{W}$ considering a normal distribution of mean $\mu = 10$ kHz, which is a typical value for cable sections of length 1 km as can be seen in Figure 2.6, with a measurement error of $\sigma = 100$ Hz. The typical The mean value of 10 kHz corresponds to a fault location of $k = 60$ %, considering an intermediate frequency fault location function $\omega(k) = 2\pi \cdot 6000/k$. In Figure 2.8, the binomial distribution of $\tilde{K} = 2\pi \cdot 6000/\tilde{W}$ is calculated for each sampled point $\tilde{W}$ and shown in light blue. In light red, the distribution of $\tilde{K}_{est}$ is calculated using polynomial approximations of different degrees. From Figure 2.8, it is possible to see that low degree approximations are not enough to accurately represent the distribution of $\tilde{K}$. Instead, good approximations of the estimated fault location's binomial distribution can be obtained with a polynomial regression degree of 10 or more.

Thirdly, while travelling wave approaches are susceptible to the fault's inception angle, an intermediate frequency methodology would not. More specifically, if the inception angle of the fault is such that the voltage is close enough to zero ($V_f(t_f) \approx 0$), then the travelling wave signals will have a very small magnitude, comparable to the measurement noise. Intermediate frequencies on the other hand are triggered across the grid and at the time of the fault will not be zero, thanks to the phase angle shift $\psi_i(t_f)$ between voltage signals at different locations.

Finally, while the previous analysis was performed considering the behaviour of voltage transient signals, an analogous effect occurs for current signals, where their characteristic frequencies of oscillation will depend on the fault location. This means that both voltage and/or current signals can be used, as opposed to travelling wave approaches and impedance-based techniques were both currents and voltages signals are required. In what follows, the proposed methodology is presented considering voltage measurements, but the same procedures could be done considering current measurements. By considering both current and voltage measurements, it would be possible to increase the accuracy of the proposed methodology, as well as to provide the option to identify the fault type. This comes at an increased investment cost as more measurement devices are deployed in the network, and thus an optimization planning problem would need to be defined to choose the best measurement combination for a specific system, budget and technical requirements. This optimization problem is not tackled in this Thesis, since it is defined as future work that rises as a natural extension of the work being presented.

To validate the previous observations, preliminary results are presented in the next section for a test system developed in PSCAD.

2.3 Preliminary results

In the previous section, important observations were made based on the equations describing the transient response of a single Π-section model when split during a fault event. Since the previous conclusions will serve as a road-map to develop a new fault location methodology, it is necessary to validate them in a small test system. To achieve this, a simple 11 kV distribution test system is developed in PSCAD as shown in Figure 2.9. First, it is necessary to verify the existence of intermediate frequencies during the transient response of a small test system after a fault event, and whether or not their fault location dependence can be approximated by polynomial functions. Secondly, it is also important to compare the frequency response between the lumped Π-section and the frequency dependent models of underground cables during a fault event. This is necessary for verifying to which extend the intermediate frequencies derived considering the

Table 2.2: Cable Data

Parameters	**Value**
Configuration	Three cables flat
Cable separation	0.5 m
Cable depth	1 m
Rated line to line peak voltage	11 kV
Conductor outer radius	0.0047 m
Conductor material: copper	$\rho_{cu} = 172.4\ \mu\Omega\cdot\text{m}$
1st insulating layer thickness	0.0034 m
1st insulating layer material: XLPE	$\epsilon_1 = 2.5$
Sheath thickness	0.0019 m
Sheath material: copper	$\rho_{cu} = 172.4\ \mu\Omega\cdot\text{m}$
2nd insulating layer thickness	0.0018 m
2nd insulating layer material: PVC	$\epsilon_2 = 8$

Π-section model of cable/line sections remains valid for realistic network systems, and whether a more detailed model of cable/line sections should be considered in the analysis and fault location methodology.

The test case shown in Figure 2.9 is a network composed of different cable sections, all using the same 11 kV three-phase underground cable model defined by the parameters specified in table 2.2, but with different lengths as specified in table 2.3. Purely resistive loads are considered in this case, an each cable section is represented by its Π-section model with electrical parameters of $R = 0.8155\ \Omega/km$, $L = 3.339\ mH/km$ and $C = 0.0776\ \mu F/km$ at 50 Hz. The test system is connected to an infinite busbar through a transformer represented by its impedance $Z_{tfr} = R_{tfr} + jX_{tfr}$, providing the input voltage V_{in} to the system. A three-phase fault with impedance $Z_f = R_f + jX_f$ occurring in the cable section connecting busbars 1 and 2 is considered, which is modelled by scaling the electrical parameters of the resulting Π-sections by the fault location k as a percentage of the total cable length l_{12}. In total there are thus 5 cable sections being modelled during the fault event, each one with its own natural frequency of oscillation which can be derived analytically in a similar way as in equations (2.5) and (2.6). More specifically, since the network is composed of linear and passive elements, the oscillatory frequencies can be computed from the system's state-space model representation.

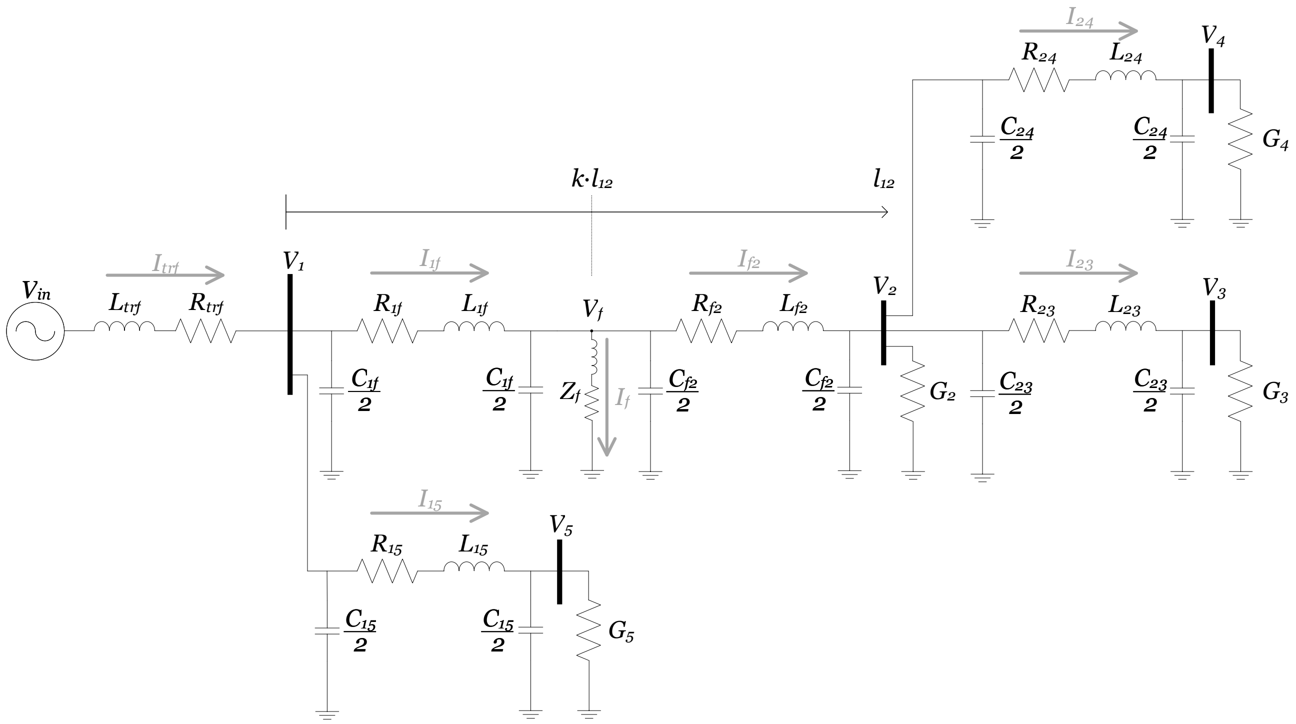

Figure 2.9: Preliminary test system using Π-section representation for underground cables.

Table 2.3: System Data

Parameters	**Value**
Transformer resistance	$R_{tf} = 1\ \Omega$
Transformer inductance	$L_{tf} = 0.1\ H$
Cable h1 length	10.0 km
Cable 12 length	6.0 km
Cable 13 length	15.0 km
Cable h4 length	13.0 km
Load P_1	0.5 MW
Load P_2	0.2 MW
Load P_3	0.3 MW
Load P_4	1.0 MW

$$\begin{aligned}
s\begin{bmatrix} I_{trf} \\ I_{1f} \\ I_{f} \\ I_{f2} \\ I_{15} \\ I_{23} \\ I_{24} \end{bmatrix}
&= \begin{bmatrix}
-\frac{R_{trf}}{L_{trf}} & 0 & 0 & 0 & 0 & 0 & 0 \\
0 & -\frac{R_{1f}}{L_{1f}} & 0 & 0 & 0 & 0 & 0 \\
0 & 0 & -\frac{R_{f}}{L_{f}} & 0 & 0 & 0 & 0 \\
0 & 0 & 0 & -\frac{R_{f2}}{L_{f2}} & 0 & 0 & 0 \\
0 & 0 & 0 & 0 & -\frac{R_{15}}{L_{15}} & 0 & 0 \\
0 & 0 & 0 & 0 & 0 & -\frac{R_{23}}{L_{23}} & 0 \\
0 & 0 & 0 & 0 & 0 & 0 & -\frac{R_{24}}{L_{24}}
\end{bmatrix}
\begin{bmatrix} I_{trf} \\ I_{1f} \\ I_{f} \\ I_{f2} \\ I_{15} \\ I_{23} \\ I_{24} \end{bmatrix} \\
&+ \begin{bmatrix}
-\frac{1}{L_{trf}} & 0 & 0 & 0 & 0 & 0 \\
\frac{1}{L_{1f}} & -\frac{1}{L_{1f}} & 0 & 0 & 0 & 0 \\
0 & \frac{1}{L_{f}} & 0 & 0 & 0 & 0 \\
0 & \frac{1}{L_{f2}} & -\frac{1}{L_{f2}} & 0 & 0 & 0 \\
\frac{1}{L_{15}} & 0 & 0 & -\frac{1}{L_{15}} & 0 & 0 \\
0 & 0 & \frac{1}{L_{23}} & 0 & -\frac{1}{L_{23}} & 0 \\
0 & 0 & \frac{1}{L_{24}} & 0 & 0 & -\frac{1}{L_{24}}
\end{bmatrix}
\begin{bmatrix} V_1 \\ V_f \\ V_2 \\ V_5 \\ V_3 \\ V_4 \end{bmatrix}
+ \begin{bmatrix} \frac{1}{L_{trf}} \\ 0 \\ 0 \\ 0 \\ 0 \\ 0 \\ 0 \end{bmatrix} V_{in} \\
&\Leftrightarrow s\mathbf{I} = \mathbf{A}_i\mathbf{I} + \mathbf{B}_i\mathbf{V} + \mathbf{B}_{in}V_{in}
\end{aligned} \tag{2.11}$$

$$s\begin{bmatrix} V_1 \\ V_f \\ V_2 \\ V_5 \\ V_3 \\ V_4 \end{bmatrix} = \begin{bmatrix} 0 & 0 & 0 & 0 & 0 & 0 \\ 0 & 0 & 0 & 0 & 0 & 0 \\ 0 & 0 & -\frac{2G_2}{C_{f2}+C_{23}+C_{24}} & 0 & 0 & 0 \\ 0 & 0 & 0 & -\frac{2G_5}{C_{15}} & 0 & 0 \\ 0 & 0 & 0 & 0 & -\frac{2G_3}{C_{23}} & 0 \\ 0 & 0 & 0 & 0 & 0 & -\frac{2G_4}{C_{24}} \end{bmatrix} \begin{bmatrix} V_1 \\ V_f \\ V_2 \\ V_5 \\ V_3 \\ V_4 \end{bmatrix}$$

$$+ \begin{bmatrix} \frac{2}{C_{1f}+C_{15}} & \frac{-2}{C_{1f}+C_{15}} & 0 & 0 & \frac{-2}{C_{1f}+C_{15}} & 0 & 0 \\ 0 & \frac{2}{C_{1f}+C_{f2}} & \frac{-2}{C_{1f}+C_{f2}} & \frac{-2}{C_{1f}+C_{f2}} & 0 & 0 & 0 \\ 0 & 0 & 0 & \frac{2}{C_{f2}+C_{23}+C_{24}} & 0 & \frac{-2}{C_{f2}+C_{23}+C_{24}} & \frac{-2}{C_{f2}+C_{23}+C_{24}} \\ 0 & 0 & 0 & 0 & \frac{2}{C_{15}} & 0 & 0 \\ 0 & 0 & 0 & 0 & 0 & \frac{2}{C_{23}} & 0 \\ 0 & 0 & 0 & 0 & 0 & 0 & \frac{2}{C_{24}} \end{bmatrix} \begin{bmatrix} I_{trf} \\ I_{1f} \\ I_f \\ I_{f2} \\ I_{15} \\ I_{23} \\ I_{24} \end{bmatrix} \tag{2.12}$$

$$\Leftrightarrow s\mathbf{V} = \mathbf{A}_v\mathbf{V} + \mathbf{B}_v\mathbf{I}$$

Based on the voltages and currents defined in Figure 2.9, a state-space formulation can be defined to characterize the transient response of the system during the fault event. For the currents flowing through each section, their state-space representation is defined by equations (2.11). For the voltages at each busbar of the system, their state-space representation is defined by equations (2.12). Combining both equations (2.11) and (2.12), it is possible to define a state-space representation for the entire network as defined by equation (2.13).

$$s\begin{bmatrix} \mathbf{V} \\ \mathbf{I} \end{bmatrix} = \begin{bmatrix} \mathbf{A}_v & \mathbf{B}_v \\ \mathbf{B}_i & \mathbf{A}_i \end{bmatrix} \begin{bmatrix} \mathbf{V} \\ \mathbf{I} \end{bmatrix} + \begin{bmatrix} \mathbf{0} \\ \mathbf{B}_{in} \end{bmatrix} V_{in} \tag{2.13}$$

$$\Leftrightarrow s\begin{bmatrix} \mathbf{V} \\ \mathbf{I} \end{bmatrix} = \mathbf{A}_{grid} \begin{bmatrix} \mathbf{V} \\ \mathbf{I} \end{bmatrix} + \begin{bmatrix} \mathbf{0} \\ \mathbf{B}_{in} \end{bmatrix} V_{in}$$

From the network's state-space representation shown in equation (2.13), it is possible to compute the intermediate frequencies defining its transient response for each fault location scenario k. Indeed, for each fault location value k in the section connecting busbars 1 and 2, the transient response's intermediate frequencies correspond to the imaginary part of the eigenvalues of the system dynamic matrix $\mathbf{A}_{sys}$, i.e. $\omega_i(k) = \Im(\lambda_i(k))$ where $\left\{\omega_1(k), \ldots, \omega_{N_f}(k)\right\}$ is the set of intermediate frequencies for the fault location k and $\left\{\lambda_1(k), \ldots, \lambda_{N_f}(k)\right\}$ is the set of complex eigenvalues of matrix $\mathbf{A}_{sys}$. This in turn allows to compute the set of expected intermediate frequencies for different fault locations $\{k_1, \ldots, k_N\}$ within a given section and then proceed to obtain their polynomial fittings. The results obtained for the case of a fault occurring in the section between busbars 1 and 2 with a fault impedance $R_f = 0.05\ \Omega$ are shown in Figure 2.10, together with their respective polynomial fittings of order 12. From Figure 2.10, it is possible to identify 5 intermediate frequencies of oscillation between 0.5 and 8 kHz, one for each Π-section in the network model as expected. It is also possible to see that polynomial functions of order 12 provide a good approximations of all 5 intermediate frequencies' dependence on the fault location k within the cable section connecting busbars 1 and 2.

The state-space modelling of the network also allows to compare the intermediate frequencies' behaviour for different fault conditions. More specifically, it is relevant to verify if the intermediate frequencies are exclusively dependent on the fault location as stated previously, or if other parameters such as the fault impedance have any impact on them. To validate this, the intermediate frequencies' dependence on the fault location is computed and compared for different fault impedance conditions R_f, as shown in Figures 2.11 and 2.12. From Figures 2.11 and 2.12, it is possible to see that indeed the intermediate frequencies are almost exclusively dependent on the fault location, with the fault impedance having an almost negligible impact on them over a wide range of R_f from 0.05 Ω to 40 Ω.

Finally, it is necessary to compare the frequency response of the system when considering Π-section and the detailed frequency dependent model of underground cables. This is achieved by simulating a three-phase fault at 90% of the cable connecting busbars 1 and 2, with a fault impedance of $R_f = 0.05\ \Omega$, considering both the lumped Π-section and frequency dependent model of cables. The three-phase instantaneous voltages are recorded, and then using the FFT

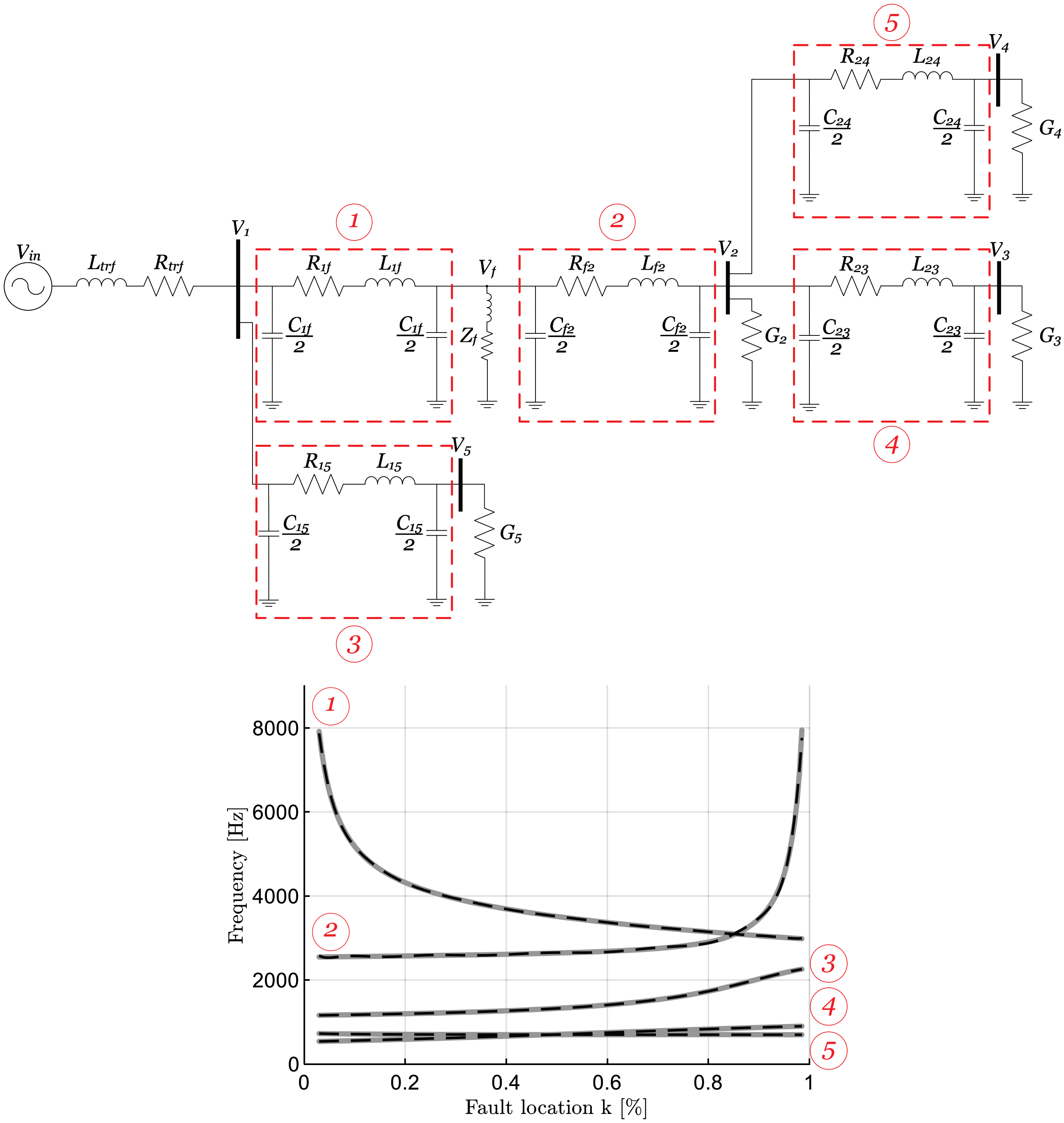

Figure 2.10: Intermediate frequencies as a function of the fault location k in the section between busbars 1 and 2. In solid grey line the theoretical values, in dotted black line their polynomial approximations of order 12. In red numbering, the match between the oscillatory frequencies and each Π-section is specified.

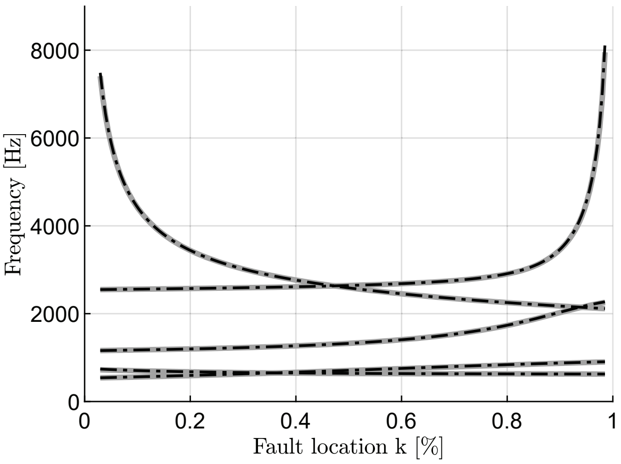

Figure 2.11: Theoretical intermediate frequencies: in solid grey line for $R_f = 0.05\ \Omega$ and in black dotted line for $R_f = 10\ \Omega$

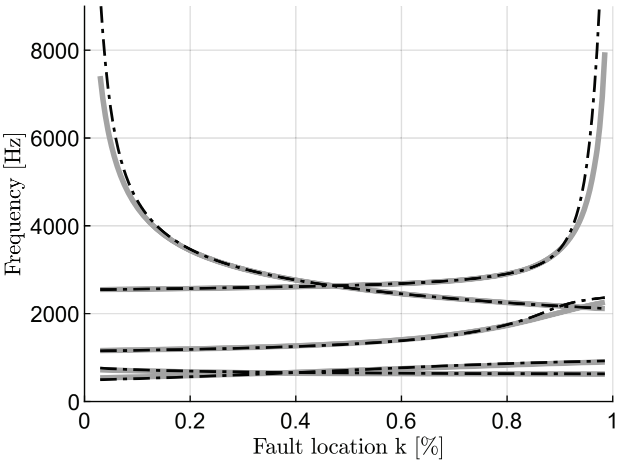

Figure 2.12: Theoretical intermediate frequencies: in solid grey line for $R_f = 0.05\ \Omega$ and in black dotted line for $R_f = 40\ \Omega$

the voltages' transient frequency response $V_i(j\omega)$ are computed. The magnitudes $|V_i(j\omega)|$ of each transient response are shown in Figure 2.13 when considering the two model approaches. As it is possible to see from Figure 2.13, there is a significant difference between the transient frequency responses predicted from the Π-section and frequency dependent models for underground cables. This demonstrates that computing the intermediate frequencies while considering the Π-section model for cable/line sections will lead to inaccurate fault location predictions. While it is standard practice to increase the order of the Π-section model by connecting several in series of smaller lengths, this allows to approximate the distributed nature of cable sections but not its frequency-dependent behaviour. It is thus necessary to consider and LTI model of cable/line section that is able to account for their electrical parameter's frequency dependent nature, so that an accurate fault location methodology can be developed for realistic power system networks.

From the previous conclusions, it is necessary to compute the polynomial approximations $\hat{\omega}_{ij}(k)$ describing the fault location dependence of the i^{th} intermediate frequency during a fault in the j^{th} cable section. With this information, a methodology to estimate the fault location based on the polynomial approximations and real-time measurements needs can be developed as presented in Chapter 4.

To accomplish the previous objective, in Chapter 3 an impedance modelling of cable/line sec-

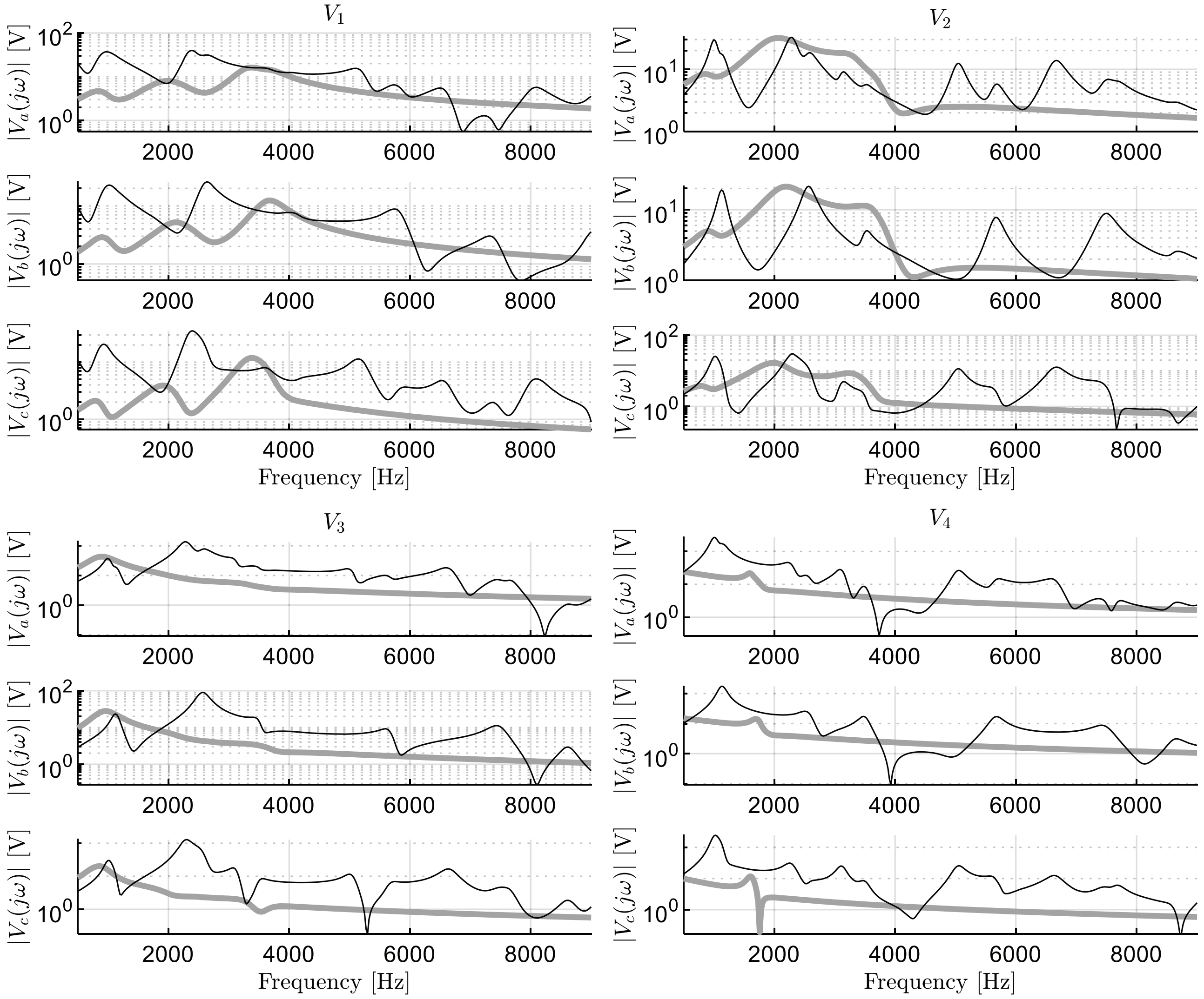

Figure 2.13: Voltages' transient frequency response comparison between the Π-section model of cables in solid grey line, and the detailed frequency dependent model in solid black line.

tions is proposed. The impedance model is based on the fundamentals of the ULM, in order to capture the frequency-dependence of the cable/lines' electrical parameter in a LTI representation. Using the proposed impedance model of cable/line sections, a fault location methodology based on the intermediate frequencies is described in Chapter 4.

CHAPTER 3

Impedance Modelling of Cables

Electromagnetic transient (EMT) studies have become a fundamental requirement in understanding power system's behaviour during switching events. Examples of such events in power systems are faults, lightning strikes, load variations and switching operation of devices such as power converters [51, 52]. Following such events, the energy exchange among different components in the grid can lead to overcurrents and overvoltages, which in turn can stress and damage the grid's components [51, 52]. Furthermore, these switching events can correspond to large disturbances such as three-phase faults, that can cause power systems' unstable operation if appropriate control schemes are not in place [53].

To perform EMT studies, various EMT simulators have been developed over the last 40 years, such as PSCAD and EMTP [54–59]. A core aspects of such simulators is to model the electromagnetic dynamics of overhead transmission lines and underground cable systems. More specifically, these models need to account for [52]:

- The well-known telegrapher's equations: differential equations which have known analytic solutions in the frequency and time domains.
- The frequency-dependence of the cable's longitudinal impedance's resistance $\mathbf{R}(s)$ and inductance $\mathbf{L}(s)$, due to the skin and proximity effects.
- The distributed nature of the cable's parameters.

To address the former aspects of the transmission line and cable EMT modelling, the Universal Line Model (ULM) was developed [54–59]. ULM is based on the fact that the cable's longitudinal impedance non-linear frequency behaviour is captured in its propagation matrix $\mathbf{H}(s)$ and characteristic admittance matrix $\mathbf{Y}_c(s)$. The traditional approach defined in [54–59] is to approximate both $\mathbf{Y}_c(s)$ and $\mathbf{H}(s)$ as a sum of rational functions in the frequency domain using vector fitting techniques [60–62]. The advantage of this methodology is that the rational functions have known inverse Laplace transforms in the time domain, i.e. exponential functions of time. This in turn allows to implement the convolution operator recursively, allowing to solve the telegrapher's equations in the time-domain while considering both the frequency dependence and the distributed nature of the longitudinal impedance [54–59].

In a separate and more recent branch of research, different approaches have tried to elaborate an impedance equivalent circuit of cables, derived from the rational functions obtained using the vector fitting techniques [63–66]. The impedance modelling of cables derived from the vector fitting is supported by the fundamental concept that the rational functions in the complex domain can be represented as equivalent electrical circuits [67]. These approaches can be traced back to the first articles related to transmission line and cable modeling [55], where a Foster representation of the approximated characteristic impedance is proposed. Although intuitive in their formulations, these approaches are either unable to capture the coupling of multiple phase systems, or they need large number of cascaded Π-sections for accurate results. An impedance representation of cables which includes the properties of the ULM would allow to:

- Represent complex networks by the cable's equivalent impedances. This representation would allow to obtain a linear state-space representation of such grids, which is a key aspect of the proposed fault location methodology presented in the next chapter.
- Extract relevant information regarding the network's dynamics such as the dominant oscillatory frequencies together with their damping coefficients for different operating conditions, topologies and disturbance scenarios. This can further improve, for example, the efficiency when performing dynamic security assessment studies with EMT/hybrid simulations or similar. In such types of studies, where large real networks are considered, the overall computation efficiency of EMT/hybrid simulations still needs to be improved [68].
- Identify key factors that define system's dynamics and stability before performing a full set of transient studies using EMT simulations.
- Work towards impedance-based modelling and analysis of complex power systems, an ongoing research field for converter-based technologies with a high number of non-linear differential equations [69–71], difficult to simulate in EMT programs on large quantities. The model must be accurate to at least capture the behaviour in the switching frequency range of power converters, i.e. dynamics in the kilohertz range [71].

In the following sections, firstly a review of the ULM's theoretical background is provided. Secondly, a summary of the incipient impedance modelling approaches for underground cables developed in recent years is described. These new modelling techniques are compared to the ULM formulation to highlight their limitations, which provides insight in why a new impedance model that captures the properties of the ULM is needed.

3.1 Universal line model formulation

Traditionally, to perform EMT simulations of underground cables, two categories of models are considered: lumped parameter models and distributed models. The first category is composed of the equivalent Π-model and the exact Π-model [57]. Further research has been done in recent years to improve the accuracy of the Π-section representation of cables [72]. Examples of such works consist of increasing the order of the model by connecting several cascaded Π-sections of smaller lengths or adding RL branches to capture some of the frequency-dependent behaviour, of cables [72]. The second category can in turn be separated in the Bergerson model -valid for a single frequency- and frequency dependent models [57]. Among these last ones, the most accurate one to date is the ULM, and it is the one typically used in EMT studies. The theory supporting the ULM corresponds to the telegrapher's equations for transmission lines and cables. More specifically, for an n-phase cable or transmission line system following the representation shown in Figure 3.1, the telegrapher's equations can be deduced from an infinitesimal representation of the electrical parameters of the system as shown in Figure 3.2 [54–59]:

By applying the Kirchhoff's laws to the system presented in Figure 3.2, it is possible to define

Figure 3.1: Sending and receiving end currents and voltages representation for transmission lines.

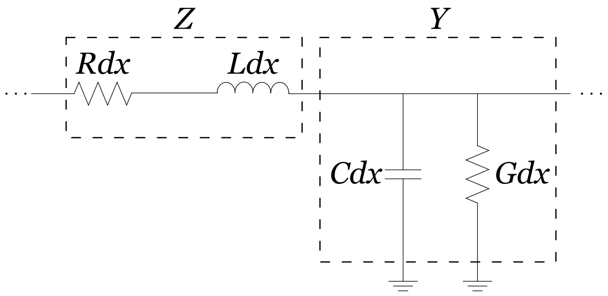

Figure 3.2: Infinitesimal representation of distributed parameters for transmission lines.

the telegrapher's equations and solutions in the Laplace domain as follows [54–59]:

$$\frac{d^2\mathbf{I}(s)}{dx^2} = [\mathbf{Y(s)Z(s)}]\,\mathbf{I(s)} \Rightarrow \mathbf{I}_x(s) = e^{-\mathbf{\Gamma}(s)x}\mathbf{I}_f(s) + e^{\mathbf{\Gamma}(s)x}\mathbf{I}_b(s) \tag{3.1}$$

$$\mathbf{V}_x(s) = -\mathbf{Y}(s)^{-1}\frac{d\mathbf{I}(s)}{dx} \Rightarrow \mathbf{V}_x(s) = \mathbf{Y}_c^{-1}(s)\left(e^{-\mathbf{\Gamma}(s)x}\mathbf{I}_f(s) + e^{\mathbf{\Gamma}(s)x}\mathbf{I}_b(s)\right) \tag{3.2}$$

$$\mathbf{Y}_c(s) = \sqrt{(\mathbf{Y(s)Z(s)})^{-1}}\mathbf{Y}(s)$$

$$\mathbf{\Gamma}(s) = \sqrt{\mathbf{Y(s)Z(s)}}$$

where $\mathbf{Z}(s)$ is the series per-unit-length longitudinal impedance matrix of the line, $\mathbf{Y}(s)$ is the per-unit-length shunt impedance matrix of the line, $\mathbf{Y}_c(s)$ is the characteristic admittance matrix of the system, $\mathbf{\Gamma}(s)$ is the propagation matrix of the system, $\mathbf{I}_f(s)$ and $\mathbf{I}_b(s)$ are the forward and backward travelling current vectors respectively. For clarity, bold letters are used to denote matrices. Regarding $\mathbf{Z}(s)$, it is a non-diagonal matrix containing cross-coupled terms in the off-diagonal positions. In the case of $\mathbf{Y}(s)$, it can be considered as a diagonal matrix since it is usually considered that the conductance $\mathbf{G}(s)$ is negligible, as well as the cross-coupled capacitance terms between phases. Both matrices $\mathbf{Z}(s)$ and $\mathbf{Y}(s)$ can be computed in different ways, one of the most common and accepted options is to use the well-known formulas from the Wedephol-Wilcox article [73], where the frequency-dependent elements of each matrix are calculated using formulas derived from the Maxwell equations.

Combining equations (3.1) - (3.2), applying the boundary conditions at $x = 0$ and $x = l$, and defining $\mathbf{H}(s) = e^{-\mathbf{\Gamma}(s)l}$ as the wave propagation matrix, the telegrapher's solutions in the

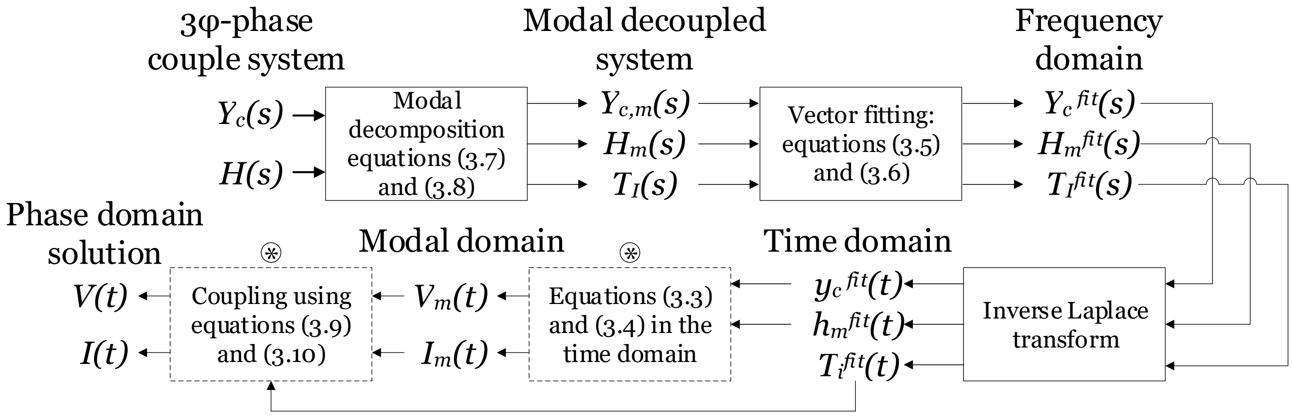

Figure 3.3: EMT simulation using ULM methodology scheme.

Laplace domain can be defined as follows:

$$\mathbf{I}_k(s) = \mathbf{Y}_c(s)\mathbf{V}_k(s) - \mathbf{H}(s)\left(\mathbf{Y}_c(s)\mathbf{V}_m(s) + \mathbf{I}_m(s)\right) \tag{3.3}$$

$$\mathbf{I}_m(s) = \mathbf{Y}_c(s)\mathbf{V}_m(s) - \mathbf{H}(s)\left(\mathbf{Y}_c(s)\mathbf{V}_k(s) + \mathbf{I}_k(s)\right) \tag{3.4}$$

where $\mathbf{V}(s)$ and $\mathbf{I}(s)$ are the phase voltage and current vectors. As it is possible to observe in equations (3.3) - (3.4), $\mathbf{Y}_c(s)$ is multiplying the voltage vectors while $\mathbf{H}(s)$ is multiplying both the voltage and current vectors. This in turn means that, in order to obtain the time-domain solutions for voltages and currents, it is necessary to apply the convolution operator in the time-domain equations after using the inverse Laplace transform in the equations (3.3) - (3.4) [54–59]. Due to the high computational cost of using the convolution operator, $\mathbf{H}(s)$ and $\mathbf{Y}_c(s)$ are approximated by sums of rational functions in the complex-domain using vector fitting techniques according to [57]:

$$Y_{c,ij}(s) \approx Y_{c,ij}^{fit}(s) = d_{ij} + \sum_{k=1}^{N} \frac{r_{k,ij}}{s - p_{k,ij}} \tag{3.5}$$

$$H_{ij}(s) \approx H_{ij}^{fit}(s) = \sum_{n}^{N_g} \left(\sum_{k=1}^{\tilde{N}} \frac{\tilde{r}_{nk,ij}}{s - \tilde{p}_{nk,ij}} \right) e^{-\tau_{n,ij} s} \tag{3.6}$$

where $\tau_{n,ij}$ corresponds to the travelling delay of each electromagnetic mode between the sending and receiving ends, N is the fitting order of $\mathbf{Y}_c(s)$, $\tilde{N}$ is the fitting order of $\mathbf{H}(s)$ and N_g is the number of delay groups. Also, $r_{k,ij}$ and $\tilde{r}_{nk,ij}$ correspond to the residues of the rational approximations for $\mathbf{Y}_c(s)$ and $\mathbf{H}(s)$ respectively, while $p_{k,ij}$ and $\tilde{p}_{nk,ij}$ correspond to their associated poles. The propagation modes can be obtained and grouped according to their travelling delays, after using modal decomposition to decouple the three-phase system. This is done by solving the eigenvalue problem [56, 59]:

$$\mathbf{Y}_c(s) = \mathbf{T}_I(s)\mathbf{Y}_{c,m}(s)\mathbf{T}_I^{-1}(s) \tag{3.7}$$

$$\mathbf{H}(s) = \mathbf{T}_I(s)\mathbf{H}_m(s)\mathbf{T}_I^{-1}(s) \tag{3.8}$$

where $\mathbf{T}_I(s)$ is the modal transformation matrix.

In the case of ideally transposed cables and transmission lines, $\mathbf{T}_I(s)$ is real and constant, corresponding to the Clarke transform. Otherwise, the matrix is complex and also frequency-dependent [59]. If cables are not transposed, then the frequency-dependent matrix $\mathbf{T}_I(s)$ must also be approximated using vector fitting techniques [59]. By solving equations (3.3) - (3.4) using the modal quantities $\mathbf{H}_m(s)$ and $\mathbf{Y}_{c,m}(s)$, it is then necessary to transform the modal voltage and current vectors to the phase domain as follows [59]:

$$\mathbf{I}(t) = \mathcal{L}^{-1}\left\{\mathbf{T}_I(s)\right\}(t) \circledast \mathbf{I}_m(t) \tag{3.9}$$

$$\mathbf{V}(t) = \mathcal{L}^{-1}\left\{\mathbf{T}_T^{-T}(s)\right\}(t) \circledast \mathbf{V}_m(t) \tag{3.10}$$

where $\circledast$ corresponds to the convolution operator.

The fundamental methodology for traditional EMT simulators using the ULM approach is summarized in Figure 3.3. As it is possible to see from the previous equations and the diagram in Figure 3.3, at least one convolution operation is necessary to perform EMT simulations in the time-domain when ideally transposed cables are considered. In addition, it is necessary to fit two matrix functions, both $\mathbf{H}(s)$ and $\mathbf{Y}_c(s)$ or $\mathbf{H}_m(s)$ and $\mathbf{Y}_{c,m}(s)$ depending on the approach.

To avoid using the convolution technique mentioned above, researchers have recently tried to establish an impedance equivalent modelling of cables and transmission lines [63–66]. These approaches are described in the next section.

3.2 Alternatives to the ULM

An impedance equivalent circuit representation of cables would allow to directly represent the frequency-dependence of their parameters in the time domain [64,66]. This in turn would allow to avoid using the convolution operator to solve equations (3.3) - (3.4) in the time-domain. In general, two approaches have been used to obtain these equivalent circuits:

- To represent the skin effect of the longitudinal impedance by means of parallel RL branches as shown in Figure 3.4 (adapted from [63]) [63, 65].
- Instead of approximating $\mathbf{H}(s)$ and $\mathbf{Y}_c(s)$ as done in EMT simulators, the total longitudinal impedance $\mathbf{Z}_T(s)$ and shunt admittance $\mathbf{Y}_T(s)$ defined in equations 3.11 and 3.12, are approximated using vector fitting techniques. The rational functions obtained from the fitting are represented as equivalent RLC circuits [64, 66].

$$\mathbf{Z}_T(s) = l \times \mathbf{Z}(s) \tag{3.11}$$

$$\mathbf{Y}_T(s) = l \times \mathbf{Y}(s) \tag{3.12}$$

where l corresponds to the total length of the cable.

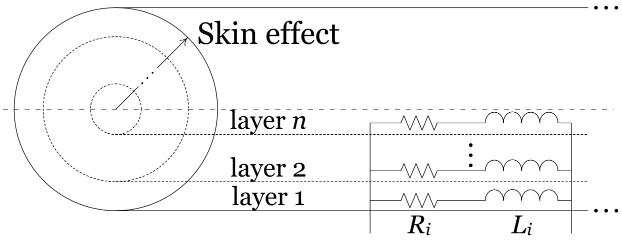

Figure 3.4: Skin effect impedance approximation.

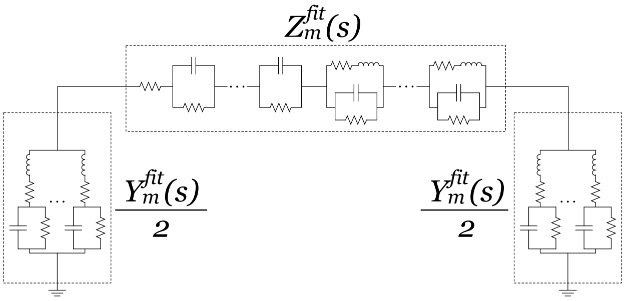

Figure 3.5: Π-circuit equivalent impedance model for cables.

Although the first approach is able to capture the frequency-dependence of the longitudinal impedance for a single cable, it does not account for the coupling between multiple cables in an n -phase system. Indeed, as it is already mentioned, $\mathbf{Z}(s)$ is a non diagonal matrix, with cross-coupled terms in the off-diagonal positions which are also frequency-dependent. As such, this approach is limited to DC or single-phase cables.

To deal with the coupling problem, references [64, 66] use a similar approach of the ULM methods and they consider the modal domain parameters instead of the phase-domain ones. In this case, the modal equations (3.9) and (3.10) are the same, and the total modal longitudinal impedance and shunt admittance are defined as follows [64, 66]:

$$\mathbf{Z}_{Tm}(s) = \mathbf{T}_I^t(s)\mathbf{Z}_T(s)\mathbf{T}_I(s) \tag{3.13}$$

$$\mathbf{Y}_{Tm}(s) = \mathbf{T}_I^{-1}(s)\mathbf{Y}_T(s)\mathbf{T}_I^{-t}(s) \tag{3.14}$$

Usually, the frequency-dependence of $\mathbf{Y}(s)$ is neglected in EMT simulators [65]. As such, $\mathbf{Y}(s)$ can be considered as a diagonal and constant matrix. When considering untransposed cables, $\mathbf{T}_I(s)$ becomes frequency-dependent, and so does $\mathbf{Y}_{Tm}(s)$ according to equations (3.13) and (3.14). To perform the impedance modelling of cables, references [64, 66] propose to use vector fitting techniques on the modal parameters $\mathbf{Z}_{Tm}(s)$ and $\mathbf{Y}_{Tm}(s)$ as they are defined in equations (3.13) and (3.14). The fitted parameters $\mathbf{Z}_{Tm}^{fit}(s)$ and $\mathbf{Y}_{Tm}^{fit}(s)$ are represented by equivalent RLC circuits using the relationships presented in [67]. This allows to establish an equivalent Π-section model as the one shown in Figure 3.5. Although intuitive, the previous approach does not consider the distributed nature of the cable's parameters. To overcome this limitation, the authors use multiple n-cascaded Π-sections connected in series [64, 66]. In this case, each Π-section is the result of approximating a smaller section of the cable with a length $l' = l/n$. While the approximation becomes more accurate as $n \to \infty$, the number of state variables increases too, and thus the proposed representation becomes computationally expensive and cumbersome to formulate and solve. This becomes particularly important when implementing this modelling technique in large systems of multiple underground cables.

As seen from the previous review, the impedance modelling of cables is still an active research topic. Further contributions must be made in order to obtain a model with similar accuracy as the ULM, that remains implementable in real systems for faster time-domain and transient analysis. In the next section, a new approach to the impedance modelling of cables is presented, which aims to fill the previous gaps in the literature.

3.3 Cable dynamics impedance modelling

The research reported in the literature is based on directly approximating the frequency-dependent behaviour of the longitudinal impedance $\mathbf{Z}(s)$ of cables. Although they follow an intuitive approach to the impedance modelling problem, they fall short when comparing their accuracy to that of the ULM in a practical way. To overcome the drawbacks of the previous techniques, a new impedance modelling techniques is proposed and described in this section. More specifically, the impedance $\mathbf{Z}_{tf}(s)$ and admittance $\mathbf{Y}_{tf}(s)$ transfer functions derived directly from the wave equations (3.3) and (3.4) are considered for the impedance modelling.

3.3.1 Cable's impedance and admittance transfer functions

The impedance and admittance transfer functions, which satisfy the wave equations (3.3) and (3.4), are well-know hyperbolic functions [74]. They are derived by considering the two-port network impedance matrix of a Π-section specified in equation (3.15) when considering the voltage and current convention in Figure 3.1 [74].

$$\begin{bmatrix} \mathbf{V}_k \\ \mathbf{I}_k \end{bmatrix} = \begin{bmatrix} \left(\mathbf{I} + \frac{\mathbf{Z}_{tf}\mathbf{Y}_{tf}}{2}\right) & -\mathbf{Z}_{tf} \\ \mathbf{Y}_{tf}\left(\mathbf{I} + \frac{\mathbf{Z}_{tf}\mathbf{Y}_{tf}}{4}\right) & -\left(\mathbf{I} + \frac{\mathbf{Z}_{tf}\mathbf{Y}_{tf}}{2}\right) \end{bmatrix} \begin{bmatrix} \mathbf{V}_m \\ \mathbf{I}_m \end{bmatrix} \tag{3.15}$$

where $\mathbf{I}$ corresponds to the $n \times n$ identity matrix. The wave equations (3.3) and (3.3) can in turn be rewritten in their matrix-form as:

$$\begin{bmatrix} \mathbf{Y}_c & -\mathbf{I} \\ \mathbf{H}\mathbf{Y}_c & \mathbf{H} \end{bmatrix} \begin{bmatrix} \mathbf{V}_k \\ \mathbf{I}_k \end{bmatrix} = \begin{bmatrix} \mathbf{H}\mathbf{Y}_c & \mathbf{H} \\ \mathbf{Y}_c & -\mathbf{I} \end{bmatrix} \begin{bmatrix} \mathbf{V}_m \\ \mathbf{I}_m \end{bmatrix} \tag{3.16}$$

By comparing equations (3.15) and (3.16) it is possible to define a Π -section that incorporates the dynamics described in the wave equations, defined by the impedance and admittance transfer functions as follows:

$$\mathbf{Z}_{tf}(s) = \frac{1}{2}\mathbf{Y}_c(s)^{-1}\left(\mathbf{H}(s)^{-1} - \mathbf{H}(\mathbf{s})\right) \tag{3.17}$$

$$\frac{\mathbf{Y}_{tf}(s)}{2} = \mathbf{Y}_c(s)\left(\mathbf{I} + \mathbf{H}(\mathbf{s})\right)^{-1}\left(\mathbf{I} - \mathbf{H}(\mathbf{s})\right) \tag{3.18}$$

If the shunt admittance matrix $\mathbf{Y}(\mathbf{s})$ of the cable system is considered diagonal, which is often the case in EMT simulations, then it is possible to compute the modal values of the transfer functions. More specifically, by using the identities (3.7) - (3.8) it is possible to define each i^{th} diagonal element of the modal impedance and admittance transfer functions as follows:

$$\begin{aligned} Z_{m,i}(s) &= \frac{Y_{cm,i}^{-1}(s)}{2} \times \frac{1 - H_{m,i}(s)^2}{H_{m,i}(s)} \\ \Leftrightarrow Z_{m,i}(s) &= Y_{cm,i}^{-1}(s) \times sinh\left(\Gamma_{m,i}(s)l\right) \end{aligned} \tag{3.19}$$

$$\begin{aligned} \frac{Y_{m,i}(s)}{2} &= Y_{cm,i}(s) \times \left(\frac{1 - H_{m,i}(s)}{1 + H_{m,i}(s)}\right) \\ \Leftrightarrow \frac{Y_{m,i}(s)}{2} &= Y_{cm,i}(s) \times tanh\left(\frac{1}{2}\Gamma_{m,i}(s)l\right) \end{aligned} \tag{3.20}$$

The advantage of equations (3.19) and (3.20) is that they are a function of the modal propagation $\mathbf{H}_m(s)$ and characteristic admittance $\mathbf{Y}_{cm}(s)$ matrices. This allows to define a rational function approximation for the modal impedance $\mathbf{Z}_m(s)$ and admittance $\mathbf{Y}_m(s)$ transfer functions respectively. These approximations are derived from the rational approximations of the wave propagation parameters performed in EMT simulations. It is possible to approximate each modal wave parameter by a sum of rational functions as follows:

$$Y_{mc,i}^{fit}(s) = d_i + \sum_{k=1}^{N} \frac{r_{k,i}}{s - p_{k,i}} = \frac{P_{y,i}(s)}{Q_{y,i}(s)} \tag{3.21}$$

$$\begin{aligned} H_{m,i}^{fit}(s) &= \left(\sum_{k=1}^{\tilde{N}_i} \frac{\tilde{r}_{k,i}}{s - \tilde{p}_{k,i}}\right) e^{-\tau_i s} \\ \Leftrightarrow H_{m,i}^{fit}(s) &\approx \frac{P_{h0,i}(s)}{Q_{h0,i}(s)} \times \frac{P_{d,i}(s)}{Q_{d,i}(s)} = \frac{P_{h,i}(s)}{Q_{h,i}(s)} \end{aligned} \tag{3.22}$$

where $P_{\cdot,i}(s)$ and $Q_{\cdot,i}(s)$ are used to denote polynomial functions of s with real coefficients for the wave parameters $\mathbf{H}_m(s)$ and $\mathbf{Y}_{cm}(s)$. In addition, the modal travelling delay $e^{-\tau_i s}$, obtained according to [75], can also be approximated by a sum of rational functions of order $N_{d,i}$ by using Padé approximant. In this case the rational approximation is denoted with the numerator and denominator polynomial functions $P_{d,i}(s)$ and $Q_{d,i}(s)$ respectively. By combining the previous rational approximations of the modal wave parameters in equations (3.19) and (3.20), it is possible to obtain rational approximations for the modal impedance and admittance transfer functions. It is important to note that this cannot be done directly on $\mathbf{Z}_{m,i}(s)$, since the modal propagation function in the denominator in equation (3.19) adds a negative delay, i.e. $\mathbf{Z}_{m,i}(s)$ is non-causal and thus cannot be approximated by rational functions. This is solved by considering its admittance inverse form $\mathbf{Z}^{-1}_{m,i}(s)$ instead to model the behaviour of the cable, since it is a causal function. By replacing the expressions (3.21) and (3.22) into (3.19) and (3.20), the rational function approximations for the admittance transfer functions can thus be defined as follows:

$$Z^{-1}_{m,i}(s) \approx \frac{P_{y,i}(s)}{Q_{y,i}(s)} \times \frac{P_{h,i}(s)Q_{h,i}(s)}{Q^2_{h,i}(s) - P^2_{h,i}(s)} \tag{3.23}$$

$$\frac{Y_{m,i}(s)}{2} \approx \frac{P_{y,i}(s)}{Q_{y,i}(s)} \times \frac{Q_{h,i}(s) - P_{h,i}(s)}{Q_{h,i}(s) + P_{h,i}(s)} \tag{3.24}$$

The polynomial fractions used for approximating the admittance transfer functions in equations (3.23) and (3.24) have an equivalent pole-residue form. Using these rational approximations, it is possible to define an equivalent circuit and a linear state-space model for each propagating mode. This in turn allows to independently compute the voltages and currents for each modal representation of a network. This is in principle similar to the methodology applied in the modal modelling used for cables in EMT simulations. In this case, the accuracy of the results is mainly limited by two factors:

- The approximation of the transformation matrix $\mathbf{T}_I(s)$ to compute the phase domain values.

- The approximation of the delay when using the Padé approximant.

Regarding the first factor, for the purpose of this thesis a perfectly transposed cable system will be considered. This means that the transformation matrix can be considered real and constant. The challenge associated with the frequency dependency of the transformation matrix will be tackled in future works, by extrapolating the proposed methodology to the improved phase domain ULM scheme presented in [76]. Regarding the influence in the approximation of the propagation delay, a high-enough order should suffice to provide accurate results up to high frequencies in the kilohertz range. The behaviour of higher frequencies cannot be accurately modelled by the proposed impedance model, unless an impractical and very high order approximation is considered for the delay. In the authors' opinion this should not have a significant impact on most transient analysis aside from travelling-wave phenomena, as will be shown in the next section. This is due to the much higher impedance values associated with very high frequencies, which translates in oscillations with high dampings and little contributions in the transient response. In the next section, the equivalent impedance model for a cable is presented, together with the state-space representation for transient analysis of a cable grid.

3.3.2 Cable's impedance and grid's state-space model

In order to establish the cable's state-space model, it is necessary to firstly define an equivalent impedance model circuit. This can be done by approximating the modal admittance transfer functions $Z_{m,i}^{-1}(s)$ and $Y_{m,i}(s)/2$. More specifically, the approximated values defined in (3.23) and (3.24) can be written in their pole-residue form as:

$$\begin{aligned} Y_{m,i}(s) = D_i + \sum_{k=1}^{M_i} \frac{r_{k,i}}{s - p_{k,i}} \\ + \sum_{k=M_i+1}^{M_i+N_i} \left(\frac{r_{k,i}}{s - p_{k,i}} + \frac{\bar{r}_{k,i}}{s - \bar{p}_{k,i}} \right) \end{aligned} \tag{3.25}$$

where

$$\{D_i\}_i, \in \mathbb{R}, \ \forall i \in \{1, ..., n\}$$

$$\{r_{k,i}\}_{k=1}^{M_i}, \ \{p_{k,i}\}_{k=1}^{M_i} \in \mathbb{R}, \ \forall i \in \{1, ..., n\}$$

$$\{r_{k,i}\}_{k=M_i+1}^{N_i+M_i}, \ \{p_{k,i}\}_{k=M_i+1}^{N_i+M_i} \in \mathbb{C}, \ \forall i \in \{1, ..., n\}$$

Each admittance approximation can be represented via a Foster RLC circuit. This is shown in Figure 3.6 for the case of the series admittance transfer function $Z_{m,i}^{-1}(s)$ connecting two busbars, by following the equivalences presented in [67]. An equivalent representation exists for the shunt admittance transfer function $Y_{m,i}(s)/2$, where V_m must be replaced by a ground connection. The circuit parameters can be computed from the pole/residue values based on the relationships in [67], which are summarized for the admittance case in equations (3.26), (3.27) and (3.28). Analogous equations for the impedance Foster circuit realization case can be found in [67]. The Foster equivalent circuit shown in Figure 3.6, together with equations (3.26) - (3.28), define the impedance model for cables/line sections, incorporating both the frequency-dependence and distributed nature of its parameters.

$$R_0 = \frac{1}{D} \tag{3.26}$$

$i \in \{1, ..., M\}$:

$$\begin{cases} L_i = \frac{1}{r_i} \\ R_i = \frac{-p_i}{r_i} \end{cases} \tag{3.27}$$

$i \in \{M+1, ..., N\}$:

$$\begin{cases} L_i = \frac{1}{r_i + \bar{r}_i} \\ R_i = -\frac{r_i p_i + \bar{r}_i \bar{p}_i}{(r + \bar{r}_i)^2} \\ C_i = \frac{(r_i + \bar{r}_i)^4}{p_i \bar{p}_i (r_i + \bar{r}_i) - (r_i p_i + \bar{r}_i \bar{p}_i)(r \bar{p}_i + \bar{r}_i p_i)} \\ R'_i = \frac{-1}{C_i} \frac{r_i + \bar{r}_i}{r_i \bar{p}_i + \bar{r}_i p_i} \end{cases} \tag{3.28}$$

Additionally, from the Foster circuit realizations it is possible to define a state-space model to represent power networks. In the case of the admittance Foster circuit representation shown in Figure 3.6 b), by applying Kirchhoff's laws it is possible to write the state-space model as shown in equation (3.29). An analogous state-space representation can be written for the impedance Foster representation case.

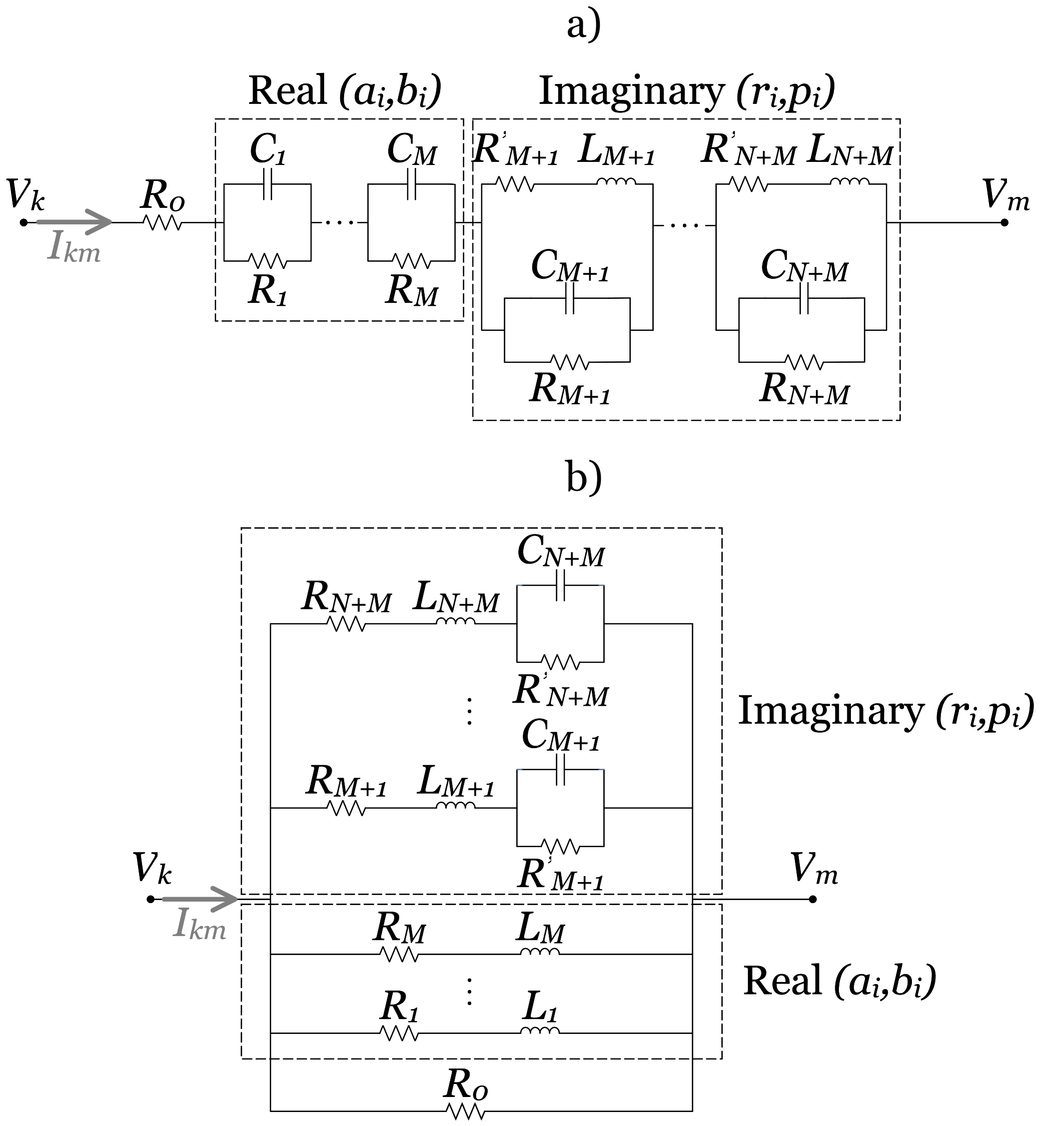

Figure 3.6: Foster circuit realization from the pole/residue form for: a) impedance case, b) admittance case

$$\begin{cases} s\mathbf{X} = \mathbf{A}\mathbf{X} + \mathbf{B}u \\ y = \mathbf{C}\mathbf{X} + Du \end{cases} \tag{3.29}$$

where $\mathbf{X} = [I_1 \cdots I_M \; I_{M+1} \cdots I_{M+N} \; V_{c,M+1} \cdots V_{c,M+N}]^t$, $u = I_b$, $y = V_b$ and:

$$\mathbf{A} = \left[\begin{array}{ccc:ccc:ccc}
-\frac{R_0+R_1}{L_1} & -\frac{R_0}{L_1} & \cdots & -\frac{R_0}{L_1} & \cdots & -\frac{R_0}{L_1} & & & \\
-\frac{R_0}{L_2} & \ddots & & \vdots & & \vdots & & & \\
\vdots & & -\frac{R_0+R_M}{L_M} & -\frac{R_0}{L_M} & \cdots & -\frac{R_0}{L_M} & & & \\
\hdashline
-\frac{R_0}{L_{M+1}} & \cdots & -\frac{R_0}{L_{M+1}} & -\frac{R_0+R_{M+1}}{L_{M+1}} & -\frac{R_0}{L_{M+1}} & \cdots & -\frac{1}{L_{M+1}} & & \\
\vdots & & \vdots & -\frac{R_0}{L_{M+2}} & \ddots & & & \ddots & \\
-\frac{R_0}{L_{M+N}} & \cdots & -\frac{R_0}{L_{M+N}} & \vdots & & -\frac{R_0+R_{M+N}}{L_{M+N}} & & & -\frac{1}{L_{M+N}} \\
\hdashline
 & & & \frac{1}{C_{M+1}} & & & -\frac{G'_{M+1}}{C_{M+1}} & & \\
 & & & & \ddots & & & \ddots & \\
 & & & & & \frac{1}{C_{M+N}} & & & -\frac{G'_{M+N}}{C_{M+N}}
\end{array}\right]$$

$$\mathbf{B} = \begin{bmatrix} \frac{R_0}{L_1} & \cdots & \frac{R_0}{L_M} & \frac{R_0}{L_{M+1}} & \cdots & \frac{R_0}{L_{M+N}} & 0 & \cdots & 0 \end{bmatrix}^t$$

$$\mathbf{C} = \begin{bmatrix} -R_0 & \cdots & -R_0 & -R_0 & \cdots & -R_0 & 0 & \cdots & 0 \end{bmatrix}$$

$$D = R_0$$

The previous representation is just one among many other possible state-space configurations, however it provides advantages for power systems modelling. Indeed, the advantages of these state-space representations are:

- Since they are derived for each modal component of the admittance transfer functions $Z_m^{-1}(s)$ and $Y_m(s)/2$, they can be used independently to describe the behaviour of each modal component of the voltages and currents.
- Grouping parallel cables into equivalent $Z_{m,eq}^{-1}(s)$ and $Y_{m,eq}(s)/2$ state-space representations is straightforward.

- It is easy to incorporate other elements such as loads and faults in the system.

- It is possible to easily defined the state-space representation for a whole cable network.

Once state-space models have been computed for all cable/line sections, they can be further aggregated to compute the state-space form of the entire grid. This can be done by first establishing one state-space representation for all branch element connections between busbars, and another state-space model for all shunt element connections from each busbar to ground.

For shunt connections to ground, the input signal is the current $I_k = \sum_i I_{ik} - \sum_j I_{kj}$ flowing from the k^{th} busbar to ground, while the output signal correspond to the respective busbar voltage V_k. This state-space model accounts, for example, for the loads S_k in the system, for the cables/lines' shunt transfer functions $Y_{m,i}(s)/2$ and for fault events with a fault impedance R_f. As mentioned before, using the Foster representations shown in Figure 3.6 it is straightforward to aggregate all of the previous models into a single one for each busbar as shown in Figure 3.7. The aggregated state-space representation for all busbars in the grid is presented in equation (3.30), where $\mathbf{I}_b = [I_1 \cdots I_{N_b}]^t$, $\mathbf{V}_b = [V_1 \cdots V_{N_b}]^t$, $\mathbf{X}_b = [\mathbf{X}_1 \cdots \mathbf{X}_{N_b}]^t$, $\mathbf{A}_b = diag\,(\mathbf{A}_1, \ldots, \mathbf{A}_{N_b})$, $\mathbf{B}_b = diag\,(B_1, \ldots, B_{N_b})$, $\mathbf{C}_b = diag\,(\mathbf{C}_1, \ldots, \mathbf{C}_{N_b})$, $\mathbf{D}_b = diag\,(D_1, \ldots, D_{N_b})$ and N_b is the number of busbars in the system.

For series elements connecting busbars/voltage sources, such as the series branches of cable/line sections $Z_{m,i}^{-1}$ and transformers, they can be represented in a separate state-space model. In this case, the input signals are the voltage drops $\Delta V_{km} = V_k - V_m$ between the connected busbars, including the input voltages to the grid V_{in} set by voltage sources such as synchronous machines or VSC converters. The output signals correspond to the flowing currents I_{km} on each series branch of the system. The aggregated state-space representation for all series connection elements in the grid is presented in equation (3.31), where $\mathbf{\Delta V}_{km} = [\Delta V_{km,1} \cdots \Delta V_{km,N_c}]^t$, $\mathbf{I}_{km} = [I_{km,1} \cdots I_{km,N_c}]^t$, $\mathbf{X}_c = [\mathbf{X}_1 \cdots \mathbf{X}_{N_c}]^t$, $\mathbf{A}_c = diag\,(\mathbf{A}_1, \ldots, \mathbf{A}_{N_c})$, $\mathbf{B}_c = diag\,(B_1, \ldots, B_{N_c})$, $\mathbf{C}_c = diag\,(\mathbf{C}_1, \ldots, \mathbf{C}_{N_c})$, $\mathbf{D}_c = diag\,(D_1, \ldots, D_{N_c})$ and N_c is the number of series connection

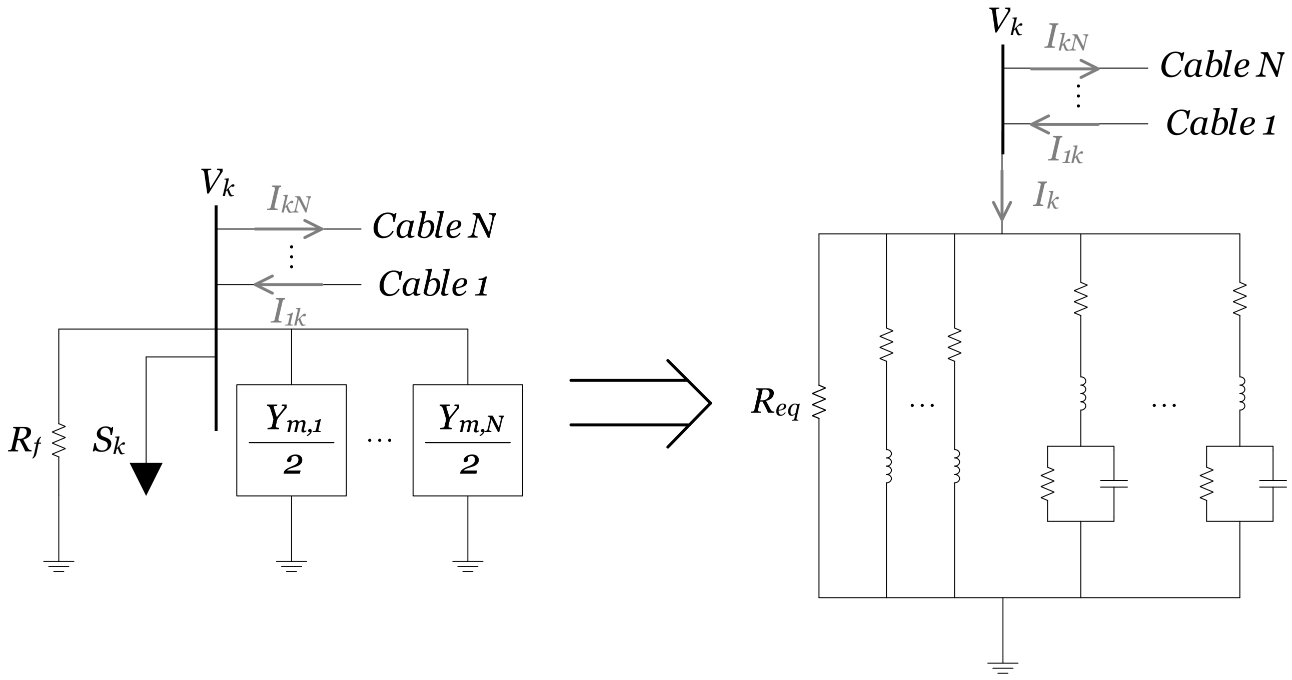

Figure 3.7: Busbar shunt aggregated state-space model

elements in the system.

$$\begin{cases} s\mathbf{X}_b = \mathbf{A}_b\mathbf{X}_b + \mathbf{B}_b\mathbf{I}_b \\ \mathbf{V}_b = \mathbf{C}_b\mathbf{X}_b + \mathbf{D}_b\mathbf{I}_b \end{cases} \tag{3.30}$$

$$\begin{cases} s\mathbf{X}_c = \mathbf{A}_c\mathbf{X}_c + \mathbf{B}_c\mathbf{\Delta V}_{km} \\ \mathbf{I}_{km} = \mathbf{C}_c\mathbf{X}_c + \mathbf{D}_c\mathbf{\Delta V}_{km} \end{cases} \tag{3.31}$$

To compute the state-space representation of the grid, it is necessary to combine equations (3.30) and (3.31) by considering the balancing matrices ξ_i and ξ_v derived from the branch and nodal Kirchhoff's laws as:

$$\mathbf{I}_b = \xi_i\mathbf{I}_{km} \tag{3.32}$$

$$\mathbf{\Delta V}_{km} = \xi_v\mathbf{V}_b + \xi_{in}\mathbf{V}_{in} \tag{3.33}$$

Using identities (3.32) and (3.33), together with the state-space representations of $Z_{m,i}^{-1}(s)$ and

$Y_{m,i}(s)/2$, the grid's state-space representation can be defined as follows:

$$\begin{cases} s\begin{bmatrix}\mathbf{X}_b\\ \mathbf{X}_c\end{bmatrix} = \mathbf{A}_{grid}\begin{bmatrix}\mathbf{X}_b\\ \mathbf{X}_c\end{bmatrix} + \mathbf{B}_{grid}\mathbf{V}_{in} \\ \begin{bmatrix}\mathbf{V}_b\\ \mathbf{I}_{km}\end{bmatrix} = \mathbf{C}_{grid}\begin{bmatrix}\mathbf{X}_b\\ \mathbf{X}_c\end{bmatrix} + \mathbf{D}_{grid}\mathbf{V}_{in}\end{cases} \tag{3.34}$$

where

$$\mathbf{A}_{grid} = \begin{bmatrix}\mathbf{A}_b & \\ & \mathbf{A}_c\end{bmatrix} + \begin{bmatrix} & \mathbf{B}_b\xi_i\\ \mathbf{B}_c\xi_v & \end{bmatrix}\begin{bmatrix}\mathbf{I} & -\mathbf{D}_b\xi_i\\ -\mathbf{D}_c\xi_v & \mathbf{I}\end{bmatrix}^{-1}\begin{bmatrix}\mathbf{C}_b & \\ & \mathbf{C}_c\end{bmatrix}$$

$$\mathbf{B}_{grid} = \begin{bmatrix}\mathbf{0}\\ \mathbf{B}_c\xi_{in}\end{bmatrix} + \begin{bmatrix} & \mathbf{B}_b\xi_i\\ \mathbf{B}_c\xi_v & \end{bmatrix}\begin{bmatrix}\mathbf{I} & -\mathbf{D}_b\xi_i\\ -\mathbf{D}_c\xi_v & \mathbf{I}\end{bmatrix}^{-1}\begin{bmatrix}\mathbf{0}\\ \mathbf{D}_c\xi_{in}\end{bmatrix}$$

$$\mathbf{C}_{grid} = \begin{bmatrix}\mathbf{I} & -\mathbf{D}_b\xi_i\\ -\mathbf{D}_c\xi_v & \mathbf{I}\end{bmatrix}^{-1}\begin{bmatrix}\mathbf{C}_b & \\ & \mathbf{C}_c\end{bmatrix}$$

$$\mathbf{D}_{grid} = \begin{bmatrix}\mathbf{I} & -\mathbf{D}_b\xi_i\\ -\mathbf{D}_c\xi_v & \mathbf{I}\end{bmatrix}^{-1}\begin{bmatrix}\mathbf{0}\\ \mathbf{D}_c\xi_{in}\end{bmatrix}$$

In the next section, the response of the proposed state-space impedance model for underground cables is compared with EMT simulations performed in PSCAD.

3.4 Numerical results

To test and compare the proposed impedance modelling methodology, a 11 kV three-phase cable test system was built in PSCAD, as shown in Figure 3.8. The cable model used for the time-domain simulations is the *Frequency Dependent (Phase) Model*, which implements the ULM scheme.

The cable's characteristics are summarized in Table 2.2, and the system parameters are presented in Table 2.3. Regarding the time-domain simulation parameters, the time-step is $\epsilon = 2\ \mu$s, the simulation duration is $t_{tot} = 0.1$ s and the sampling time is $t_s = 2\ \mu$s.

In what follows, firstly results of the proposed admittance transfer functions' approximation and modelling are shown. Secondly, a time-domain comparison is made between the PSCAD model and the proposed state space model implemented in Simulink. These last results correspond to a three-phase fault occurring at the middle of cable h1.

3.4.1 Impedance modelling results

Using the cable data presented in Table 2.2, $Z_{m,i}^{-1}(s)$ and $Y_{m,i}(s)/2$ are calculated using the wave parameters $\mathbf{H}_m(s)$ and $\mathbf{Y}_{cm}(s)$, which are computed following the same procedure as PSCAD's *Solve Cable Constants* routine. To perform the rational approximation for the travelling delays $\tau_{m,i}$, a Padé approximation of order $N_d = 10$ is considered.

As it is possible to see from Figures 3.9 to 3.12, the rational approximation is very accurate both in magnitude and phase up to around 100 kHz. From the rational approximations, an equivalent impedance circuit was derived together with a state space model for the cable test network as described in the previous sections. The state space model was implemented in Simulink and compared with time-domain results obtained in PSCAD.

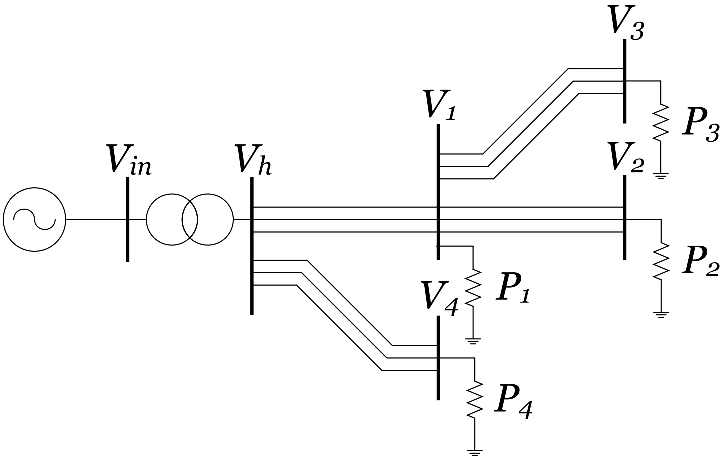

Figure 3.8: PSCAD cable test system.

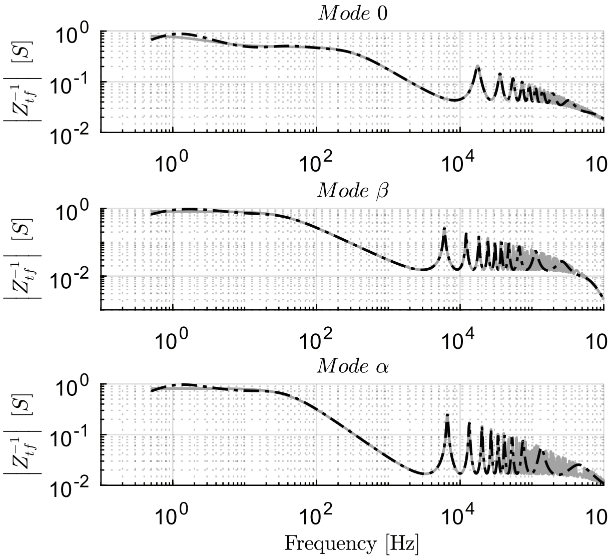

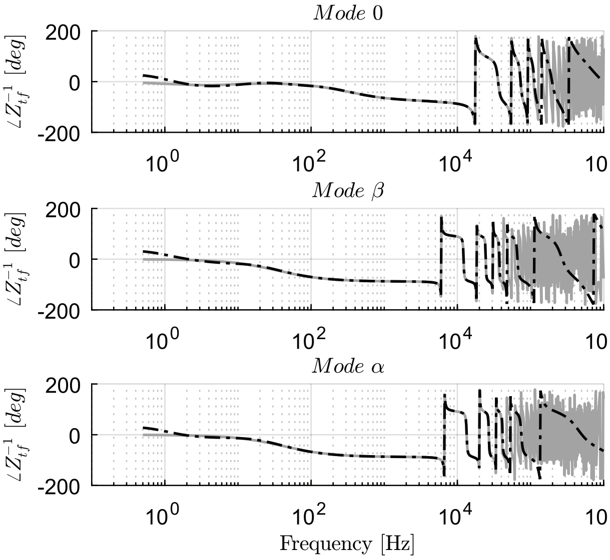

Figure 3.9: Magnitudes of cable h1 admittance transfer function $Z_{m,i}^{-1}(s)$. In solid gray line the theoretical values and in dotted black line the proposed rational approximation.

Figure 3.10: Phase angles of cable h1 admittance transfer function $Z_{m,i}^{-1}(s)$. In solid gray line the theoretical values and in dotted black line the proposed rational approximation.

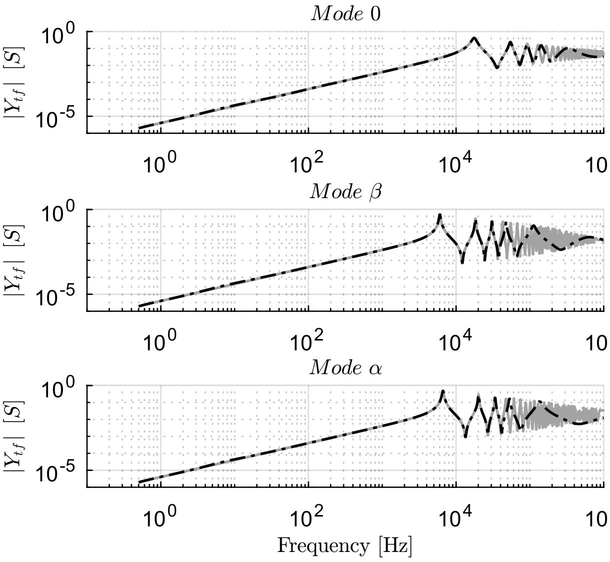

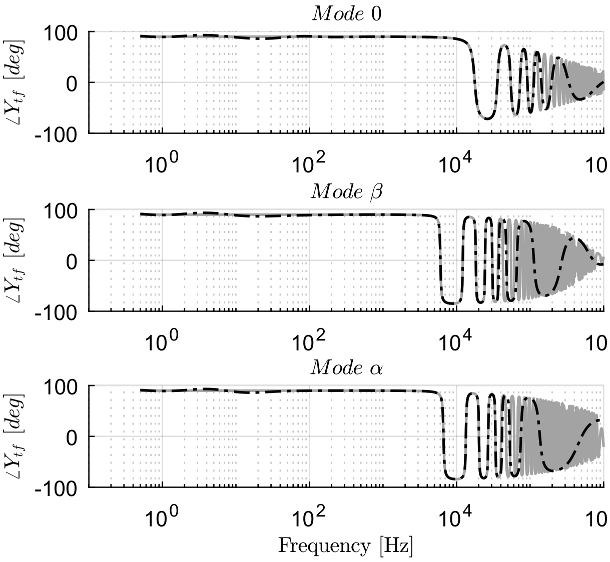

Figure 3.11: Magnitudes of cable h1 admittance transfer function $Y_{m,i}(s)/2$. In solid gray line the theoretical values and in dotted black line the proposed rational approximation.

Figure 3.12: Phase angles of cable h1 admittance transfer function $Y_{m,i}(s)/2$. In solid gray line the theoretical values and in dotted black line the proposed rational approximation.

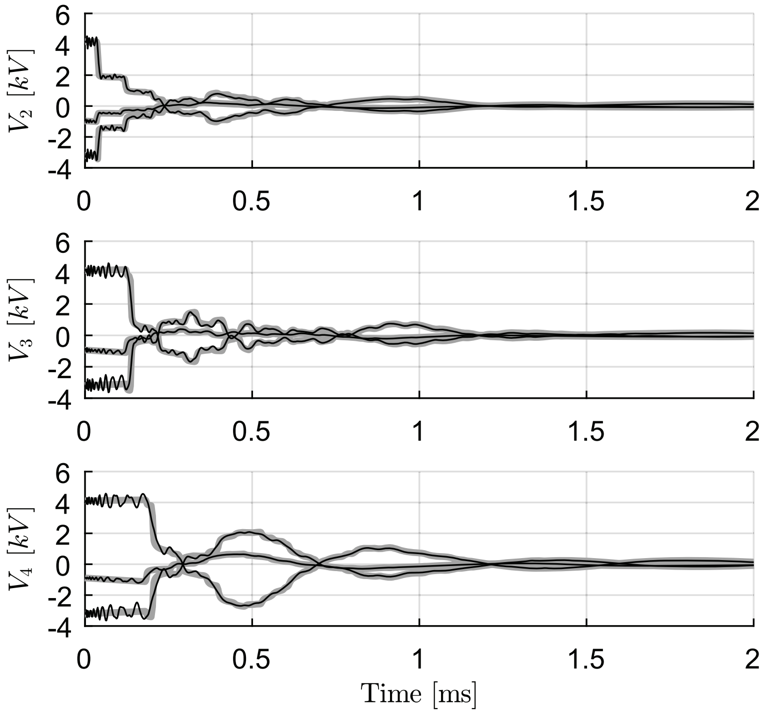

Figure 3.13: Transient three-phase voltages at busbars 2, 3 and 4 immediately after a three-phase fault. In solid gray line the PSCAD results and in solid black line the proposed impedance-based state space model.

3.4.2 Time-domain comparison

To compare the accuracy of the proposed cable impedance modelling, the state space model implemented in Simulink is tested during a three-phase fault. More specifically, at the simulation time $t_f = 0.08$ s, a three-phase to ground fault with a resistance of 0.05 Ω occurs at the middle of cable h1. The obtained results are shown in Figure 3.13.

From Figure 3.13, it is possible to see that the time-domain results obtained using the proposed impedance modelling closely match the ones obtained in PSCAD. The transient response of both models are very similar except for the very high frequency behaviour as expected. This corroborates that this impedance-based approach could be useful to complement transient studies performed using EMT simulations. By considering the state-space formulation derived from the cable impedance model, it is possible to identify the dominant oscillatory modes defining the transient response, together with their frequencies and damping coefficients. This can be computed from the state space matrix A_{grid} in equation (3.34) using eigenvalue analysis, providing a fast tool for transient characteristics screening before performing more detailed

EMT simulations.

In this chapter, an LTI impedance representation or cable/line sections is provided. The proposed impedance representation is able to accurately model the cable/lines' frequency-dependent electrical parameters up to the 100 kHz range, which was one of the main requirements to develop a new fault location methodology based on system's intermediate frequency transient response as described in Chapter 2. In the next chapter, the details of such fault location methodology are described by considering the proposed LTI impedance representation for cable/line sections.

CHAPTER 4

Fault Location Methodology

The proposed fault location methodology using the fault's transient intermediate frequency response can be divided in two parts, as shown in Figure 4.1. First, an offline characterization methodology is used to obtain the polynomial approximations of the intermediate frequencies' dependency on different fault location scenarios. This offline characterization stage is simulation-based, and it takes as inputs the known topology and electrical parameters of the system components. The outputs of this stage are the polynomial coefficients defining the intermediate frequencies' fault location dependence, which can be stored on a database for later use in the real-time fault location process.

The real-time fault location process is performed in a second stage. This online fault location process uses the polynomial approximations previously computed in the first offline stage. Here, the aim is to solve the polynomial equations to obtain the estimated fault location, by using as inputs the measured intermediate frequencies of the network's transient response. These frequencies can be obtained by using signal processing techniques such as the Fast Fourier Transform (FFT) on the sampled voltage or current signals measured at the time of the fault occurrence. The objective of the proposed fault location methodology is to tackle most of the modelling complexity in the offline stage, while maintaining the online process fast, simple and applicable to realistic networks. The offline and online stages are described in the next sections.

4.1 Offline characterization

The offline characterization stage needs to first identify the intermediate frequencies present in the transient response of the network for different fault location scenarios. More specifically, the transient frequency response of the network needs to be computed for different fault locations within each cable/line section in the system. The intermediate frequencies are thus identified in an iterative process over the cable/line sections of the grid. For each j^{th} cable/line section, different fault locations are simulated at different percentages $\{k_{1j}, \ldots, k_{ij}, \ldots, k_{N_j j}\}$ of the total section length. For faults occurring in the j^{th} section, there will be a set $\mathcal{F}_j = \{\omega_{1j}(k), \ldots, \omega_{N_j j}(k)\}$ of intermediate frequencies that define the transient frequency response of the system.

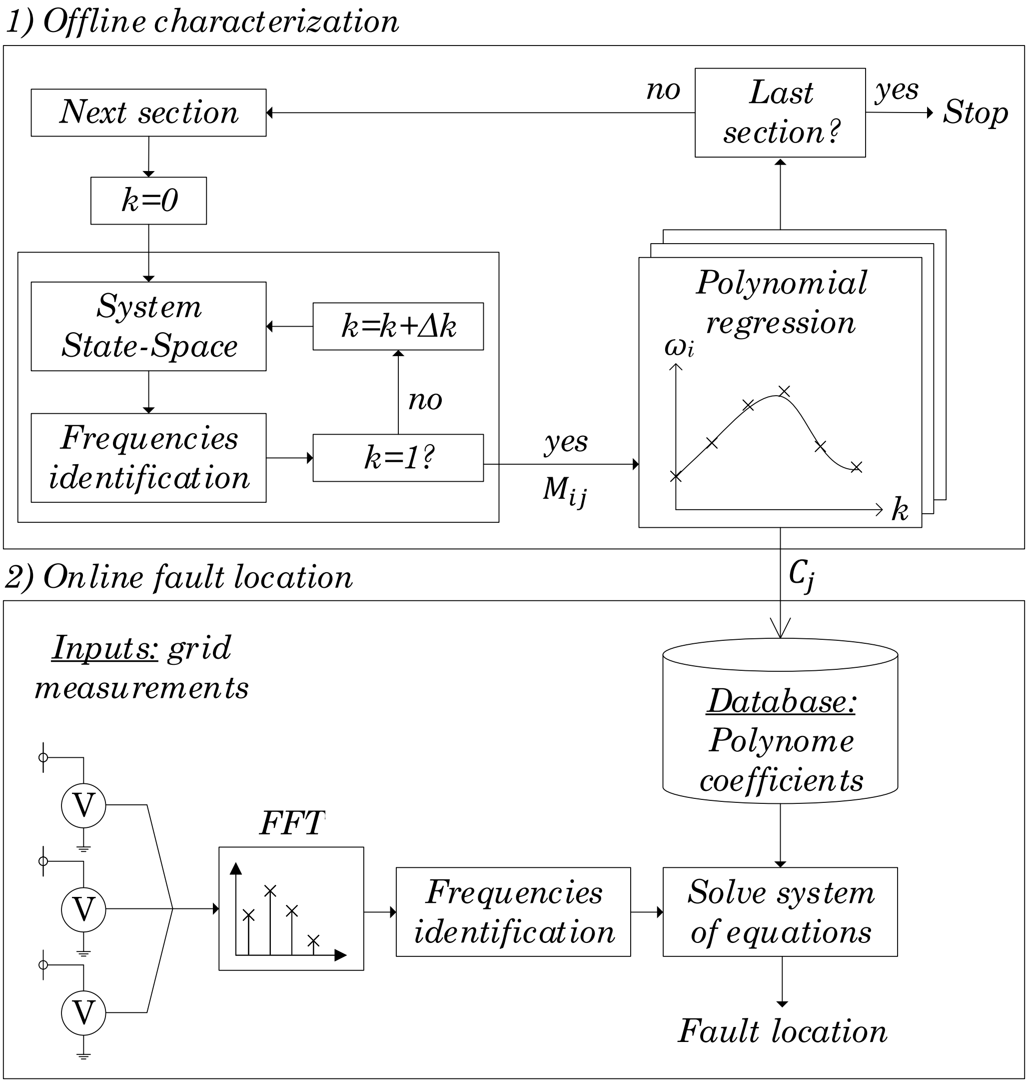

Figure 4.1: Proposed fault-location methodology

In the simplest case shown in Figure 2.4, each cable/line being represented by a lumped Π-section has a unique intermediate frequency defining its transient response. It is, however, well-known that a line/cable's frequency behaviour is defined by transcendental functions having an infinite number of poles [77,78]. Using the LTI admittance model presented in Chapter 3, each j^{th} cable/line section is represented by a sum of rational function of $\tilde{N}_j$ poles. Thus, each j^{th} cable/line section's transient response is defined by $N_j \leq \tilde{N}_j$ intermediate frequencies, where N_j is the number of pairs of complex poles.

When modelling a realistic network with N_s cable/line sections by using the proposed LTI admittance model, a total of $N = \sum_j^{N_s} N_j$ intermediate frequencies can be computed. These intermediate frequencies correspond to the imaginary parts of the eigenvalues $\{\lambda_1(k), \ldots . \lambda_N(k)\}$

computed from the system's state-space matrix $\mathbf{A}_{grid,f}(k)$ under faulted condition, defined according to equation (3.34) for a fault location k. From the set $\mathcal{F}_j$ of all intermediate frequencies, only a subset will be observable in each measured frequency response of voltage and current signals in the grid. Indeed, the presence of each intermediate frequency in the measured frequency responses $V_n(s = j\omega)$ and $I_n(s = j\omega)$ of voltage and current signals across the grid is defined by equation (4.1), where the system transitions from a non-faulted condition defined by the state-space matrices $\{\mathbf{A}_{grid,pf}(k), \mathbf{B}_{grid,pf}(k), \mathbf{C}_{grid,pf}(k), \mathbf{D}_{grid,pf}(k)\}$, to the faulted condition defined by the state-space matrices $\{\mathbf{A}_{grid,f}(k), \mathbf{B}_{grid,f}(k), \mathbf{C}_{grid,f}(k), \mathbf{D}_{grid,f}(k)\}$. In equation (4.1), $\mathbf{X}_{pf,t_f}$ corresponds to the initial condition of the state-variables of the system at the time of the fault occurrence $t = t_f$ in the non-fault condition, $\mathbf{C}_{grid,f}(n)$ corresponds to the n^{th} row of $\mathbf{C}_{grid,f}$ and $\mathbf{A}_{grid,f}(k) = \mathbf{T}_f \mathbf{\Lambda}_{grid,f}(k) \mathbf{T}_f^{-1}$ is the eigenvalue decomposition of matrix $\mathbf{A}_{grid,f}(k)$. From equation (4.1), it is possible to see that there is a steady-state term $V_{n,ss}(s)$ which corresponds to the forced response of the system to the input voltages at the fundamental frequency ω_0, and a transient term $V_{n,tr}(s)$. It is in this transient term where the contribution of the different intermediate frequencies can be measured. It is thus clear that the contribution of each intermediate frequency to the transient frequency response of each voltage signal will depend on the initial conditions $\mathbf{X}_{pf,t_f}$ and the output matrix $\mathbf{C}_{grid,f}(n)$.

$$
\begin{aligned}
V_n(s) &= \mathbf{C}_{grid,f}(n)\mathbf{T}_f(s\mathbf{I} - \mathbf{\Lambda}_{grid,f}(k))^{-1}\mathbf{T}_f^{-1}\mathbf{X}_{pf,t_f} \\
&\quad + \left(\mathbf{C}_{grid,n}\mathbf{T}_f(s\mathbf{I} - \mathbf{\Lambda}_{grid,f}(k))^{-1}\mathbf{T}_f^{-1}\mathbf{B}_{grid,f} + \mathbf{D}_{grid,f}\right) V_{in,t_f}(s) \qquad (4.1) \\
\Leftrightarrow V_n(s) &= V_{n,tr}(s) + V_{n,ss}(s)
\end{aligned}
$$

From the previous analysis, a frequency identification procedure needs to be established in order to determine the intermediate frequencies of interest present in the n^{th} transient frequency response signal $V_n(j\omega)/I_n(j\omega)$. It is important to note that this frequency identification procedure will be used both in the offline characterization stage and in the online fault location process as shown in Figure 4.1. To ensure the accuracy and consistency of the proposed methodology, the intermediate frequencies identified in the offline stage need to match the ones measured during the real time fault location process. It is thus necessary to implement the same frequency identification procedure in both stages, which should be an accurate yet simple and fast computational process in favour of the real time fault location method's efficiency.

The most accurate procedure would be to apply the vector fitting algorithm to the measured transient frequency response signals $\hat{V}_n(j\omega)$, which would allow to identify their poles and thus the intermediate frequencies defining the transient response of the system. This process, however, is not simple to implement systematically for all possible measured frequency responses signals, since the vector fitting process usually requires fine tuning of its input parameters to achieve an accurate system identification. Examples of such parameters are the weights used to assign relative importance to each frequency point of the input frequency response data, the total number of poles to perform the fitting and the presence of constant terms. An alternative considered in the proposed methodology, is to identify the frequencies associated with the peak values of each frequency response magnitude data $|V_n(j\omega)|$. Indeed, it is expected that for a given frequency response $V_n(j\omega)$, the intermediate frequencies originated from the transient response of the cable/line sections connected to that respective measuring point will not only be directly observable, but they should also have the largest contribution to its transient frequency response, which reflects as peak values in its magnitude at those respective frequencies.

The main advantage of the aforementioned frequency identification procedure is its simplicity to implement systematically for all measured frequency response data. In the case of the offline characterization stage, the theoretical frequency response $V_n(j\tilde{\omega})$ can be computed using equation (4.1), by evaluating it at $s = j\tilde{\omega}_i$ where $\mathcal{W}_{FFT} = \{\tilde{\omega}_1, \ldots, \tilde{\omega}_{N_{FFT}}\}$ is the the set of available frequencies to compute the FFT of the measured signals, defined by the sampling frequency and resolution of the measuring devices in the grid. In order to compute the expected frequency response data $V_n(j\tilde{\omega})$ theoretically, it is also necessary to consider an initial condition $\mathbf{X}_{pf,t_f}$. In the case of a radial distribution network with an input voltage $V_{in}(t) = V_0 \cdot \sin(\omega_0 t)$ at the distribution substation, the initial conditions for a fault occurring at time $t = t_f$ can be computed using equation (4.2). For more complex meshed networks with multiple voltage source inputs it is possible to compute the initial conditions of the inductor currents and capacitor voltages by solving the steady-state load flow condition of the network in the pre-faulted state, using standard iterative method such as the Newton-Raphson algorithm. For the rest of this thesis a radial network is considered and thus the initial conditions are computed using equation (4.2). It is also worth noting that the dependence of the frequency response on the fault time t_f is not significant, in the sense that it won't change its frequency content since matrix $\mathbf{A}_{sys,f}(k)$ will remain unaffected. Instead, the fault time will define the overall magnitude of the voltages and currents in the network at the time of the fault occurrence.

$$\mathbf{X}_{pf,t_f} = V_0 \mathbf{T}_{pf} \left(sin(\omega_0 t_f) \mathbf{\Lambda}_{grid,pf}(k) + \omega_0 \cdot cos(\omega_0 t_f) \mathbf{I} \right) \left(\mathbf{\Lambda}^2_{grid,pf}(k) + \omega_0^2 \mathbf{I} \right)^{-1} \mathbf{T}^{-1}_{pf} \mathbf{B}_{grid,pf} \quad (4.2)$$

It is worth noting that, when performing the frequency identification on the estimated frequency response, only the peak values below a critical frequencies f_c should be considered to ensure good accuracy in accordance with the rational approximations of the line/cables impedance behaviour. More specifically, the impedance/admittance representations defined in Chapter 3 considered to establish the state-space, are accurate up to a critical frequency f_c as shown Figure 4.2. Since the modal travelling delay τ_i is approximated by a Padé approximant, the rational approximations of the impedance transfer functions are accurate up to the critical frequency f_c. In this case, the critical frequency is identified based on a predetermined error threshold σ_e between the theoretical values and the fitted ones as shown in Figure 4.2. An example of the upper bound f_c is shown with a solid black line in Figure 4.3. It is also important to consider the dominant frequencies above the fundamental frequency f_0 and some of its harmonics, since those frequencies don't correspond to the transient response of the cable system but rather with its forced response.

The set of theoretical intermediate frequencies $\mathcal{M}_{ij} = \{(k_1, w_{ij}(k_1)), \ldots, (k_{N_d}, w_{ij}(k_{N_d}))\}$ can then be constructed by iteratively extracting the frequency response's peak values for each fault scenario k_n. The number of theoretical values is defined by the section's length partitioning according to Δk. Thus, Δk must be selected to have enough data points to achieve the desired polynomial regression accuracy while keeping a reasonable computation time of the offline methodology. More data points allow to perform higher order polynomial regressions with better accuracy at the cost of more computation time. In the authors' experience, good results can be achieved by considering 15 data points.

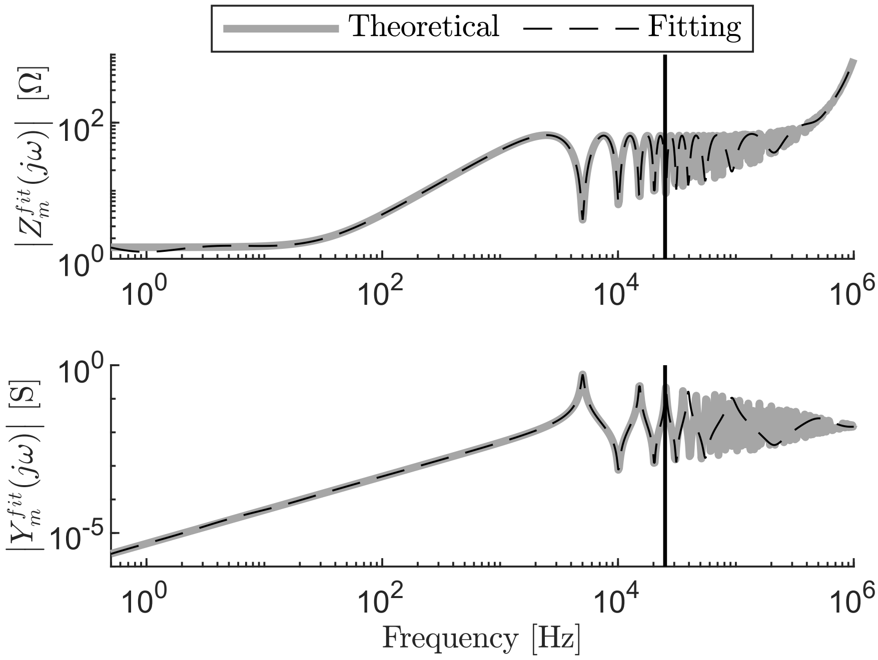

Figure 4.2: Exact Π-section $Z_m^{fit}(s)$ and $Y_m^{fit}(s)$ approximations examples in the modal domain. The solid grey line represents the theoretical values, the dashed black line the fitted approximation and the solid vertical black line is the critical frequency.

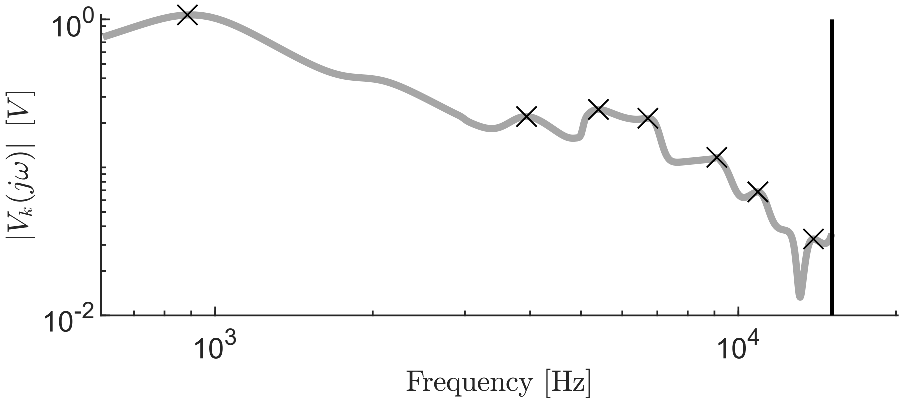

Figure 4.3: Dominant intermediate frequencies estimated from voltage's frequency response.

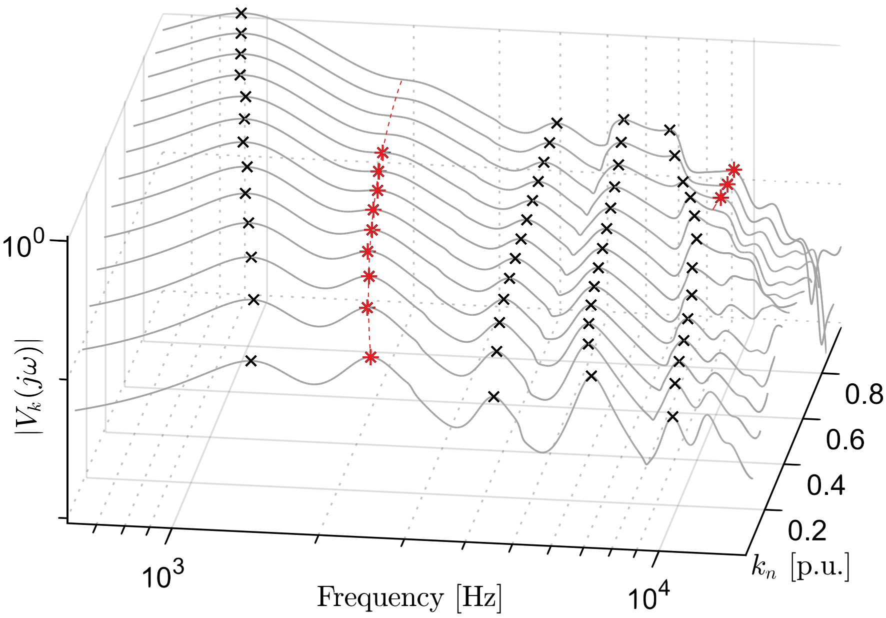

Figure 4.4: Dominant intermediate frequencies tracking over different fault location scenarios on the same cable/line section. Black crosses correspond to consistent peaks across all fault locations. Red stars correspond to inconsistent peak values, not present in all fault locations.

One last point to consider in this process is that not all intermediate frequencies correspond to peak values of the voltages' frequency responses across all fault scenarios k_n. This is represented in the example shown in Figure 4.4, where the black crosses correspond to intermediate frequencies that consistently represent peak values of the voltage's frequency response for all fault location scenarios k_n. The red stars on the other hand correspond to intermediate frequencies that represent peak values in some fault location cases, but not in all of them. These intermediate frequencies must thus be identified and filtered out after computing the peak values for all fault scenarios k_n within the j^{th} cable/line section.

Finally, once the set $\mathcal{M}_{ij}$ is computed, each intermediate frequency fault location dependency $\omega_{ij}(k)$ can be fitted using a polynomial regression $\hat{\omega}_{ij}(k)$. Each polynomial fitting can be stored as the set of its coefficients $\mathcal{C}_{ij} = \left\{a_{ij1}, \ldots, a_{ijN_{ij}}\right\}$, where N_{ij} is the order of each polynomial regression. These coefficients are the main outcome of the offline characterization methodology in order to solve the fault location problem, as it is explained in the next section. The coefficients can be further grouped for the j^{th} section as $\mathcal{C}_j = \{\mathcal{C}_{1j}, \ldots, \mathcal{C}_{Nj}\}$.

This offline methodology must be performed for each topology and pre-fault condition of interest. This in turn means that the offline methodology should be updated each time a topological change is performed, i.e. new lines, loads or generators are connected to the grid. The model is also accurate for a specific pre-fault condition. Different load values will impact on the damping of the transient response of the system, thus modifying the shape of the frequency spectrum being measured and the location of the identified peaks in the FFT magnitude. An option to address this issue would be to consider and compute different fault location characterization polynomials for different loading conditions of the system, which is usually known data by DSO as a function of the time of the day and season. Despite of this, the proposed offline methodology has two advantages in comparison with other simulation-based approaches. Firstly, the offline characterization can be performed for each cable/line section independently, which means it could be performed in parallel, greatly reducing computational time and improving its scalabilty for larger systems. Secondly, simulation-based methods that match time-domain simulations with field measurements must consider different fault inception angle conditions. The proposed offline methodology relies only in the intermediate frequency of oscillations during the transient response of the system and thus doesn't need to consider different fault inception angle conditions. Further research can be done to optimize the proposed offline methodology, for example by applying model order reduction techniques when defining the LTI representation of the system, making it more tractable without compromising its accuracy.

4.2 Online fault location

The offline characterization methodology is designed to tackle most of the modelling and analysis complexity to solve the fault location problem. This in turn allows the online fault location method to remain simple in its implementation and applicability.

The first step to perform the real-time fault location is to obtain the time-domain waveforms of the transient voltages $\tilde{V}_n(t)$ generated immediately after the occurrence of a fault in the system. Using traditional FFT techniques, together with the necessary windowing and filtering processes to discard high-frequency noise and to avoid spectral leakage, the measured frequency response $\tilde{V}_n(j\omega)$ for each measured voltage waveform is computed.

In a second step, the measured dominant intermediate frequencies $\tilde{\omega}_i$ for each transient measurement are identified using the same peak-value identification process used in the offline characterization methodology. The peak identification procedure is performed in the magnitude of the measured frequency response $\left|\tilde{V}_n(j\omega)\right|$, where the numerical derivative $\Delta_k \left|\tilde{V}_n(j\omega)\right|$ is computed between two consecutive measurements k and $k+1$. A peak or valley value can be identified by checking when the numerical derivative is close to zero according to a user defined threshold ϵ_p, i.e. when $\left|\Delta_k \left|\tilde{V}_n(j\omega)\right|\right| < \epsilon_p$. Peak values are then identified by comparing them with their neighbouring measurement points $k-1$ and $k+1$, and then taking the ones that are greater than both. As mentioned in the previous section, it is worth mentioning that each intermediate frequency $\tilde{\omega}_i$ won't be observable in all measured voltage waveforms $\tilde{V}_n(t)$. The dominant intermediate frequencies in each voltage waveform $\tilde{V}_n(t)$ depend, however, on their respective participations to each voltage's transient response. In order to have full observability of all dominant intermediate frequencies $\tilde{\omega}_i$, an optimization problem can be defined to establish the optimal allocation of the measuring devices in the grid across a set of credible and/or critical fault location scenarios. This problem however is not tackled in this work and remains open for future research. In what follows of the online methodology, it is assumed that enough measurement devices are available to identify the dominant intermediate frequencies.

Once the dominant intermediate frequencies $\tilde{\omega}_i$ have been identified, they can be used to solve the fault location problem. This is done by identifying the faulted section and the fault location $\hat{k}$ within said section. This can be done by solving the system of polynomial equations $\mathcal{C}_j$ obtained while considering a fault occurring in each j^{th} section as defined in equation (4.3). In this case, if the j^{th} section has N_j set of polynomial equations $\hat{\omega}_i(k)$, and there are N_f measured dominant intermediate frequencies $\tilde{\omega}_i$, then there is a total of $N_j \times N_f$ equations to solve. When the polynomial regressions being solved are the ones that were obtained for a fault scenario that simulated the actual faulted section, then there will be a cluster $\Omega = \left\{\tilde{k}_1, \ldots, \tilde{k}_{N_f}\right\}$ of fault location estimates around the value of the real fault location $\hat{k}$. Such a cluster will not exist when considering the polynomial regressions obtained for fault scenarios simulated in other cable/line sections. While this might not be obvious from equation (4.3), an example is provided in Figure 4.5. In the example, a set of four measured dominant intermediate frequencies $\tilde{\omega}_i$

are considered. When solving the polynomial regressions obtained when simulating the actual faulted section there is a cluster of solutions around the real fault location value. This is not the case when considering the polynomial equations associated with a different faulted section scenario, where multiple estimates of the location do not provide a clear cluster.

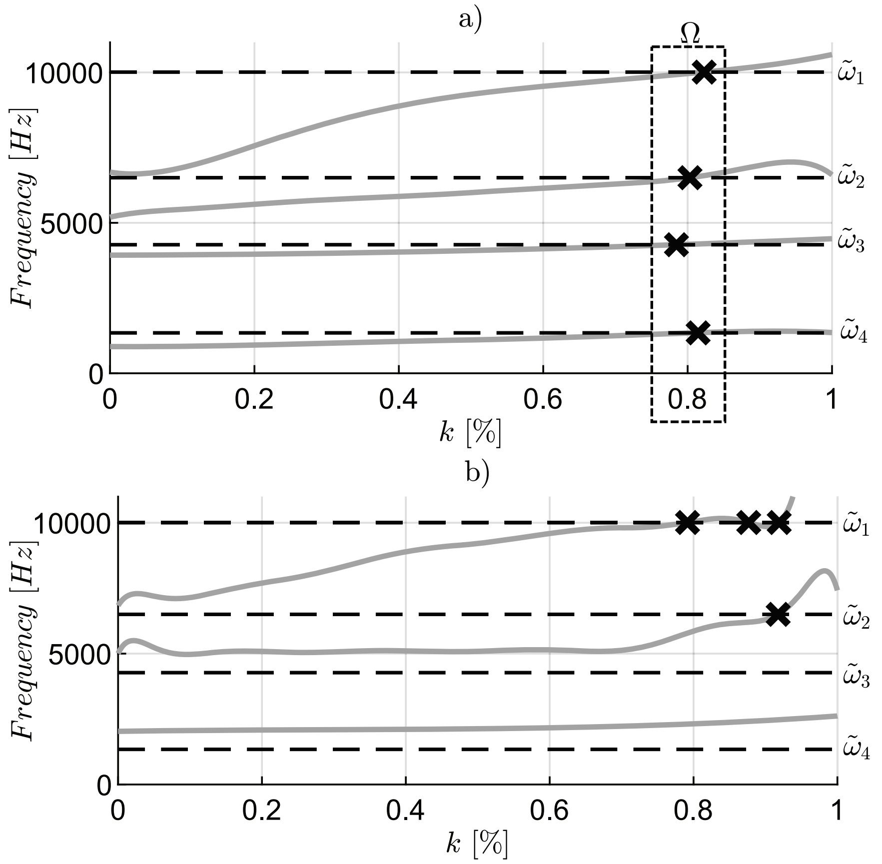

Figure 4.5: Example of polynomial solutions for set of measured frequencies $\tilde{\omega}_i$: a) Equations obtained for scenario of faulted section, b) Equations obtained for scenario of non-faulted section.

$$\begin{gathered}
\hat{\omega}_1(k) = a_{11} + \ldots + a_{1N_1} k^{N_1-1} = \tilde{\omega}_1 \\
\vdots \\
\hat{\omega}_1(k) = a_{11} + \ldots + a_{1N_1} k^{N_1-1} = \tilde{\omega}_{N_f} \\
\vdots \\
\hat{\omega}_{N_j}(k) = a_{N_j1} + \ldots + a_{N_jM} k^{M-1} = \tilde{\omega}_1 \\
\vdots \\
\hat{\omega}_{N_j}(k) = a_{N_j1} + \ldots + a_{N_jM} k^{M-1} = \tilde{\omega}_{N_f}
\end{gathered} \tag{4.3}$$

The online fault location can thus be performed by solving the set of polynomial regressions of each cable/line section using the measured intermediate frequencies until a cluster of solutions is found. The cluster of solutions should be defined by finding at least one solution per polynomial regression, and having all the solutions within a maximum distance deviation threshold Δk_j predefined beforehand. In the next section, numerical results are provided when the methodology is tested using EMT cable models in PSCAD.

4.3 Study case and numerical results

To test the proposed fault location methodology, a 11 kV three-phase cable test system was built in PSCAD, as shown in Figure 4.6. The cable model used for the time-domain simulations is the *Frequency Dependent (Phase) Model*, which implements the ULM scheme. The cable's characteristics are summarized in Table 4.1, and the system parameters are presented in Table 4.2. Two transformers are modelled using their T-models, i.e. a shunt branch to represent their magnetizing properties and two series branches two account for the leakage reactances and resistances. Loads are represented using realistic dynamic ERLM models as defined in [79]. More specifically, each load's dynamic behaviour is defined in PSCAD by equations (4.4) and (4.5), where all loads have the same paramaters $\alpha_s = 0.38$, $\alpha_t = 2.26$, $T_{pr} = 2.26\ s$, $\beta_s = 2.68$, $\beta_t = 5.22$ and $T_{qr} = 70\ s$ according to [79].

$$\begin{aligned}
&\dot{P}_r + T_{pr}P_r = P_s - P_t \\
&P = P_r + P_{tr} \\
&P_s(V) = P_0\left(\tfrac{V}{V0}\right)^{\alpha_s} \\
&P_t(V) = P_0\left(\tfrac{V}{V0}\right)^{\alpha_t}
\end{aligned} \tag{4.4}$$

$$\begin{aligned}
&\dot{Q}_r + T_{qr}Q_r = Q_s - Q_t \\
&Q = Q_r + Q_{tr} \\
&Q_s(V) = Q_0\left(\tfrac{V}{V0}\right)^{\beta_s} \\
&Q_t(V) = Q_0\left(\tfrac{V}{V0}\right)^{\beta_t}
\end{aligned} \tag{4.5}$$

From equations (4.4) and (4.5), it is possible to obtain the time-domain behaviour of loads immediately after the occurrence of a fault at time t_f as defined by equations (4.6) [79], where a voltage drop occurs from from the steady-state value V_s to the fault value V_f.

$$
\begin{aligned}
&P(t) = P_s(V_f) + [\Delta P(V_s) - \Delta P(V_f)]\, e^{\frac{-(t-t_f)}{T_{pr}}} \\
&Q(t) = Q_s(V_f) + [\Delta Q(V_s) - \Delta Q(V_f)]\, e^{\frac{-(t-t_f)}{T_{qr}}} \\
&\Delta P(V) = P_s(V) - P_t(V) \\
&\Delta Q(V) = Q_s(V) - Q_t(V)
\end{aligned}
\tag{4.6}
$$

To represent the load behaviour in the LTI representation of the grid in the offline characterization, two key aspects need to be considered:

- The time response of the loads is much slower than the transient response of the cable/line system. The transient behaviour of the intermediate frequencies occurs within the μs range, while the load dynamics is in the s range which means that $e^{\frac{-(t-t_f)}{T_{pr}}} \approx 1$.
- The voltage drop from V_s to V_f is not instantaneous. While this is the case in RMS simulation, in the EMT case the rate of change of voltages across the grid is limited by the grid's dynamics, i.e. it's inductances and capacitances. More importantly, immediately after the fault occurrence and during the first μs when the intermediate frequencies' transient behaviour is dominating, it can be considered that $V_f \approx V_s \Rightarrow \Delta P(V_s) \approx \Delta P(V_f)$.

With the previous two considerations, for the purposes of the offline characterization the loads can be considered as static and defined by equations (4.7), where the steady-state voltages V_s can be computed from the load-flow solutions for the grid on a given operating condition. In general, these values will be constrained to a narrow operational band around 1.0 pu as defined by each country's grid code.

$$
\begin{aligned}
P(t) = P_s(V_s) \Rightarrow R = \tfrac{V_s^2}{P_s(V_s)} \\
Q(t) = Q_s(V_s) \Rightarrow X = \tfrac{V_s^2}{Q_s(V_s)}
\end{aligned}
\tag{4.7}
$$

The time-domain simulations are performed in PSCAD considering a the time-step of $\epsilon = 2$ μs

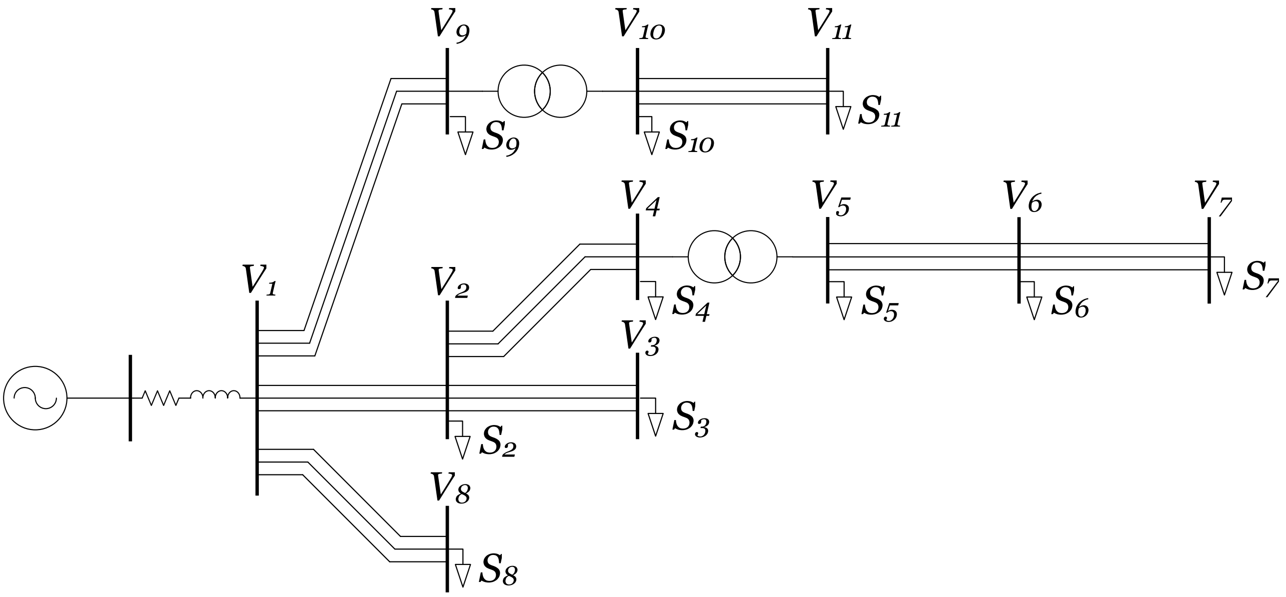

Figure 4.6: PSCAD cable test system.

and a sampling frequency of 30 kHz. The offline characterization of a single cable section takes approximately 23 min in a Intel Core i7-10750 CPU of 2.6 GHz, with a total RAM usage of 2.4 GB. While this time and memory consumption can be improved with code optimization, from a theoretical perspective the computational burden comes from the matrices' size of the LTI state-space representation of the system. To improve the scalability of the proposed methodology to bigger systems, future work needs to be done to reduce the order of the LTI models while preserving its accuracy for the purposes of the offline characterization.

To test the proposed fault location methodology, three fault scenarios are considered:

1. Scenario 1: three-phase fault with $R_f = 0.2\ \Omega$ at 30% of cable 2-3
2. Scenario 2: three-phase fault with $R_f = 2\ \Omega$ at 80% of cable 1-2
3. Scenario 3: three-phase fault with $R_f = 20\ \Omega$ at 50% of cable 5-6

For each fault scenario, 40 ms of the transient voltage waveforms are recorded with a sampling frequency of 30 kHz and then processed in Matlab. A blackman windowing is applied to the sampled signals and the FFT is computed. Since the modelling of the cable system is done in the modal domain using the state-space representation described in Chapter 3, the voltage waveforms are transformed to the modal domain using the Clarke transform to be consistent

Table 4.1: Test case cable Data

Parameters	**Value**
Configuration	Three cables flat
Cable separation	0.5 m
Cable depth	1 m
Rated line to line voltage	11 kV
Conductor outer radius	0.0047 m
Conductor material: copper	$\rho_{cu} = 172.4\ \mu\Omega\cdot\mathrm{m}$
1st insulating layer thickness	0.0034 m
1st insulating layer material: XLPE	$\epsilon_1 = 2.5$
Sheath thickness	0.0019 m
Sheath material: copper	$\rho_{cu} = 172.4\ \mu\Omega\cdot\mathrm{m}$
2nd insulating layer thickness	0.0018 m
2nd insulating layer material: PVC	$\epsilon_2 = 8$

Table 4.2: Test cases data

Parameters	**Value**
Header equivalent resistance	$R_{tf} = 1\ \Omega$
Header equivalent inductance	$L_{tf} = 0.1\ H$
Cable 1-2 length	5.0 km
Cable 2-3 length	6.0 km
Cable 2-4 length	2.0 km
Cable 5-6 length	3.0 km
Cable 6-7 length	2.0 km
Cable 1-8 length	20.0 km
Cable 1-9 length	2.0 km
Cable 10-11 length	5.0 km
Transformer 4-5 rated power	0.2 MVA
Transformer 4-5 leakage reactances	$X_1 = X_2 = 0.1\ pu$
Transformer 4-5 leakage resistances	$R_1 = R_2 = 0.05\ pu$
Transformer 4-5 magnetizing reactance	$X_m = 500\ pu$
Transformer 4-5 magnetizing resistance	$R_m = 500\ pu$
Transformer 9-10 rated power	0.1 MVA
Transformer 9-10 leakage reactances	$X_1 = X_2 = 0.1\ pu$
Transformer 9-10 leakage resistances	$R_1 = R_2 = 0.05\ pu$
Transformer 9-10 magnetizing reactance	$X_m = 500\ pu$
Transformer 9-10 magnetizing resistance	$R_m = 500\ pu$

Table 4.3: Load Data

Load	P_0 MW	Q_0 MVAr	$V_s pu$
S_2	0.05	0.1	0.97
S_3	0.03	0.15	0.97
S_4	0.05	0.015	0.97
S_5	0.15	0.07	0.945
S_6	0.015	0.015	0.945
S_7	0.015	0.015	0.945
S_8	0.15	0.07	0.972
S_9	0.01	0.02	0.975
S_{10}	0.07	0.03	0.974
S_{11}	0.03	0.015	0.973

in the analysis. The dominant intermediate frequencies are tracked by identifying the peak values of the frequency responses' magnitude, in a range of frequencies below the critical fitting frequencies f_c computed in the offline characterization of the cable system. An example of the process' outcome is shown in Figure 4.7 for voltage measurements performed in busbars 2, 3 and 4 during fault scenario 1.

The results of the fault location estimations are shown from Figures 4.8 to 4.10 respectively. In all cases the faulted section is identified with either the existence of a single solution or a cluster of solutions around the real fault location value. In addition, the average of the fault location estimates $\tilde{k}_i$ is shown with a solid black line.

As it is possible to see from Figures 4.8 to 4.10, the final fault location estimation using the average of the found solutions is very close to the actual values. More specifically, in the fault scenario 1 where the fault occurs at 30% of cable 23, the estimated fault location is 30.24%, which translates in a final error of 0.8% or 48 m. In fault scenario 2, the final estimation is 79.86%, which translates in a final error of 0.18% or 8.75 m. Finally, for the fault scenario 3, the final estimation is 50.44%, which translates in a final error of 0.88% or 26.4 m. In fault scenario 2, three outsider solutions are also identified, marked by circles in Figure 4.9, and discarded since they don't belong to any cluster of solutions.

To test the validity of the proposed methodology in longer cable/line sections, two additional fault scenarios are performed in cable 1-8 with a length of 20 km:

- Scenario 4: three-phase fault with $R_f = 0.2\ \Omega$ at 25% of cable 1-8
- Scenario 5: three-phase fault with $R_f = 0.2\ \Omega$ at 50% of cable 1-8

The fault location results for fault scenarios 4 and 5 are shown in Figures 4.12 and 4.13 respectively, where the fault estimation is performed considering the polynomial equations of bus 1. When performing the proposed methodology to faults occurring in cable 1-8, the methodology can provide accurate results. More specifically, by using the frequencies measured at bus 1, the methodology is able to correctly identify the first fault at 24.17% of the cable with a precision of 3.3% or 166 m. The second fault is estimated to occur at 48.77%, equivalent to a 2.46% error or 246 m.

Finally, a single phase to ground fault with a fault inception angle of zero is simulated in cable 23. The frequency spectrum of the phase voltages at Bus 3 are shown in Figure 4.11, for different fault locations. For the proposed offline methodology to emulate unbalanced faults and apply the fault location methodology, the current LTI impedance modelling defined in equations (3.20) and (3.19) needs to be extended from the modal to the phase domain. That being said, from Figure 4.11 it is possible to see that there are intermediate frequencies that depend on the fault location present in the faulted phase C, more specifically the one with values 3,875, 5,737 and 8,880 Hz. This intermediate frequency could be used to solve the fault location using the proposed fault location methodology considering the extended phase domain impedance modelling of cable/lines, which remains an open research challenge for future works. This again reinforces the need for further research on the impedance modelling of cables/lines to complement EMTP time-domain simulations with frequency-domain analysis.

The results obtained for a realistic distribution test system using the proposed fault location methodology are promising. In order to have a definitive fault location methodology, two key aspects remain unsolved:

- To extend the modal LTI impedance/admittance representation of cable/line sections from the modal to the phase domain.

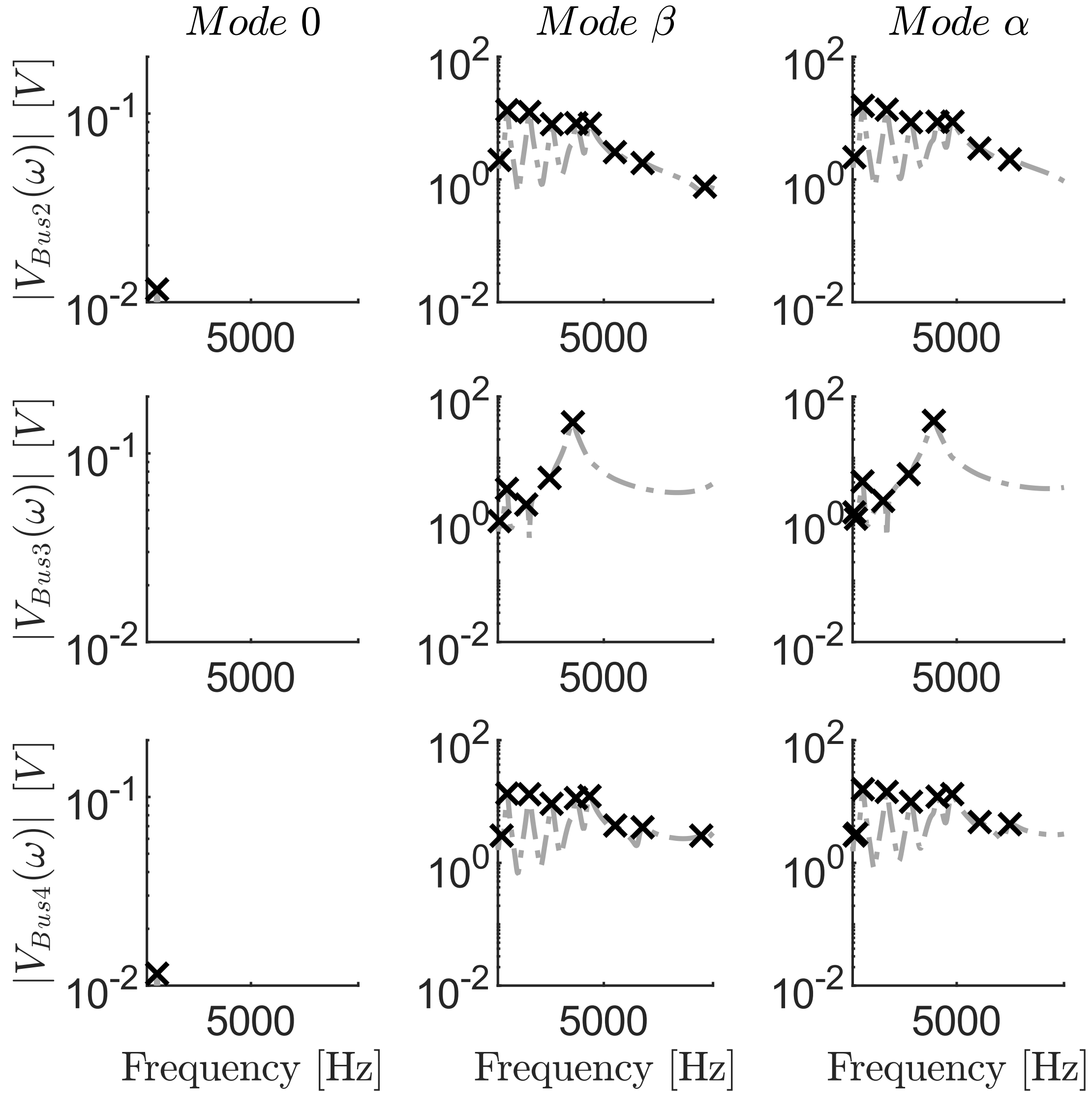

Figure 4.7: Frequency spectrum of voltages' transient response during fault scenario 1.

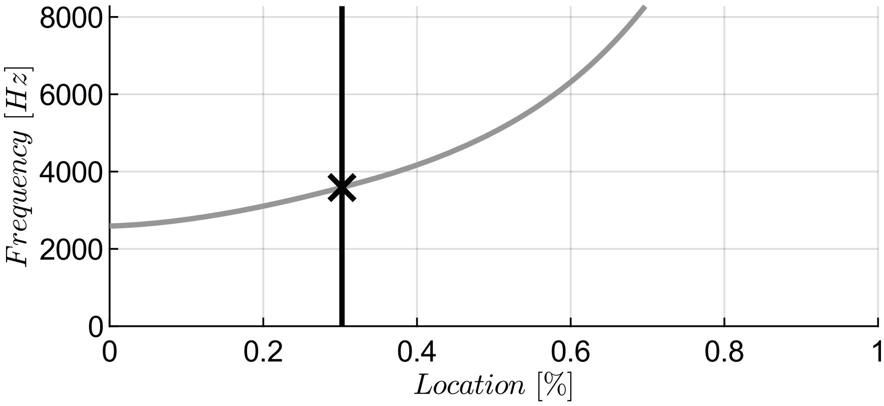

Figure 4.8: Fault location solution for fault scenario 1 using Bus 3 polynomial regressions.

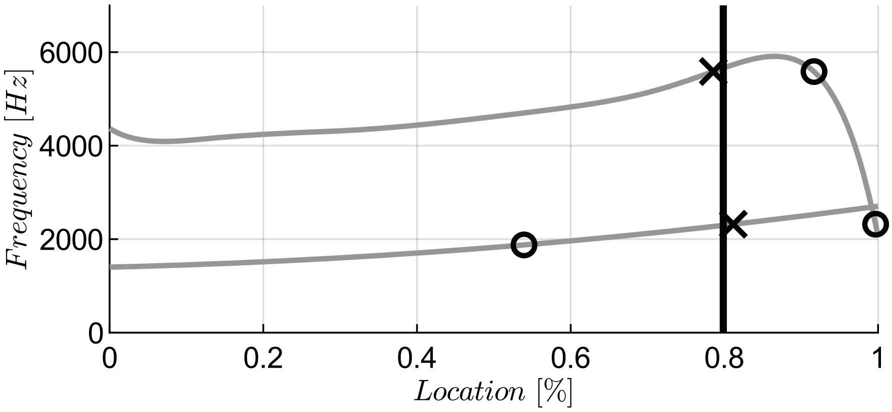

Figure 4.9: Fault location solution for fault scenario 2 using Bus 2 polynomial regressions.

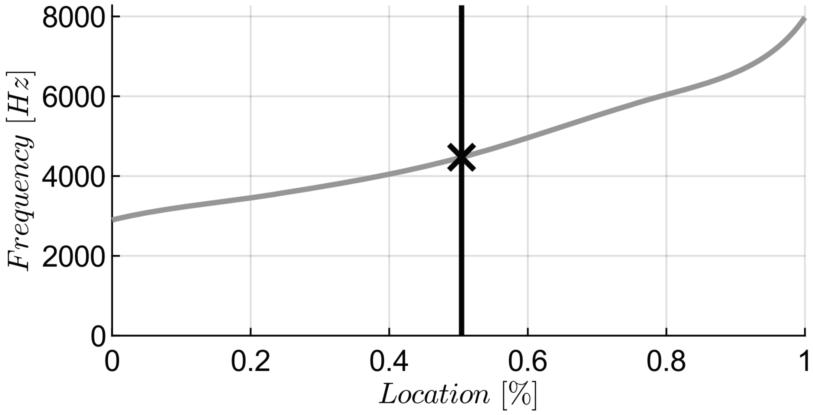

Figure 4.10: Fault location solution for fault scenario 3 using Bus 6 polynomial regressions.

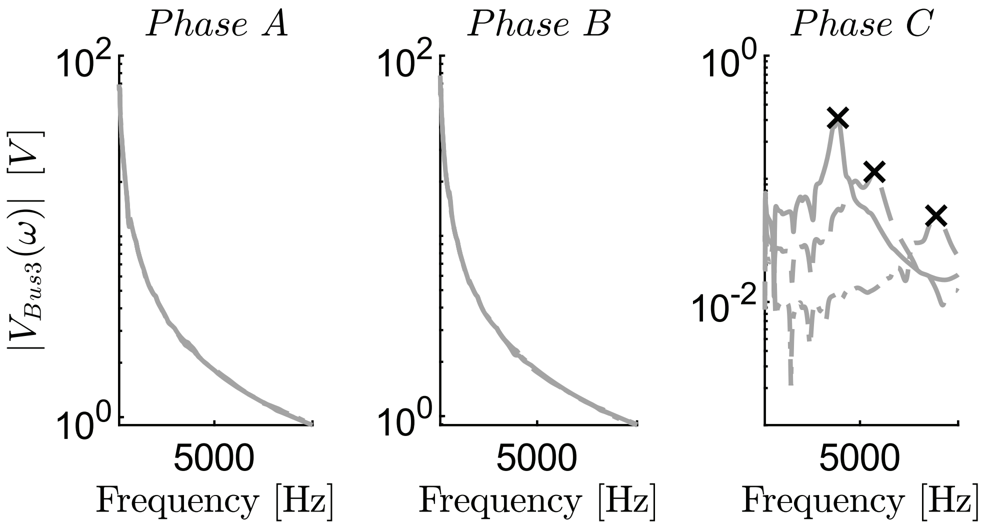

Figure 4.11: Frequency spectrum of voltages' transient response for a fault inception angle of zero in cable 23. The solid line if for a fault at 30%, the dashed line for 50% and the dotted line for 70%.

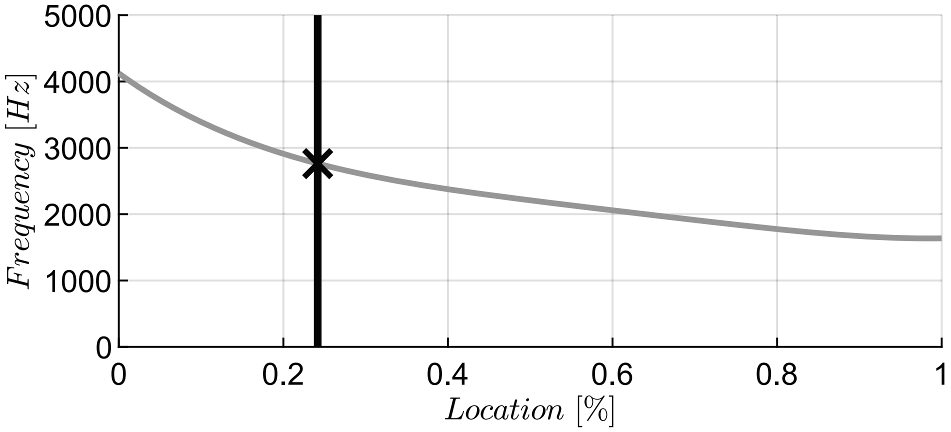

Figure 4.12: Fault location solution for fault scenario 4 using Bus 1 polynomial regressions.

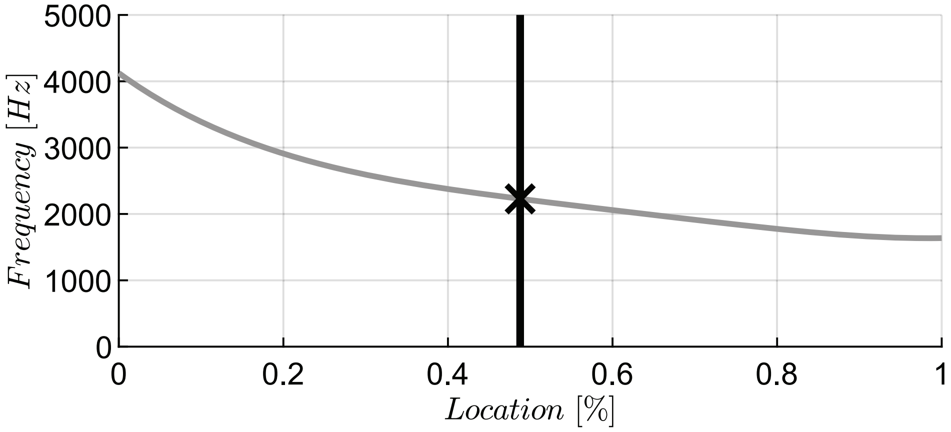

Figure 4.13: Fault location solution for fault scenario 5 using Bus 1 polynomial regressions.

- To incorporate the behaviour of converter-based devices to the network, since they can have a dynamic response in the same frequency range of interest as the proposed fault location methodology. This becomes more important as converter-based devices can remain connected to the grid during fault events according to FRT requirements from TSOs and DSOs.

The next chapter aims to tackle the modelling of converter-based devices such that they can be incorporated to the proposed fault location methodology. To achieve this, the dynamics of converter-based devices need to be represented using an LTI approach so that they can be added to the modelling process of the network in the offline characterization stage. The most common alternative being currently developed in the literature is to define an impedance representation of converter-based devices, which in turn could be incorporated in the LTI model of the network for the offline characterization stage. A new approach to the black-box impedance modelling of converter-based devices is developed and presented in the next chapter.

CHAPTER 5

Black-Box Converter Impedance Modelling

As mentioned in the previous chapter, an LTI model of converter-based devices is necessary if the proposed fault location methodology is to be used in modern power system, with high penetration of renewable generation and FACT devices. Indeed, converter-based devices can have a dynamic response in the same frequency range as the one used by the proposed fault location methodology. It is thus important to identify such frequencies and discard them from the ones originated by the transient response of cable/line sections in the system, so that they do not interfere with the fault location process. An LTI representation of converter-based devices would thus allow to incorporate their behaviour in the offline characterization process if the proposed fault location methodology, and account for their response during in the transient signals generated immediately after the occurrence of a fault event.

In what follows, an impedance/admittance model of black-box converters is proposed based on a similar approach to the one presented in Chapter 3 for the modelling of cable/line sections using rational approximations and the vector fitting algorithm. This admittance representation will be used for understanding the behaviour and interactions between the grid and converter-based devices. Since protection schemes, Fault Ride Trough capability and reactive power support are all defined by converters' control schemes, they will impact the transient behaviour of the system and thus need to be accounted for in the proposed fault location methodology. In other words, control, protection and stability become inseparables when high penetration of converter-based devices are present in the network.

5.1 Introduction

In the last decade, converter-based devices have continually increased their participation in power systems, both in the form of converter interfaced generation (CIGs) and FACT devices [80]. By simultaneously displacing conventional generation and incorporating more sophisticated control schemes however, converter-based devices can pose new risks to the stable operation of power systems. More specifically, it has been noted that these technologies can lead to system oscillations followed by unstable operation in a wide range of frequencies, from slow subsynchronous phenomena to fast control interactions of a few kHz [81, 82]. In order to investigate and analyse this unstable behaviour, impedance-based modelling of converter-based devices has gained increased attention in recent years [83–91].

From the design perspective, impedance-based modelling together with the generalized Nyquist criterion provide a fast method to test new control strategies and different operating conditions. It also helps to gain insight of the impact that different control loops have in the converter's dynamic response and stability. In [83], the authors use impedance modelling to assess the impact of the PLL, inner current control and outer power control loops in a VSC converter. A similar analysis is performed in [84], where the impact of the PLL and inner current control loops on the stability of a VSC is assessed. In addition, the authors demonstrate the frequency coupling effect in the *dq* domain introduced by the PLL scheme. Impedance-based modelling has also been used to assess the risk of control interaction and unstable operation for several converters connected to small tests grids [85–87].

In general, the impedance-based behaviour of a converter-based device can be obtained in two ways. From a theoretical perspective, the control and electrical equations defining the dynamics of the converter can be linearized around its operating condition. To do this, it is necessary to have full knowledge of both the control and hardware structure of the converter, together with its parameters and operating conditions [83–88]. From an experimental perspective, several techniques have been proposed to measure the impedance behaviour of power converters: using frequency sweep methodologies [89, 90, 92], estimate it from its transient response [93] and using MIMO parametric identification procedure [94] among others. In these cases, it is not necessary to have full knowledge of the converter structure and control schemes. Impedance measurements are thus a valuable tool to model the dynamic behaviour of so called "Black-box" models, where the inner structure and control schemes are unknown and inaccessible.

While impedance-based models have proven useful to design and test the dynamic behaviour of converters in small test systems, it remains impractical for the stability assessment of larger power networks. This is because using the generalized Nyquist criterion or several Bode plots in larger systems to visually assess stability becomes impractical. In addition, such methods don't provide insight or the root cause of possible unstable operating conditions to power engineers and transmission system operators (TSOs), so that corrective actions can be taken. State-space models on the other hand are widely used in stability assessment studies, since they provide useful information on the cause of possible unstable operation via participation factors and eigenvalue analysis [89, 91]. The main problem of this approach is that a full knowledge of the system's dynamic equations is necessary, and so it remains impractical when left with black-box model of power converters [89, 91] for business confidential reason.

Some works have tried to fill the gap between impedance-based models and state-space approaches using system identification techniques. Recent works on this topic use harmonic state-space methods to model of power electronic devices [95, 96]. Other works have focused on translating directly the impedance measurements to state-space models using model identification procedure such as the vector fitting algorithm [89, 90, 97]. In [90], the authors apply the vector fitting technique to the frequency response data of a VSC average model including a PLL, an inner current control loop and a constant DC voltage. The authors show that this approach can be use to correctly identify the eigenvalues that define the dynamic behaviour of the VSC model. In [97], the authors propose a non-parametric impedance identification procedure to assess stability and provide corrective control actions for an offshore windfarm/HVDC connection to an AC grid. While in both cases the potential of system identification techniques together with impedance modelling are showcased, an extension for stability assessment of larger grids including more complex converter models is necessary. Additionally, it has been proved that the vector fitting algorithm converges if the order of the model is chosen equal to or higher than the order of the underlying system [98], which for black-box models it is unknown. The work developed in this Chapter aims to fill the gap between impedance-based modelling and state-space stability assessment procedures for power systems. The specific contributions of this work are:

1. Provide a complete methodology to establish a state-space model for black-box converter-based models, on the basis of vector fitting techniques and frequency response data.
2. Specify how to use the vector fitting algorithm with impedance/admittance data for

obtaining accurate state-space models for black-box converter in the *dq* domain.

3. Provide a methodology to incorporate such models in an LTI state-space model representation in the *dq* domain to perform stability assessment studies.

4. Validate the proposed methodology considering both average and detailed switching models of converter-based devices.

5. Test the proposed methodology in the well established 39 bus New England system, considering realistic converter-based device models.

5.2 Impedance measurement and modelling

In this section, the impedance measurement and LTI representation of black-box converter-based models is presented. Firstly, the frequency response measurement of a single converter device is presented. This is done by using a frequency sweep approach as presented in [89, 90], which is summarized in Section 5.2.1. Secondly, a methodology to translate the frequency response data into a state-space representation for stability assessment studies is presented.

5.2.1 Frequency response measurement

To measure the frequency response of a black-box converter device using a frequency sweep approach, two conditions must be fulfilled. First, the converter-based device must be operating in steady-state behaviour. This is accomplished by connecting the converter device to an equivalent grid as shown in Figure 5.1, which provides the operating conditions of the converter at the point of common coupling (PCC) as in the original AC grid. The operating conditions are defined by the grid strength at the PCC, which in this case is captured by the Thévenin equivalent impedance Z_{th} of the grid seen at the PCC, together with voltage magnitude V_0 and phase angle δ_0 provided by the infinite bus at the fundamental frequency f_0. The second condition is to provide a small-perturbation signal V_i of varying frequency f_i to measure the frequency response of the converter. In general, this can be accomplished either by connecting

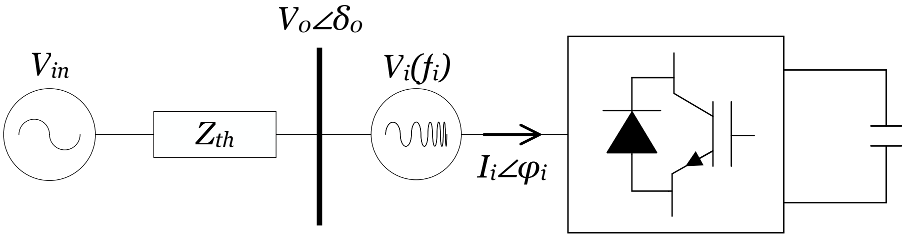

Figure 5.1: Frequency sweep measurement for converter-based devices.

a shunt current source or a series voltage source at the interface between the converter and the equivalent grid [90]. Since in general the grid's strength is much larger than the converter's rated power, most of the injected current will flow through the grid's impedance Z_{th} rather than through the converter. For this reason, in this work a series voltage injection V_i is considered for improved measurement accuracy.

Once the previous two conditions have been met, a frequency sweep measurement of the converter's impedance response can be performed. In the case of a single tone frequency sweep, this is achieved by varying the injected voltage signal's frequency f_i and measuring the converter's current's magnitude I_i and phase angle ψ_i at that corresponding frequency f_i. The impedance response of the converter at that specific frequency f_i can then be calculated according to equation (5.1) [90]. It is worth noting that equation (5.1) is defined in the *dq* domain. While the frequency sweep approach could be performed in any reference frame, the *dq* one is chosen in this work since it is easier to accurately track the small signals magnitudes V_i and I_i with their respective phase angles using FFT techniques, without the fundamental frequency signal interfering in the measurement since it becomes a DC value. To perform the *dq* transform without using a PLL in the measurement device, which would add undesired dynamics, the fundamental frequency phase angle δ_0 at the PCC can be computed beforehand using load-flow calculations. It is also important to note that, since there are 4 independent unknown variables $Z_{i,dd}$, $Z_{i,dq}$, $Z_{i,qd}$ and $Z_{i,qq}$, it is necessary to perform two measurements tests as explained in [90]. These measurements tests must be performed with linearly independent injected signals $\boldsymbol{V_{i1}}$ and $\boldsymbol{V_{i2}}$. Without loss of generality, it is possible to use pure D and a pure Q axis injections for each test respectively as defined in equations (5.2) and (5.3).

$$\begin{bmatrix} Z_{i,dd} & Z_{i,dq} \\ Z_{i,qd} & Z_{i,qq} \end{bmatrix} = \begin{bmatrix} V_{i1,d} & V_{i2,d} \\ V_{i1,q} & V_{i2,q} \end{bmatrix} \begin{bmatrix} I_{i1,d} & I_{i2,d} \\ I_{i1,q} & I_{i2,q} \end{bmatrix}^{-1} \tag{5.1}$$

$$\boldsymbol{V_{i1}} = \begin{bmatrix} V_{i1} \cdot cos\left(\omega_i t\right) \\ V_{i1} \cdot cos\left(\omega_i t - \frac{2\pi}{3}\right) \\ V_{i1} \cdot cos\left(\omega_i t + \frac{2\pi}{3}\right) \end{bmatrix} \tag{5.2}$$

$$\boldsymbol{V_{i2}} = \begin{bmatrix} V_{i2} \cdot sin\left(\omega_i t\right) \\ V_{i2} \cdot sin\left(\omega_i t - \frac{2\pi}{3}\right) \\ V_{i2} \cdot sin\left(\omega_i t + \frac{2\pi}{3}\right) \end{bmatrix} \tag{5.3}$$

5.2.2 Impedance/admittance LTI modelling

As discussed in [90], once the impedance measurements have been performed for a converter-based device, an LTI approximation of the apparent impedance of the system formed by the converter-based device and the grid's equivalent Thévenin impedance can be obtained applying the vector fitting algorithm [60–62] to assess possible instabilities. While this approach is useful for design purposes in a single converter, it remains impractical to assess instabilities in a larger grid with several converter-based devices. For power system's stability assessment, it is instead necessary to have a LTI representation of the converter-based device on its own. With such LTI representation in the *dq* domain, the converter dynamics could be incorporated in the state-space representation of the rest of the grid to perform standard eigenvalue and participation factor analysis. While this is possible, additional considerations must be taken care of when performing the vector fitting of the converter dynamics.

The vector fitting algorithm allows to obtain an LTI approximation $\hat{H}(s)$ for the set of frequency response measurements $\mathcal{F} = \left\{H(f_1), \ldots, H(f_{N_f})\right\}$. The approximation $\hat{H}(s)$ is a sum of rational functions as defined in equation (5.4), where a_i and b_i correspond to real residues and poles, while r_i and p_i are imaginary residues and poles respectively and D is a real constant.

The outputs of the vector fitting algorithm are the residues and poles a_i, r_i, b_i and p_i together with D and the root mean square error ϵ_{rms} in relation to the input measurement set $\mathcal{F}$. The inputs to the vector fitting algorithm are [90]:

1. The set of frequency response measurements $\mathcal{F}$.
2. The desired order of the approximation defined as N.

The previous input arguments should be selected such that the RMS error ϵ_{rms} is minimized given a reasonable order of approximation N. In the next sections, a detailed overview is given on how these inputs should be selected.

$$\hat{H}(s) = D + \sum_{i=1}^{M} \left(\frac{a_i}{s - b_i} \right) + \sum_{i=M+1}^{N} \left(\frac{r_i}{s - p_i} + \frac{\bar{r}_i}{s - \bar{p}_i} \right) \tag{5.4}$$

Input frequency response measurements

In most of the literature the impedance behaviour of converter-based devices is selected to perform stability analysis. The general approach is to linearize the known control functions in the Laplace domain as to obtain the impedance equivalent of the converter dynamics. This however is limited not only by the fact that most times the inner control structure is unknown, but also because it is not always possible to properly linearize all control schemes. Examples of such cases are limiters imposed in different state variables, delays in the system or when more recent and sophisticated control approaches are used, such as sorting algorithms for the capacitor balancing control or model predictive control schemes. Indeed, the impedance beavhiour of converter-based device might not be the best choice to perform the LTI modelling of the converter dynamics. In a more general sense this can be understood if we assume that the control functions can be approximated by sums of rational functions $\hat{H}(s)$ in the Laplace domain $\hat{H}(s)$. These functions could then be measured using standard frequency sweep techniques, and then mathematically defined using the vector fitting algorithm into its rational polynomial form $P(s)/Q(s)$, where $P(s)$ and $Q(s)$ are polynomial functions of s with coefficients $\{a_1, \ldots, a_N\}$

and $\{b_1, \ldots, b_N\}$ respectively. With this representation, the impedance behaviour is represented by a rational matrix as shown in equation (5.5), where the argument (s) of each function has been omitted for clarity. This in turn means that, if the impedance behaviour $\mathbf{Z}_{dq}$ of the converter dynamics can be approximated by a sum of rational function of order N, then its admittance behaviour $\mathbf{Y}_{dq}$ defined by equation (5.6) will require an approximation of $4N$ if no zeros/poles cancellations occur. This implication goes both ways, i.e. if the admittance can be approximated by a sum of rational functions of order N, then its impedance behaviour will require an approximation of order $4N$.

This analysis indicates that when approximating the black-box converter dynamics using the vector fitting approach, both the impedance and admittance behaviours should be considered. Since no information is known from the internal dynamics of the device, it is not possible to know *a priori* which of the two representations will require the lowest order to approximate. In fact, it is possible that, while one representation can be accurately approximated using a sum of rational functions, its counterpart might be intrinsically not well-behaved to be fitted. A simple example of such case is when considering an RL circuit in the dq domain, where its impedance defined by equation (5.7) is not well-behaved for the purpose of rational fitting since it is improper, i.e. the order N_p of its numerator $P(s)$ is higher than the order N_q of its denominator $Q(s)$. Traditional vector fitting is able to approximate improper functions up to a second order difference, i.e. $N_p = N_q + 2$, by finding constants D and E. In the case of (5.7) however, the fitting process will add fictitious poles no matter the desired approximation order N defined by the user, introducing false dynamics and generating an inaccurate fitting of the original impedances. The admittance behaviour defined by (5.8) is proper and thus well-behaved for the purpose of vector fitting. The converter dynamics should thus be represented by the LTI model that has the lowest error for the desired fitting order N. As will be described in Section 5.3, both the impedance and admittance LTI representations of the converter dynamics can be used for system-wise stability assessment studies.

$$\mathbf{Z}_{dq} = \begin{bmatrix} \frac{P_{dd}}{Q_{dd}} & \frac{P_{dq}}{Q_{dq}} \\ \frac{P_{qd}}{Q_{qd}} & \frac{P_{qq}}{Q_{qq}} \end{bmatrix} \tag{5.5}$$

$$\Leftrightarrow \mathbf{Y}_{dq} = \frac{1}{K} \begin{bmatrix} P_{qq}Q_{dd}Q_{dq}Q_{qd} & -P_{dq}Q_{dd}Q_{qq}Q_{qd} \\ -P_{qd}Q_{dd}Q_{qq}Q_{dq} & P_{dd}Q_{qq}Q_{dq}Q_{qd} \end{bmatrix} \tag{5.6}$$

$$\text{Where } K = \frac{1}{P_{dd}P_{qq}Q_{dq}Q_{qd} - P_{dq}P_{qd}Q_{dd}Q_{qq}}$$

$$\mathbf{Z}_{RL} = \begin{bmatrix} R+sL & -\omega_0 L \\ \omega_0 L & R+sL \end{bmatrix} \tag{5.7}$$

$$\mathbf{Y}_{RL} = \frac{1}{(R+sL)^2 + (\omega_0 L)^2} \begin{bmatrix} R+sL & \omega_0 L \\ -\omega_0 L & R+sL \end{bmatrix} \tag{5.8}$$

Another important aspect to consider in the vector fitting process is the dependence that the frequency response input data in the dq domain has on the angle δ_i for each i^{th} converter used for their synchronization via PLL. While frequency decoupled models, such as an RL branch, will have dq representations which are dq invariant, frequency-coupled models such as converter-based devices must be computed on a common dq reference frame [90, 99]. This can be achieved by using a linear transformation $\mathbf{T}_{dq,i}$ on the converter's measured impedance $\mathbf{Z}_i$ frequency response data by considering a common reference angle δ_{ref} and its synchronizing angle δ_i which can be computed from load flow calculations or by performing the FFT on the voltage signal of phase a when performing the frequency sweep measurements to obtain the impedance/admittance behaviour of the converter [90], to obtain the impedance frequency response $\tilde{\mathbf{Z}}_i(s)$ in the common reference frame as defined in equation (5.9). An analogous process can be performed for the measured admittance response.

$$\begin{aligned} \tilde{\mathbf{Z}}_i(s) &= \mathbf{T}_{dq,i}\mathbf{Z}_i(s)\mathbf{T}_{dq,i}^{-1} \\ \mathbf{T}_{dq,i} &= \begin{bmatrix} cos(\delta_i - \delta_{ref}) & -sin(\delta_i - \delta_{ref}) \\ sin(\delta_i - \delta_{ref}) & cos(\delta_i - \delta_{ref}) \end{bmatrix} \end{aligned} \tag{5.9}$$

When each *dq* impedance component is vector fitted independently, each element of the matrix $\mathbf{Z}_{dq}$ will have its own set of poles and residues as shown in eq (5.5). By combining equations (5.5) and (5.9), it is possible to see that, for a rational representation in a given *dq* reference frame $\mathbf{Z_{dq}}$, when translating it to another reference frame $\tilde{\mathbf{Z}}_{\mathbf{dq}}$ the order N and dynamics of the new rational representation will change. More specifically, each element of the new matrix $\tilde{\mathbf{Z}}_{\mathbf{dq}}$ will be a linear combination of the rational representations of $\mathbf{Z_{dq}}$, with scaling factors depending on the phase angle difference between the two *dq* reference frames being considered. This reference frame angle dependence can be avoided by identifying the common poles of all 4 components using the vector fitting process in the sum of them as defined in equation (5.10). Indeed, by performing the vector fitting algorithm to Z_{DQ} to obtain its rational approximation $\hat{Z}_{DQ}$, a common set of poles $\{\lambda_1, \ldots, \lambda_N\}$ defined by the denominator Q_Z can be derived for the impedance behaviour $\mathbf{Z_{dq}}$. Once the poles are identified, the residues of each element can be computed by performing the vector fitting on each element's frequency response data considering the poles previously computed, which will provide the polynomial functions P_{DD}, P_{DQ}, P_{QD} and P_{QQ}. This in turn provides a rational representation as shown in equation (5.12), which can be rotated from one *dq* reference to another using equation (5.9) without changing the order N of the approximation and the common set of poles $\{\lambda_1, \ldots, \lambda_N\}$, only the residue of its elements. It is thus concluded that the impedance and admittance elements in the *dq* domain should not be fitted independently if the *dq* reference frame rotation dependence of its LTI representation is to be minimized. This analysis is valid for both the impedance and admittance representations of the converter dynamics.

$$Z_{DQ}(s) = Z_{dd} + Z_{dq} + Z_{qd} + Z_{qq} \tag{5.10}$$

$$\hat{Z}_{DQ}(s) \approx \frac{1}{Q_Z}\left(P_{DD} + P_{DQ} + P_{QD} + P_{QQ}\right) \tag{5.11}$$

$$\mathbf{Z}_{dq} = \frac{1}{Q_Z}\begin{bmatrix} P_{DD} & P_{DQ} \\ P_{QD} & P_{QQ} \end{bmatrix} \tag{5.12}$$

Approximation order selection

When selecting the approximation order N, in general the higher it is, the lower the RMS error ϵ_{rms} will be. However, it is not possible to select an arbitrarily large value of N. In this case, the order of the converter's impedance (or admittance) fitted approximation $Z_c(s)$, is constrained by the requirement of having a stable representation of the original measuring system as shown in Figure 5.2. While the vector fitting algorithm can be set to always provide stable LTI representations, i.e. $b_i < 0 \; \forall i \in \{1, \ldots, M\}$ and $\Re(p_i) < 0 \; \forall i \in \{1 + M, \ldots, N\}$, the fitted approximation of the converter dynamics must fulfill that the complete measuring system is also stable. The dynamics of the complete measuring system are defined by equation (5.13). This in turn means that the approximation order N must be increased to reduce the RMS error ϵ_{rms} while providing stable representations of the original measuring system, i.e. the poles of $H(s)$ should be on the left half of the complex plane. The best LTI representation will thus be the one with the lowest RMS error while preserving the stable behaviour of the original measuring system. The fitting methodology is summarized in Figure 5.3 for the admittance case, where it is shown how the fitting order should be increased until finding the first unstable model that signals the stopping criterion so that only the previous stable representation with the lowest RMS error is considered. The same process applies for the impedance behaviour of the converter. Large approximation orders will lead to over-fitting, which when evaluated in the original test system may lead to a false unstable representation.

$$\begin{aligned} V_{pcc}(s) &= H(s)\left[Y_{th}(s)V_{in}(s) + Y_c(s)V_c(s)\right] \\ H(s) &= \left(Y_c(s) + Y_{th}(s)\right)^{-1} \end{aligned} \tag{5.13}$$

With the previous considerations, it is thus possible to obtain an LTI representation of the converter dynamics in the *dq* domain, based either in the converter's impedance or admittance frequency response. In the next section, a detailed description is provided on how to integrate this LTI representation for power system stability assessment studies.

5.3 Impedance-based stability assessment

In this section, a detailed description on how to use the LTI impedance/admittance representation of black-box converter models in stability assessment studies is provided. To this end, it is necessary to provide a framework that allows computing the state-space LTI representation of a power system in the *dq* domain, including the converter's LTI models, to perform standard eigenvalue analysis of the system dynamics.

Once the converter's LTI model has been computed according to the methodology presented in Section 5.2, its state-space representation can be computed. It is important to note that for the residue/pole representation obtained from the vector fitting algorithm, there are infinitely many possible state-space representations, most of which might not have any meaningful physical interpretation. However, it is possible to compute a circuit realization of both the impedance and admittance LTI models using *RLC* branches, analogous to the one performed for the cable/line section case described in Section 3.3.2. Using Kirchhoff's laws on the circuit realizations in Figure 3.6, a state-space representation for the converter's impedance/admittance LTI model can be computed. For the case of the admittance representation, the aggregated state-space

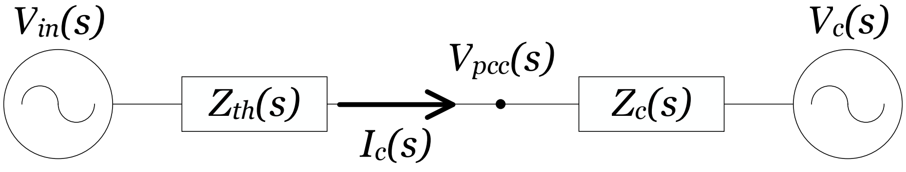

Figure 5.2: Impedance representation of the measurement system.

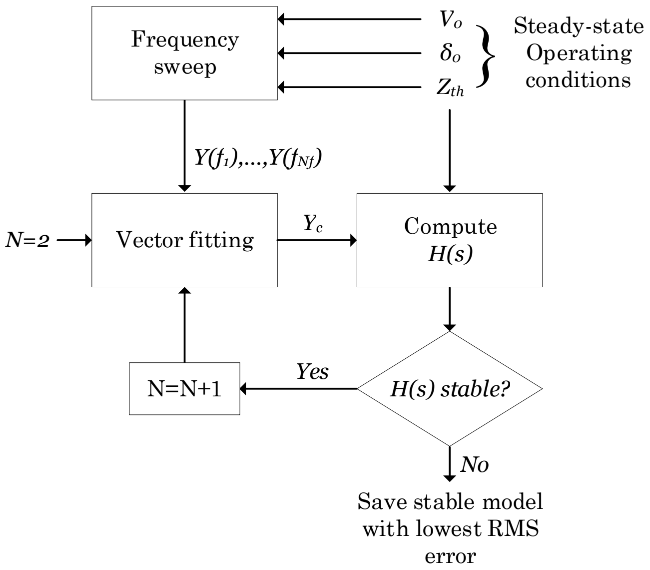

Figure 5.3: Fitting methodology for the admittance frequency measurements.

form of the 4 LTI models $Y_{dd}(s)$, $Y_{dq}(s)$, $Y_{qd}(s)$ and $Y_{qq}(s)$ is presented in equation (5.14). A similar procedure can be performed for the impedance representation, where the inputs are the currents $[I_{km,d}\ I_{km,q}]^t$ and the outputs are the voltage drops $[\Delta V_d\ \Delta V_q]^t$.

$$
\begin{aligned}
s\begin{bmatrix} X_{dd} \\ X_{dq} \\ X_{qd} \\ X_{qq} \end{bmatrix} &= \begin{bmatrix} A_{dd} & & & \\ & A_{dq} & & \\ & & A_{qd} & \\ & & & A_{qq} \end{bmatrix} \begin{bmatrix} X_{dd} \\ X_{dq} \\ X_{qd} \\ X_{qq} \end{bmatrix} + \begin{bmatrix} B_{dd} & \\ & B_{dq} \\ B_{qd} & \\ & B_{qq} \end{bmatrix} \begin{bmatrix} \Delta V_d \\ \Delta V_q \end{bmatrix} \\
\begin{bmatrix} I_{km,d} \\ I_{km,q} \end{bmatrix} &= \begin{bmatrix} C_{dd} & C_{dq} & & \\ & & C_{qd} & C_{qq} \end{bmatrix} \begin{bmatrix} X_{dd} \\ X_{dq} \\ X_{qd} \\ X_{qq} \end{bmatrix} + \begin{bmatrix} D_{dd} & D_{dq} \\ D_{qd} & D_{qq} \end{bmatrix} \begin{bmatrix} \Delta V_d \\ \Delta V_q \end{bmatrix}
\end{aligned}
\tag{5.14}
$$

Once all state-space models have been computed for all converter-based devices of interest, they can be further aggregated to compute the state-space form of the entire grid in the dq frame. This can be done by first establishing one state-space representation for all branch element connections between busbars, and another state-space model for all shunt element connections from each busbar to ground.

For shunt connections to ground, the input signals are the currents $I_{b,dq}$ flowing from the grid to ground, while the output signals corresponds to the busbar's voltages V_{dq}. This state-space model accounts, for example, for the loads in the system and transmission lines' capacitances/conductances. The state-space representation is presented in equation (5.15).

For series elements connecting busbars/voltage sources, such as the converter's admittances, the series branches of transmission lines and transformers, they can be represented in a separate state-space model. In this case, the input signals are the voltage drops ΔV_{dq} between the connected busbars, including the input voltages to the gird $V_{in,dq}$ set by voltage sources such as synchronous machines or VSC converters. The output signals correspond to the flowing currents $I_{km,dq}$ on each series branch of the system. The state-space representation is presented in equation (5.16).

$$\begin{cases} sX_V = A_V X_V + B_V I_{b,dq} \\ V_{dq} = C_V X_V + D_V I_{b,dq} \end{cases} \tag{5.15}$$

$$\begin{cases} sX_I = A_I X_I + B_I \Delta V_{dq} \\ I_{km,dq} = C_I X_I + D_I \Delta V_{dq} \end{cases} \tag{5.16}$$

By combining equations (5.15) and (5.16), together with the nodal and branch balancing matrices ξ_I and ξ_V as defined in equations (5.17) and (5.18), it is possible to establish a grid state-space representation. More specifically, the dynamic state-space matrix A_{sys} defining the dynamic behaviour of the grid can be computed according to equation (5.19). Using eigenvalue analysis and participation factor computation on A_{sys}, it is possible to identify unstable operating conditions and poorly damped oscillatory modes in the system, together with the respective contributions of each converter-based device. This assessment allows to take corrective measures, by changing the operating conditions and/or the control parameters of the converter-based devices. In addition, the impedance/admittance model of converter devices allows to easily reduce and aggregate them into equivalent impedance-voltage source at the fundamental frequency when they are electrically distant of the area or devices of interest in very large power system, using standard impedance equivalence methods. In a large, realistic power system, when checking for converter interactions or poorly damped oscillations, in general, only a subset of power converters in a specific area of interest needs to be modelled in detail while the rest of the grid can be simplified. This procedure however becomes more complex as black-box models are considered in the grid, since their aggregation and reduction are not obvious and many times not possible to perform. Once the impedance modelling has been done however, this allows to reduce the original system and thus make stability assessment scalable to larger and more complex grids.

$$I_{b,dq} = \xi_I I_{km,dq} \tag{5.17}$$

$$\Delta V_{dq} = \xi_V V_{dq} + \xi_{in} V_{in,dq} \tag{5.18}$$

$$A_{sys} = \begin{bmatrix} A_V & \\ & A_I \end{bmatrix} + \begin{bmatrix} B_V\xi_I & \\ & B_I\xi_V \end{bmatrix} \begin{bmatrix} I & -D_I\xi_V \\ -D_V\xi_I & I \end{bmatrix}^{-1} \begin{bmatrix} & C_I \\ C_V & \end{bmatrix} \tag{5.19}$$

5.4 Results

To test the methodologies proposed in Sections 5.2 and 5.3, the well-known 39 Bus New England system, shown in Figure 5.4, is implemented in PSCAD. All synchronous generators except for G1 include theirs governor, steam turbine and AVR models. The system is modified by replacing G9 in Bus 29 by a 200 MVA detailed type 4 VSC aggregated windfarm model, available in [100]. Transmission lines are modelled using Π - sections, with active power loads represented by a constant current characteristic and reactive power loads with a constant impedance characteristic.

To validate the proposed impedance stability assessment methodology, it is first tested to compare the stability boundaries between the average and detailed models of a MMC STATCOM module. Then, the proposed impedance stability assessment methodology is tested in the 39 Bus New England system for two scenarios:

- Scenario 1: to assess the dynamic behaviour of the windfarm for different values of the grid strength at Bus 26

- Scenario 2: to assess the risk of control interactions when connecting a 200 MVA MMC STATCOM at Bus 28

When performing stability assessment studies in large grids, it might be impractical to model in detail the entirety of the network. Depending on the phenomena being studied, different partition and reduction techniques have been developed in the literature, such that the model complexity can be reduced without significantly affecting the accuracy of the study [101–103]. More recent works have proposed power system clustering and partitioning based on electrical distance and grid topology, useful for voltage related studies [101, 102]. While reduction techniques are out of the scope of this work, the 39 Bus system is partitioned as proposed in [102] to perform the proposed LTI stability assessment based on the state-space representation of the grid. More specifically, devices in the subsystem under study are modelled in detail using their LTI models, while the rest of the grid is aggregated into equivalent Thévenin models at the subsystem's boundary busbars.

To perform stability assessment for both scenarios, the following methodology steps are performed:

1. Obtain the impedance frequency response for windfarm/STATCOM models as per Section 5.2.1 using the frequency sweep method on detailed EMT PSCAD models.
2. Obtain the LTI representation of each converter-based device as per Section 5.2.2.
3. Perform eigenvalue analysis as per Section 5.3, using a reduced representation of the system considering subsystem 2 and an equivalent Thévenin grid of the rest of the grid as seen from busbar 26, as shown in Figure 5.5.
4. Validate stability assessment results with time-domain simulations in PSCAD in both the reduced 3 bus and full 39 bus systems.

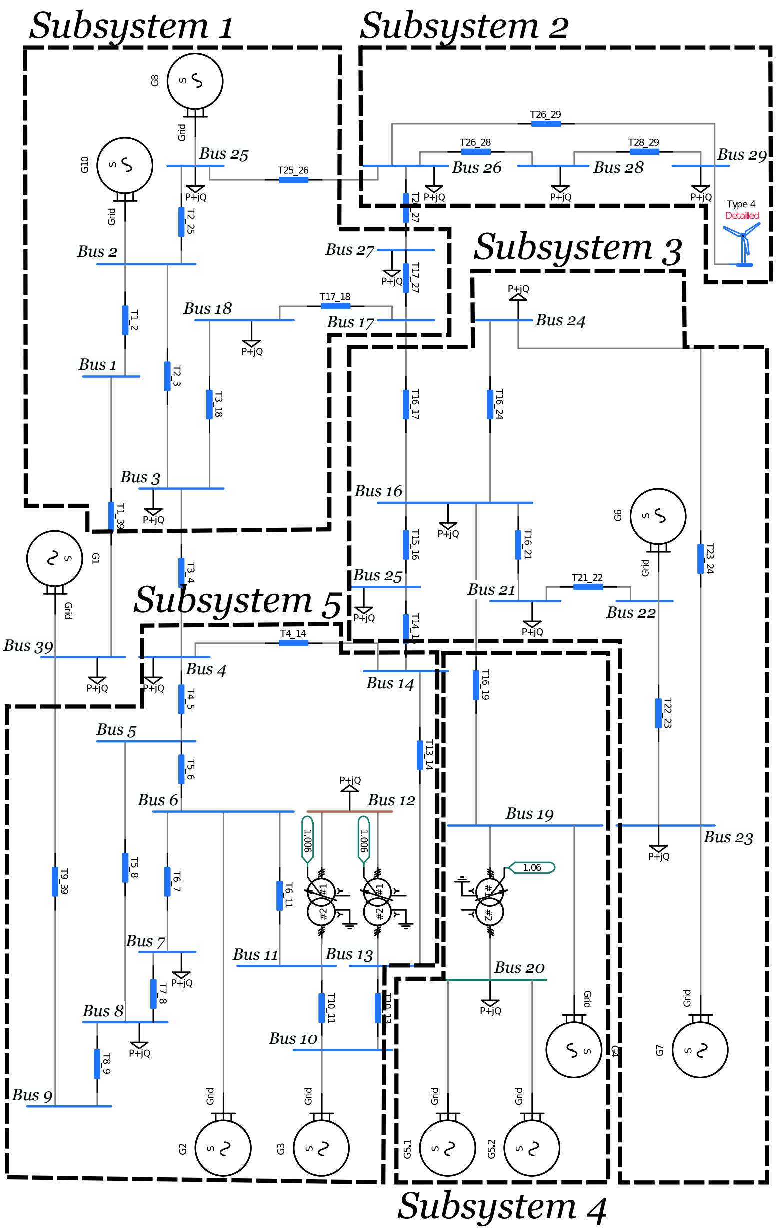

Figure 5.4: Modified 39 Bus New England system in PSCAD.

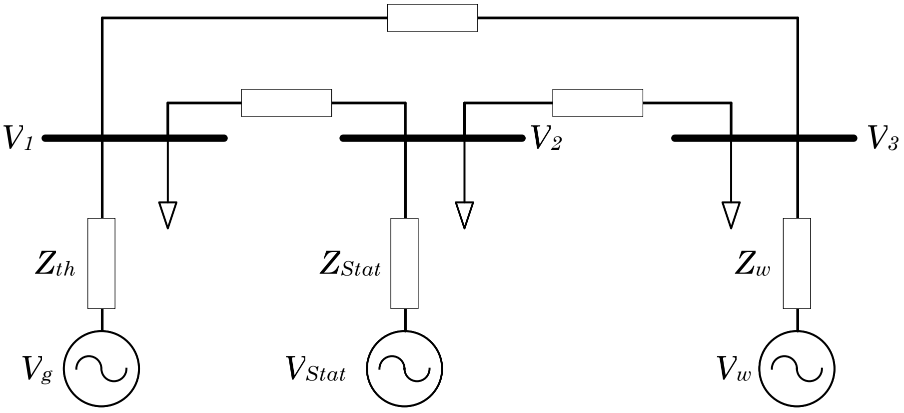

Figure 5.5: Reduced equivalent of subsystem 2 for stability assessment.

5.4.1 MMC STATCOM model comparison

In this section, the proposed impedance modelling methodology is used to compute the stability boundary of a full-bridge MMC STATCOM module of 200 MVA. A detailed model is used, based on the HVDC model available in [104], which has been modified accordingly to work as a STATCOM model. The STATCOM parameters are specified in Table 5.1. The MMC detailed model considers [105]:

- Standard *dq* PI vector control for the outer AC voltage and inner current control loops.
- PLL and PWM modulation for operating the power modules.
- Capacitor balancing is achieved by incorporating a sorting algorithm depending on the state of charge of each power module.
- A circulating current suppression control.

The proposed impedance modelling methodology is used to compare the stability boundaries between the average and detailed models of the MMC STATCOM module. The average model in this case considers:

- PLL control.
- Inner *dq* current control loop.
- Ideal constant DC voltage.

Both models are operating in AC voltage control mode, with a voltage reference of 1.0 p.u. and providing 100 MVAr. Initially, the impedance frequency response data is measured using the frequency sweep technique for both models. An LTI representation of each model is then computed in the *dq* domain as explained in Section 5.2. It is worth noting that it is possible to obtain a good approximation of the admittance response for both the average and detailed models of the MMC STATCOM, but not when considering their impedance behaviour. This

Table 5.1: MMC STATCOM parameters

Parameters	**Value**
Rated power	200 MVAr
Number of power modules	44 per arm
Power module capacitance	5 mF (17 kJ/MVA)
Arm inductance	20 mH
DC rated voltage	35.2 kV
AC rated voltage	33 kV
Carrier frequency	360 Hz

Table 5.2: RMSE for admittance and impedance fittings considering detailed and averaged MMC STATCOM models

	dd	*dq*	*qd*	*qq*
Y_{det}	5.287e-5	6.236e-5	4.713e-5	2.332e-5
Y_{avg}	3.481e-5	2.068e-5	2.216e-5	1.828e-5
Z_{det}	3.525e3	2.745e3	1.637e3	3.333e3
Z_{avg}	8.632e3	7.811e3	8.462e3	8.628e3

can be seen in Fig. 5.6 and Fig. 5.7, where the frequency response data for both MMC STATCOM models are shown, together with their respective vector fitting approximations. As it can be see from Fig. 5.6 and Fig. 5.7, while it is possible to obtain a good approximation of the admittance response with an approximation of order 6, the same cannot be said for the impedance response as opposed to the conventional approach presented in the literature. To obtain the same level of accuracy considering the impedance response, it would thus be necessary to continue increasing the fitting order. This however is limited by the fact that over fitted models will usually include numerical instabilities and thus false dynamic representations of the converter. Indeed, whether the impedance or the admittance behaviour of the converter is best suited for the vector fitting procedure will depend on the internal control structure of the converter, on its control parameters and operating condition. The RMS fitting errors for each component for both models are summarized in Table 5.2, where it is possible to see that the impedance fittings have a significantly larger error than the admittance ones. Similar results are obtained for the phase angle data. This goes in line with the theoretical description provided in Section 5.2.2.

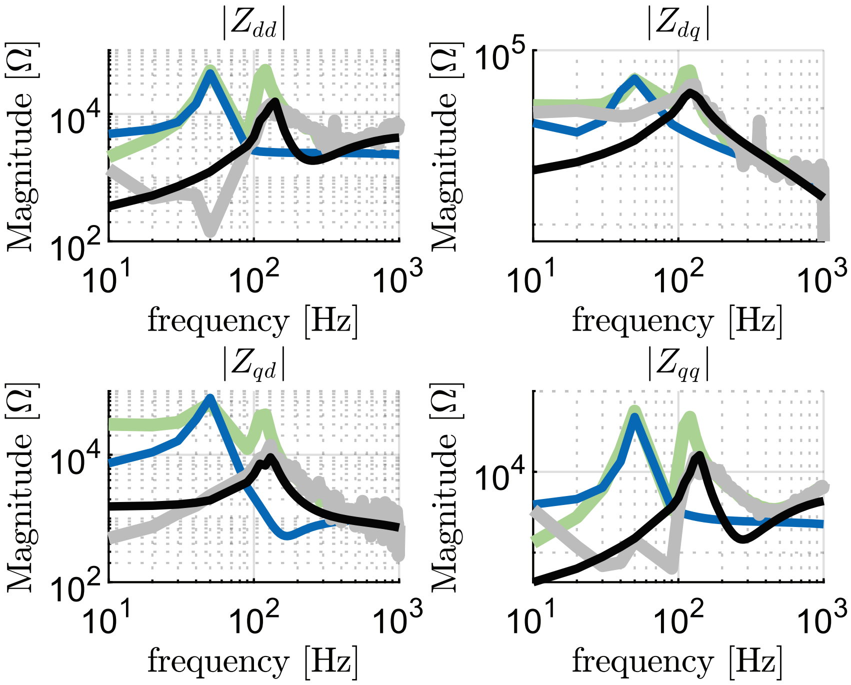

Figure 5.6: Impedance frequency response for MMC STATCOM: in grey the measured datapoints using the frequency sweep method for the detailed model and in green for the average model, together with their LTI vector fitting results in solid black and solid blue lines respectively.

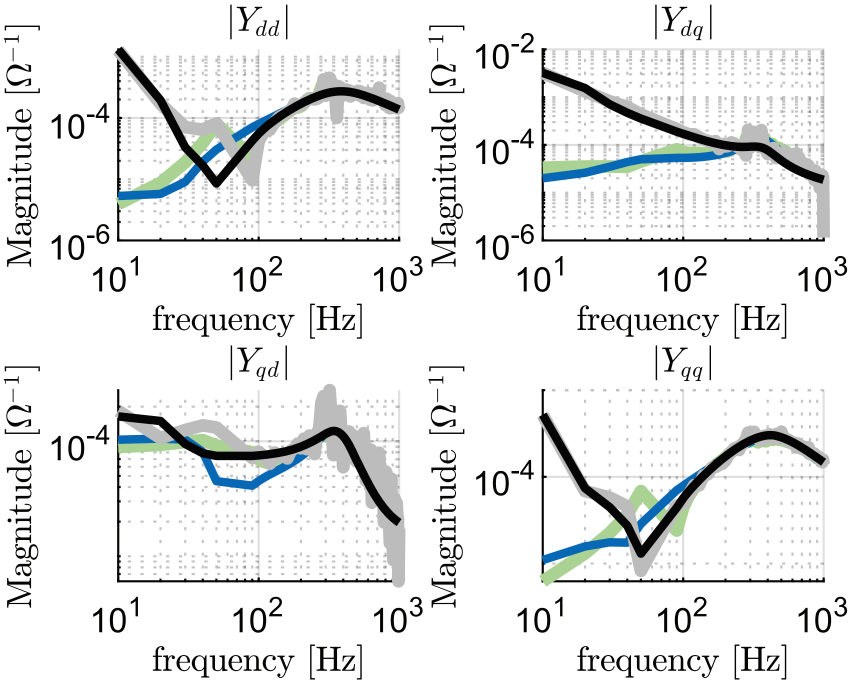

Figure 5.7: Admittance frequency response for MMC STATCOM: in grey the measured datapoints using the frequency sweep method for the detailed model and in green for the average model, together with their LTI vector fitting results in solid black and solid blue lines respectively.

Using the LTI representations of both the detailed and average models, their stability boundaries can be computed for different values of the short-circuit ratio (SCR) and X/R ratio of the grid at the PCC. The stability boundary is useful for TNOs when assessing the risk of instability for converter-based devices due to an unexpected change in the short-circuit level or X/R ratio of the grid at the PCC, which typically happens after the clearance of a transmission line following a fault event. The stability boundary is computed in a similar way as done in the vector fitting technique shown in Figure 5.3, by varying the values of the equivalent grid's inductance L_{th} and resistance R_{th} according to the SCR and X/R ratio desired to check defined as inputs. The SCR and X/R ratio would be defined based on prior knowledge of the system, i.e. its topology and plausible planned and unplanned outages/fault scenarios. For each value, the poles of the transfer function $H(s)$ as defined in equation (5.13) are computed. The L_{th}-R_{th} pair is then classified as a stable or unstable operating condition depending on the presence of poles with positive real part. The stability boundary regions for both models are shown in Figure 5.8. As it is possible to see from Figure 5.8, the average model greatly overestimates the stability boundary of the MMC STATCOM module, having the same control parameters as the detailed model but only considering the PLL and current control loops. It is also worth noting that for high SCR values, the average model will lead similar results to the detailed model and so in these conditions it would be enough for stability analysis.

To validate the stability boundaries shown in in Figure 5.8, time domain simulations are performed in PSCAD and shown in Figure 5.9. The MMC STATCOM module is operating in steady-state condition with a short-circuit ratio (SCR) of 4.5 and an X/R ratio of 15. In the simulation for operating point 2, at 0.2 s the SCR is decreased to 0.335 as defined in Figure 5.8. As it is possible to see, in this case the system is able to reach a new steady-state marginally stable condition with poorly damped oscillations that persist in the voltage and power signals. In the simulation for operating point 1, at 0.2 s the SCR is decreased from 4.5 to 0.327, which initially triggers poorly damped oscillations which eventually drive the system to becoming unstable after 1.3 s, thus representing a marginally unstable operating condition. It is also worth noting that the stability boundary computed considering the average model considers both operating condition as stable, which highlights the need to consider the full detailed model.

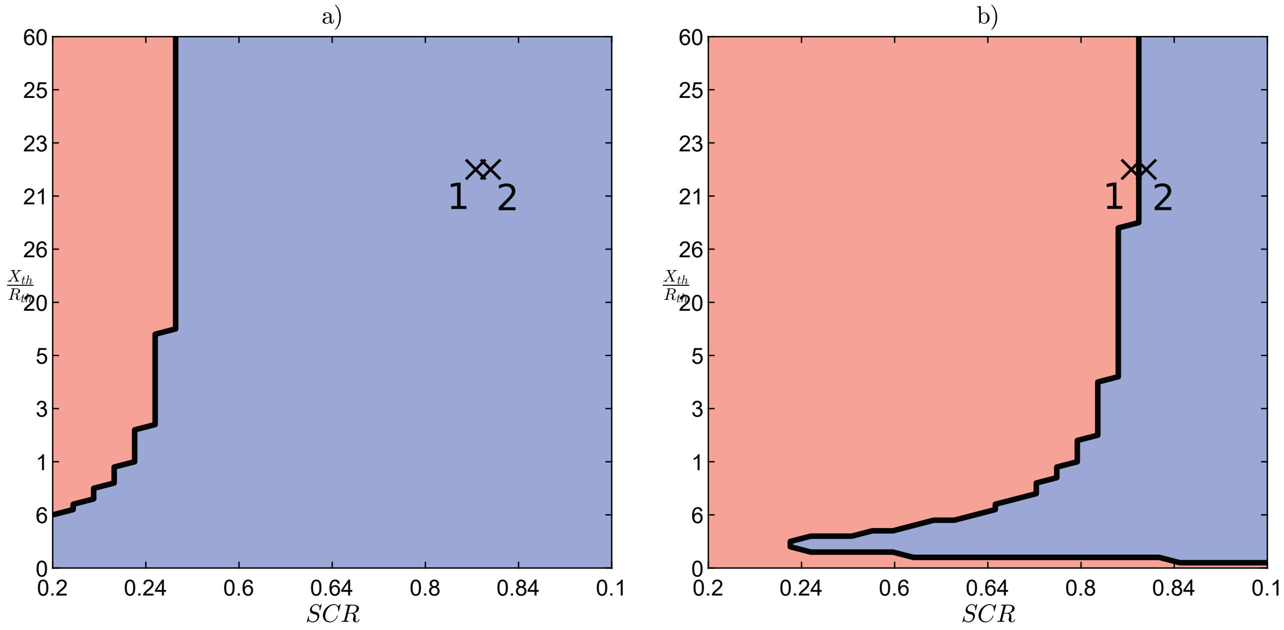

Figure 5.8: Stability boundary for a) average and b) detailed MMC STATCOM models respectively. In red unstable operating region, in blue stable operating region.

It is important to note that the LTI model obtained using the proposed methodology remains accurate only within the vicinity of the operating condition under which the impedance/admittance behaviour was measured during the frequency sweep. Indeed, if the stability boundary of the converter is to be computed accurately, the frequency sweep measurement should be performed in an operating condition close to the boundary. While in most cases the stability boundary is unknown, it can be computed by using the proposed methodology iteratively. First, an initial guess of the stability boundary can be computed by considering the LTI model obtained with measurements on a standard operating condition or any other stable operating condition. Then, a more accurate prediction can be obtained by repeating the methodology but considering the measurements done on an operating condition close to the currently predicted boundary. By repeating this process iteratively and updating the stability boundary each step, an accurate estimation together with an accurate LTI model on its vicinity can be achieved. In the authors experience 2 or 3 iterations are sufficient to have accurate models and predictions.

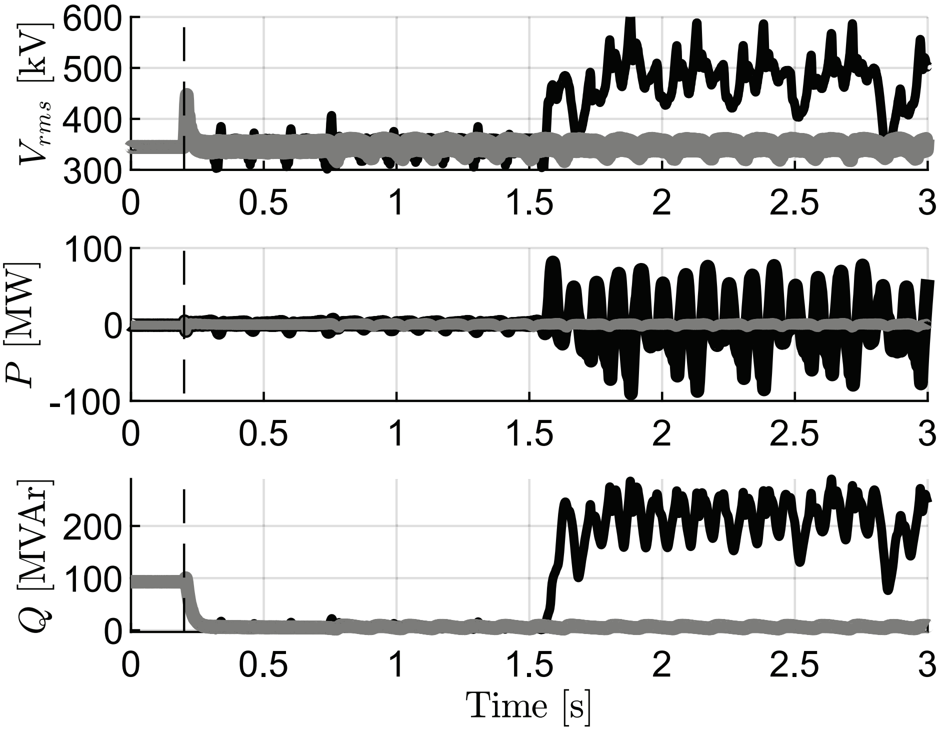

Figure 5.9: Time-domain simulations in PSCAD for a sudden change in short-circuit level considering the MMC STATCOM mode: in grey for operating condition 2 and in black for operating condition 1.

5.4.2 Scenario 1 stability analysis

In scenario 1, a 200 MVA windfarm model is connected to Bus 29, providing 200 MW to the system. Its stability margin is computed for different values of the short-circuit level S_{SC} of the grid at busbar 26, the boundary busbar of subsystem 2 to the rest of the grid. The goal is to identify at which short-circuit level the VSC aggregated windfarm model loses stability. First, the frequency response of the windfarm model is measured in the dq domain as per the methodology presented in Section 5.2.1. From these measurements, an LTI representation is obtained using the vector fitting technique using the methodology presented in Section 5.2.2., the results are shown for the magnitude of its admittance response in Figure 5.10.

Using the LTI representation of the windfarm, a state-space representation of subsystem 2 is obtained by reducing the rest of the grid by its short-circuit Thévenin equivalent at busbar 26. The original value starts at 3700 MVA, and it is reduced progressively by scaling the grid's Thévenin impedance Z_{th} at busbar 26 while keeping the voltage at the busbar constant. For

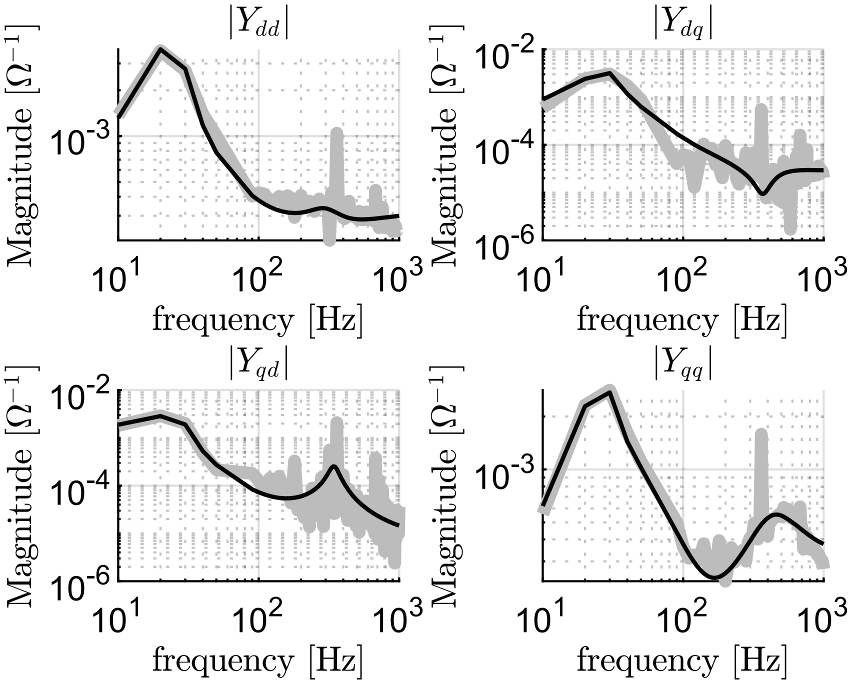

Figure 5.10: Admittance frequency response for windfarm: in grey the measured data-points using the frequency sweep method, together with its LTI vector fitting results in solid black line.

each value of the grid's short-circuit level S_{SC}, eigenvalue analysis is performed on the system dynamic matrix A_{sys} to identify possible unstable operations, i.e. poles with positive real part. The system's eigenvalue loci of interest are plotted in Figure 5.11. As it is possible to see from Figure 5.11, once the short-circuit level drops below 620 MVA, the windfarm can no longer remain stable.

The eigenvalue analysis is validated by performing time-domain simulations in PSCAD. The simulation are performed on the reduced 3 Bus system using the grid's Thévening equivalent, since modifying the short-circuit level on the original 39 Bus system by changing the operating point and topology is cumbersome. The results for short-circuit levels of 620 and 530 MVA are shown in Figure 5.12. Initially, the system is ramped-up to the steady-state operating condition and at time 0.5 s the windfarm model is deblocked, switching from zero output powers to its full detailed model at rated operating conditions. As it is possible to see from Figure 5.12, the eigenvalue analysis considering the proposed LTI admittance modelling of the windfarm model accurately predicts the loss of stable operation once the short-circuit level drops to 530

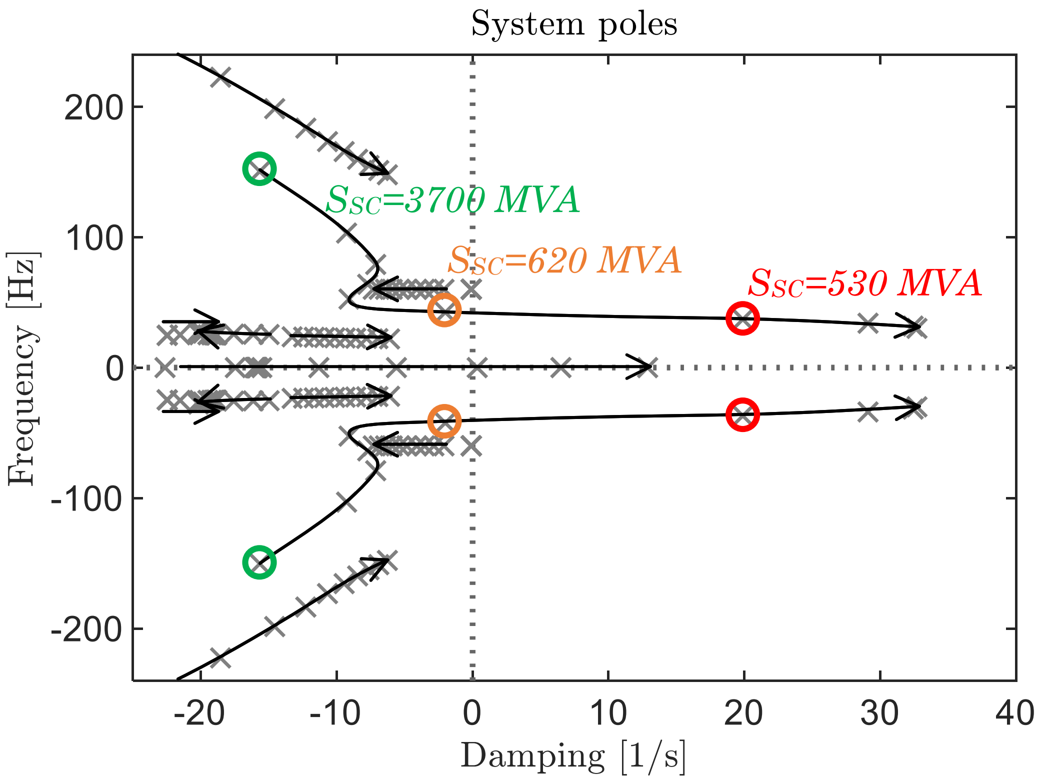

Figure 5.11: 3 Bus system pole loci for different short-circuit levels of the grid at bus 26.

MVA. For a grid strength of 620 MVA, the windfarm is able to transition into its steady-state operation with a poor dynamic response since there is a pair of poorly damped modes. Once the grid strength drops to 530 MVA, the windfarm is not able to transition into a stable steady-state operation.

5.4.3 Scenario 2 stability analysis

Once again, the proposed stability assessment methodology is applied to the reduced 3 Bus system, now incorporating the impedance LTI model of the MMC STATCOM. More specifically, the STATCOM module is operating in AC voltage control mode, injecting 100 MVAr to the grid at bus 28. The windfarm model is operating by injecting 200 MW to the grid at bus 29. A sensitivity analysis is performed on the proportional gain K_p of the AC outer voltage control loop of the STATCOM module. The gain K_p is varied from its base value of 0.5 to 1, 2, 6, 10 and 20 in 6 different cases. For each gain value, a different LTI impedance model of the STATCOM is computed, i.e. a frequency sweep is performed, together with the vector fitting

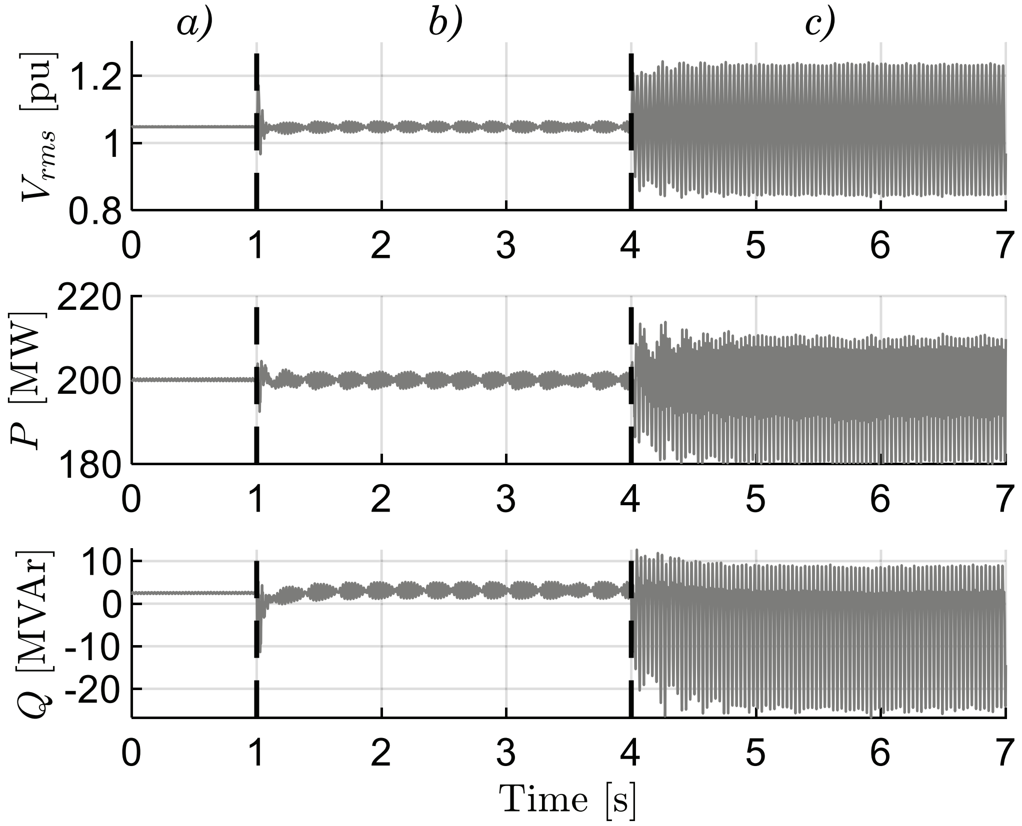

Figure 5.12: Time-domain simulations in PSCAD for: a) $S_{sc} = 3,700$ MVA, b) $S_{sc} = 620$ MVA and c) $S_{sc} = 530$ MVA

identification procedure and its associated state-space modelling is calculated. In each case, the 3 bus system's dynamic matrix A_{sys} is computed and the poles of the system are identified using eigenvalue analysis. The poles' loci of interest are shown in Figure 5.13 where it is possible to see that once the proportional gain K_p increases to a value of 6, unstable operation should be expected.

To validate the results obtained using the proposed stability assessment methodology, time-domain simulations are performed on the entire 39 Bus system. The results for a proportional gain of 2 and 6 are shown in Figure 5.14. The simulation is started from a steady-state condition with a proportional gain of $K_p = 0.5$, and at 0.5 s it is switched to $K_p = 6$ and $K_p = 2$ for the grey and black plots respectively. As it is possible to see from Figure 5.14, when switching to a proportional gain of 2, the system is able to remain in steady-state operation and no significant change is seen in the outputs of the windfarm and STATCOM modules. Once the gain is increased to 6 however, stability is lost and both the STATCOM and windfarm are unable to control its output voltage and reactive power correctly.

It is worth noting that, since both the windfarm and STATCOM modules are stable independently, which is a condition necessary to perform the frequency sweep measurements, they are unstable when interconnected and the proportional gain is increased to 6. This is thus an unstable behaviour due to control interactions between the STATCOM module and windfarm model in close proximity. This is further verified when considering the participation factors of each model to the unstable mode, computed from the dynamic matrix A_{sys}, as shown in Figure 5.15. As it is possible to see from Figure 5.15, as the proportional gain increases and the dynamics performance worsens, both the STATCOM and windfarm model contribute to the unstable mode. While the contribution of the windfarm remains rather constant, the STATCOM's contribution increases with the AC gain as expected, since it is driving the unstable voltage behaviour. This analysis can be further disaggregated by each dq component contribution as shown in Figure 5.16 for the case of a STATCOM for different values of the AC voltage gain. As it is possible to see from Figure 5.16, the main contribution to the unstable mode from the MMC STATCOM comes from its Y_{dq} component, which has the most significant increase in its participation factor as the AC proportional gain increases and the dynamic performance worsens. This is expected, since the vector control strategy in both the MMC STATCOM and windfarm modules use the q component of the voltage to control reactive power injection to the system. More specifically, the main contribution of the STATCOM module for a proportional gain of $K_p = 6$ comes from a state with an associated pole $p_1 = -55.78 \pm j109.9$ and a participation factor of 1.26% from its admittance LTI representation. This pole p_1 has thus associated frequencies in the dq domain of 17.5 Hz, smaller than $2f_0$ which in turn means that the corresponding states have a dynamic response in the subsynchronous frequency band as defined in [106]. As explained in detail in [106], these subsynchronous frequencies are associated with the converters' AC voltage control loop, which validates the results obtained from the eigenvalue and participation factor analysis performed using the proposed impedance-based stability assessment methodology.

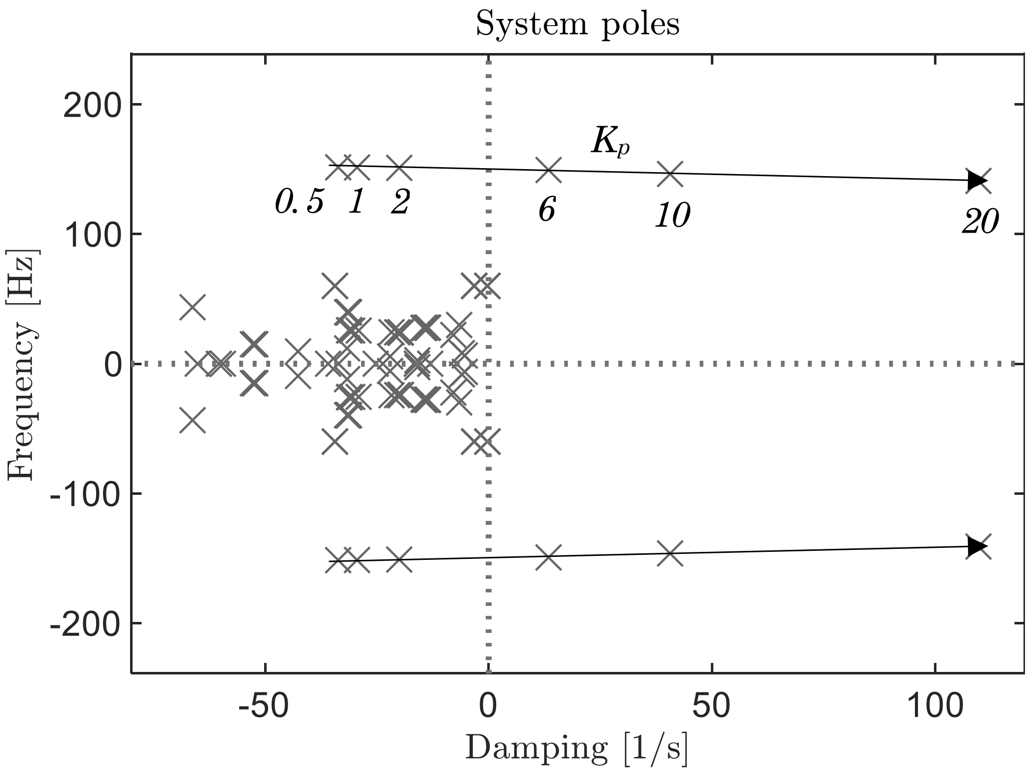

Figure 5.13: 3 Bus system pole loci for different STATCOM AC voltage proportional gains K_p.

5.5 Discussion

In this Chapter, a comprehensive impedance-based stability assessment methodology for power system with converter-based devices is proposed. The methodology aims to fill the gap between impedance-based models and state-space representations for converter-based devices. This in turn provides a method to assess the risk of possible unstable operation for black-box converter models.

The proposed methodology describes how to obtain an LTI representation of the converter's dynamics based on frequency response measurements. This is achieved by using the vector fitting algorithm on the impedance frequency response of the converter, measured using a frequency sweep technique. Using the LTI representation obtained from the vector fitting technique, a circuit realization using RLC branches is constructed, which can in turn be incorporated in the state-space model of a larger network. Using this state-space representation, dynamic operation can be assessed using traditional eigenvalue analysis and participation factor computation. The proposed methodology is able to handle both average and detailed models of both a aggregated

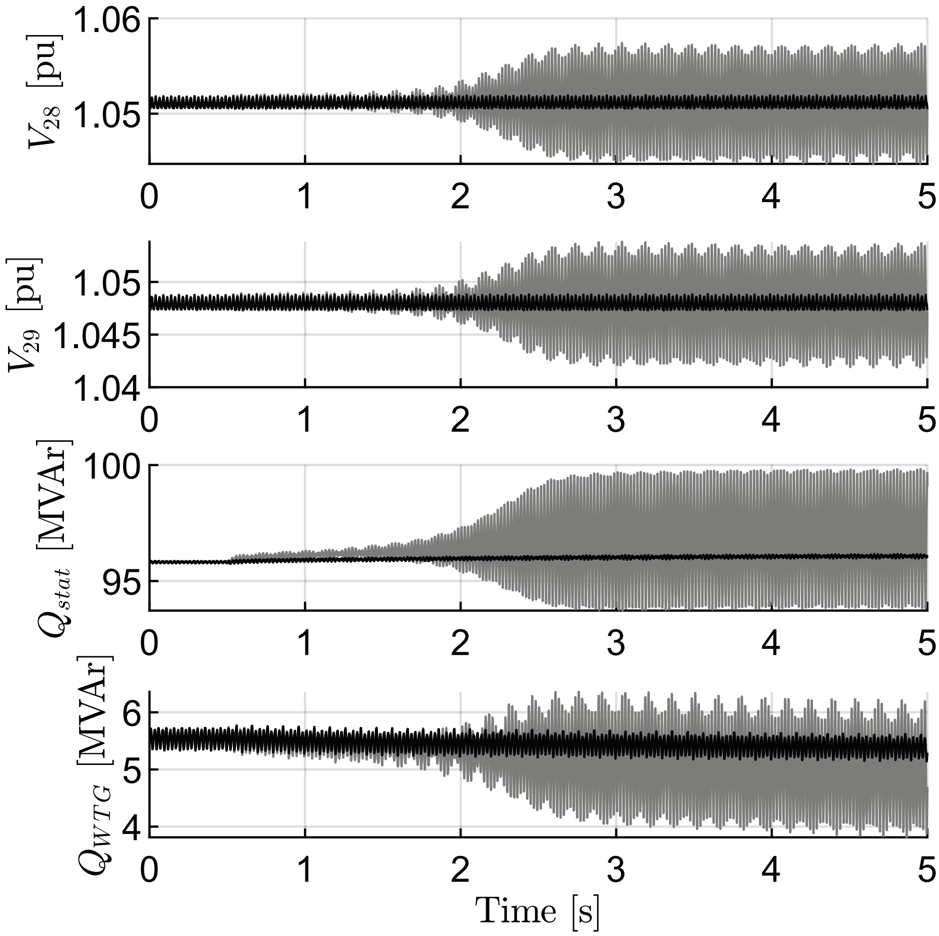

Figure 5.14: Time-domain simulations in PSCAD: in grey for a STATCOM AC voltage proportional gain $K_p = 6$; in solid black line $K_p = 2$.

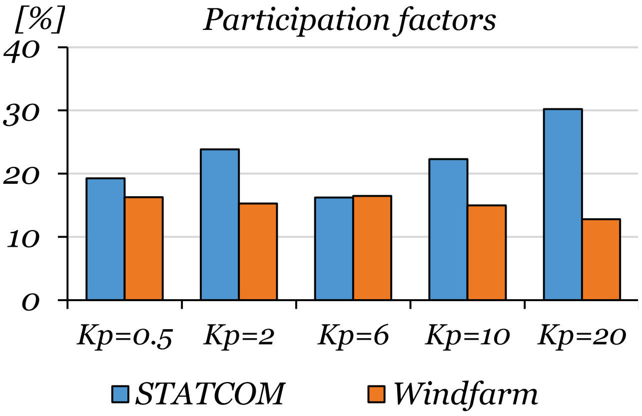

Figure 5.15: Participation factors for different STATCOM AC voltage proportional gains K_p.

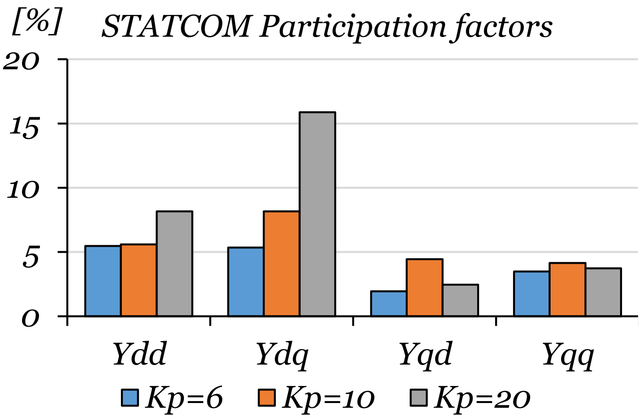

Figure 5.16: Participation factors for STATCOM and windfarm dq components, for a STATCOM AC voltage gain $K_p = 6$.

VSC windfarm model and an MMC STATCOM module. The methodology is validated with EMT time-domain simulation in PSCAD on the 39 Bus New England System, considering detailed VSC windfarm and MMC STATCOM models.

The proposed impedance/admittance model is able to accurately capture the converter-based devices' dynamic behaviour. This in turn provides an LTI representation of converter-based devices which could be used in conjunction with the proposed fault location methodology. More specifically, the proposed impedance/admittance model of converter-based devices could be incorporated in the LTI representation of the grid in the offline characterization stage in order to predict the intermediate frequency content of the system's transient response during fault events. The major limitation at this point to establishing a complete fault location methodology for realistic power systems is to develop the offline characterization in a common reference frame for all elements. Currently, the proposed impedance modelling of cable/line sections is defined in the modal domain, while the LTI admittance modelling of power converters is done in the dq reference frame. The next major research milestone as future work is thus to unify these models in a unique LTI representation, in the phase, modal or dq reference frame.

CHAPTER 6

Conclusions

6.1 Summary of Thesis Achievements

Currently, there is no universal agreement for a truly applicable and reliable solution to the fault location problem in distribution and transmission systems. This is evident in the fact that there are no widely spread fault location methodologies available in transmission or distribution grid protection schemes. The lack of a definitive solution comes from unresolved drawbacks of current available techniques, namely impedance-based solutions or travelling wave methods. In both cases, voltage and current measurement devices are necessary across the network. In the case of travelling wave methods, these measurements devices must be synchronized and have high sampling frequencies, which translates in higher costs which are prohibitive for TNOs and DNOs. In the case of impedance-based approaches, multiple fault location solutions may arise which is prevented at the cost of installing several redundant measurement devices across the network.

This work proposes a novel fault location methodology based on the grid's transient intermediate frequency response. The fundamental idea is to use the grid's natural response to a switching event such as a fault in the network. Each cable/line section in the network has a natural frequency of oscillation depending on its electrical parameters and length. Assuming the electrical parameters of the grid are known and fixed, a fault event can be understood as a partitioning of the grid at the location of the fault occurrence. This will in turn create a transient behaviour defined by the natural oscillatory behaviour of the cable/line sections in the system. The frequencies of oscillations defining the transient response will be thus dependent on which cable/line section is faulted, as well as the fault location within said section. By estimating the frequency spectrum of the transient response for different fault location scenarios via offline simulations, it is thus possible to identify the faulted section and subsequently the fault location in real-time. This can be achieved by matching the measured frequency spectrum of real-time transient voltage/current measurements in the grid with the intermediate frequencies estimated previously in the offline simulation stage.

The first step to perform the fault location using the grid's transient intermediate frequency response, is to estimate the frequency spectrum for different fault location scenarios. This can be achieved in several ways, either by using time-domain simulation softwares or by establishing an analytical formulation of the grid's transient response. As has been shown in this work, when using the intermediate frequency behaviour of the grid, it is important to consider in this stage the frequency-dependent and distributed nature of the electrical parameters for cable/lines sections to obtain accurate fault location predictions. To achieve this, a new LTI impedance representation of cable/line sections is proposed in this work, based the universal line model formulation used in most EMT softwares in the modal domain. The proposed LTI representation provides a Π-circuit representation of each cable/line section, formed by series and parallel branches of RLC circuits. This representation provides good accuracy in representing the frequency-dependent behaviour up to the kHz range, and it is thus an important tool to represent the intermediate frequency transient behaviour of the grid during fault events.

Using the proposed LTI representation of cable/line sections, an offline methodology is developed to identify the intermediate frequencies present in the transient response of the grid during a fault event. This is achieved by establishing the state-space formulation of the grid's transient response for different fault location scenarios. For each fault location scenario within a given section, the intermediate frequencies present in the grid's transient response are identified from the state-space representation. Once the intermediate frequencies have been estimated for all fault location scenarios within a given cable/line section, each intermediate frequency's dependency on the fault location is fitted using a polynomial regression. This polynomial regression provides an analytical characterization of the transient response's frequency spectrum dependency on the fault location and can be stored as a set of polynomial coefficient to be used in the online fault location process. As opposed to using time-domain simulation, the proposed offline methodology can be performed in parallel for each cable/line section in the grid, allowing it to scale as the number of cable/line sections in the system increases.

To perform the fault location in real time, an online methodology is proposed. Using either voltage or current measurements of the grid's transient response immediately after a fault event, it is possible to identify its intermediate frequencies. This can be achieved by using standard signal processing technique such as the Fast Fourier Transform and peak identification algorithms. Once the intermediate frequencies of the transient response have been identified, they are used to solve the polynomial equations characterizing the fault location dependency of the intermediate frequencies for different fault location scenarios. When considering the polynomial equations of the faulted section, a cluster of estimated fault location solutions will exist in the neighbourhood of the unknown real fault location. When using the polynomial equations of other non-faulted sections such a cluster of solutions will not exist. This in turn allows to identify the fault section and estimate the fault location within such section. The proposed methodologies were tested in a 11 kV underground cable distribution system implemented in PSCAD. The frequency-dependent model of underground cables was considered, together with realistic load and transformer models. The accuracy of the proposed fault location methodology was verified for different fault location scenarios, including different faulted sections and fault impedances. The proposed methodologies provided accurate results in all fault scenarios, and thus allows to confirm that the intermediate frequency transient response can be used to effectively to solve the fault location problem. This in turn opens a new research possibility to further improve the proposed technique into a feasible alternative for modern distribution and transmission networks.

Finally, with the objective of extending the proposed fault location methodology to modern power systems, the LTI modelling of converter-based devices is tackled in this work. Similar to the proposed cable/line impedance modelling using RLC branches computed form rational approximations, an admittance representation of power converter in the dq domain is presented. The admittance representation is valid for black-box converter models, where their dynamic behaviour if measured using frequency sweep techniques and approximated using the vector fitting algorithm. The computed admittance representation is able to accurately predict the transient behaviour of power converter and thus is a promising tool to incorporate them in the proposed fault location methodology, as well as to use them for power system stability and security assessment studies.

6.2 Future Work

One of the core elements of this work, and the proposed fault location methodology, is the LTI representation and modelling of power system element. From cable/line sections to converter-based devices, the proposed methodology leverages on their impedance/admittance LTI representation to compute the predicted system's transient frequency response to fault events. Using this approach, the proposed fault location methodology remains scalable for real system, without the need to use computationally expensive EMT simulations. Three major research questions remain open for future research in order to have a complete and accurate fault location methodology based on the system's transient intermediate frequencies:

- To unify the LTI impedance/admittance representations in a common reference frame, whether it is the phase, modal or *dq* domains. The proposed work provides LTI representation of cable/line section in the modal domain, which in turn needs to be extended to the phase domain for maximum accuracy, particularly when considering underground cable with different geometric configurations. In the case of power converters, the proposed LTI model is in the *dq* domain and further research needs to be performed in order to incorporate its behaviour under unbalanced operation.

- To reduce the computational burden of the proposed fault location methodology, further order reduction techniques should be tested on its LTI representation. It is worth exploring whether or not it is possible to reduce the order of the grid's LTI model without significantly impacting its accuracy and intermediate frequency content prediction. By reducing the model order, the computational cost of predicting the system's transient frequency response could be greatly reduced, contributing to the methodology's scalability and applicability.

- Similarly, it is worth exploring if grid partitioning and reduction techniques could be applied to compute the system's LTI representation. It is common practice in stability assessment studies to only simulate in detail the sub-system of interest while keeping a simplified representation of the rest of the grid. A similar approach could be useful when computing a large system's transient frequency response during the offline characterization stage, where electrically distant cable/line sections and power converters have little to no impact on the transient behaviour of different fault location scenarios.

Bibliography

[1] The Gas and Electricity Markets Authority, “The Electricity (Standards of Performance) Regulations 2015 (SI 2015/699),” http://www.legislation.gov.uk/uksi/2015/699/made, 2015.

[2] A. Bahmanyar, S. Jamali, A. Estebsari, and E. Bompard, “A comparison framework for distribution system outage and fault location methods,” *Electric Power Systems Research*, vol. 145, pp. 19 – 34, 2017.

[3] S. Gururajapathy, H. Mokhlis, and H. Illias, “Fault location and detection techniques in power distribution systems with distributed generation: A review,” *Renewable and Sustainable Energy Reviews*, vol. 74, pp. 949 – 958, 2017.

[4] M. Shafiullah and M. A. Abido, “A review on distribution grid fault location techniques,” *Electric Power Components and Systems*, vol. 45, no. 8, pp. 807–824, 2017.

[5] T. O. of Gas and E. Markets, “Guide to the RIIO-ED1 electricity distribution price control,” The Office of Gas and Electricity Markets, Tech. Rep., 2017. [Online]. Available: https://www.ofgem.gov.uk/system/files/docs/2017/01/guide_to_riioed1.pdf

[6] ——, “RIIO-ED1 Annual Report 2016-17,” The Office of Gas and Electricity Markets, Tech. Rep., 2017. [Online]. Available: https://www.ofgem.gov.uk/system/files/docs/2017/12/riio-ed1_annual_report_2016-17.pdf

[7] ——, “Electricity distribution company performance 2010 to 2015,” The Office of Gas and Electricity Markets, Tech. Rep., 2015. [Online]. Available: https://www.ofgem.gov.uk/sites/default/files/docs/electricity_distribution_company_performance_2010-2015.pdf

[8] The Gas and Electricity Markets Authority, “Quality of Service Incentives,” https://www.ofgem.gov.uk/electricity/distribution-networks/network-price-controls/quality-service/quality-service-incentives.

[9] B. Clegg and N. G. Lord, “Modern cable-fault-location methods,” *Proceedings of the Institution of Electrical Engineers*, vol. 122, no. 4, pp. 395–402, 1975.

[10] F. Shen, Q. Wu, and Y. Xue, “Review of service restoration for distribution networks,” *Journal of Modern Power Systems and Clean Energy*, vol. 8, no. 1, pp. 1–14, 2020.

[11] A. Farughian, L. Kumpulainen, and K. Kauhaniemi, “Review of methodologies for earth fault indication and location in compensated and unearthed MV distribution networks,” *Electric Power Systems Research*, vol. 154, pp. 373 – 380, 2018.

[12] E. Personal, A. García, A. Parejo, D. F. Larios, F. Biscarri, and C. León, “A Comparison of Impedance-Based Fault Location Methods for Power Underground Distribution Systems,” *Energies*, vol. 9, no. 12, 2016.

[13] J. Mora-Flórez, J. Meléndez, and G. Carrillo-Caicedo, “Comparison of impedance based fault location methods for power distribution systems,” *Electric Power Systems Research*, vol. 78, no. 4, pp. 657 – 666, 2008.

[14] C. Orozco-Henao, A. Bretas, A. Herrera-Orozco, J. D. Pulgarín-Rivera, S. Dhulipala, and S. Wang, “Towards active distribution networks fault location: Contributions considering DER analytical models and local measurements,” *International Journal of Electrical Power & Energy Systems*, vol. 99, pp. 454 – 464, 2018.

[15] S. Zhang, S. Lin, Z. He, and W. j. Lee, “Ground fault location in radial distribution networks involving distributed voltage measurement,” *IET Generation, Transmission Distribution*, vol. 12, no. 4, pp. 987–996, February 2018.

[16] P. Wang, B. Chen, H. Zhou, T. Cuihua, and B. Sun, "Fault location in resonant grounded network by adaptive control of neutral-to-earth complex impedance," *IEEE Transactions on Power Delivery*, vol. 33, no. 2, pp. 689–698, April 2018.

[17] H. Cifuentes-Chaves, J. Mora-Flúrez, and S. Pérez-Londoño, "Time domain analysis for fault location in power distribution systems considering the load dynamics," *Electric Power Systems Research*, vol. 146, pp. 331 – 340, 2017.

[18] K. Jia, Z. Ren, L. Li, Z. Xuan, and D. Thomas, "High-frequency transient comparison based fault location in distribution systems with DGs," *IET Generation, Transmission Distribution*, vol. 11, no. 16, pp. 4068–4077, November 2017.

[19] A. Bahmanyar and S. Jamali, "Fault location in active distribution networks using non-synchronized measurements," *International Journal of Electrical Power & Energy Systems*, vol. 93, pp. 451 – 458, 2017.

[20] M. Salehi and F. Namdari, "Fault location on branched networks using mathematical morphology," *IET Generation, Transmission Distribution*, vol. 12, no. 1, pp. 207–216, February 2018.

[21] Y. Xi, Z. Li, X. Zeng, X. Tang, X. Zhang, and H. Xiao, "Fault location based on travelling wave identification using an adaptive extended Kalman filter," *IET Generation, Transmission Distribution*, vol. 12, no. 6, pp. 1314–1322, March 2018.

[22] M. Goudarzi, B. Vahidi, R. Naghizadeh, and S. Hosseinian, "Improved fault location algorithm for radial distribution systems with discrete and continuous wavelet analysis," *International Journal of Electrical Power & Energy Systems*, vol. 67, pp. 423 – 430, 2015.

[23] A. Borghetti, M. Bosetti, C. A. Nucci, M. Paolone, and A. Abur, "Integrated Use of Time-Frequency Wavelet Decompositions for Fault Location in Distribution Networks: Theory and Experimental Validation," *IEEE Transactions on Power Delivery*, vol. 25, no. 4, pp. 3139–3146, Oct 2010.

[24] A. Borghetti, M. Bosetti, M. D. Silvestro, C. A. Nucci, and M. Paolone, "Continuous-Wavelet Transform for Fault Location in Distribution Power Networks: Definition of

Mother Wavelets Inferred From Fault Originated Transients," *IEEE Transactions on Power Systems*, vol. 23, no. 2, pp. 380–388, May 2008.

[25] C. Y. Evrenosoglu and A. Abur, "Travelling wave based fault location for teed circuits," *IEEE Transactions on Power Delivery*, vol. 20, no. 2, pp. 1115–1121, April 2005.

[26] P. E. Farias, A. P. de Morais, J. P. Rossini, and G. Cardoso, "Non-linear high impedance fault distance estimation in power distribution systems: A continually online-trained neural network approach," *Electric Power Systems Research*, vol. 157, pp. 20 – 28, 2018.

[27] I. M. Karmacharya and R. Gokaraju, "Fault Location in Ungrounded Photovoltaic System Using Wavelets and ANN," *IEEE Transactions on Power Delivery*, vol. 33, no. 2, pp. 549–559, April 2018.

[28] M. Shafiullah, M. A. Abido, and Z. Al-Hamouz, "Wavelet-based extreme learning machine for distribution grid fault location," *IET Generation, Transmission Distribution*, vol. 11, no. 17, pp. 4256–4263, December 2017.

[29] F. Dehghani, F. Khodnia, and E. Dehghan, "Fault location of unbalanced power distribution feeder with distributed generation using neural networks," *CIRED - Open Access Proceedings Journal*, vol. 2017, no. 1, pp. 1134–1137, October 2017.

[30] F. Zhang, Q. Liu, Y. Liu, N. Tong, S. Chen, and C. Zhang, "Novel fault location method for power systems based on attention mechanism and double structure gru neural network," *IEEE Access*, vol. 8, pp. 75 237–75 248, 2020.

[31] D. Guillen, C. Salas, L. Fernando Sanchez-Gomez, and L. M. Castro, "Enhancement of dynamic phasor estimation-based fault location algorithms for ac transmission lines," *IET Generation, Transmission and Distribution*, vol. 14, no. 6, pp. 1091–1103, 2020.

[32] L. Xie, L. Luo, Y. Li, Y. Zhang, and Y. Cao, "A traveling wave-based fault location method employing vmd-teo for distribution network," *IEEE Trans. Power Del.*, vol. 35, no. 4, pp. 1987–1998, 2020.

[33] R. Liang, N. Peng, L. Zhou, X. Meng, Y. Hu, Y. Shen, and X. Xue, “Fault location method in power network by applying accurate information of arrival time differences of modal traveling waves,” *IEEE Transactions on Industrial Informatics*, vol. 16, no. 5, pp. 3124–3132, 2020.

[34] S. Shi, B. Zhu, A. Lei, and X. Dong, “Fault location for radial distribution network via topology and reclosure-generating traveling waves,” *IEEE Trans. Smart Grid*, vol. 10, no. 6, pp. 6404–6413, 2019.

[35] Y. Xi, Y. Cui, X. Tang, Z. Li, and X. Zeng, “Fault location of lightning strikes using residual analysis based on an adaptive kalman filter,” *IEEE Access*, vol. 7, pp. 88 126–88 137, 2019.

[36] A. Ahmadimanesh and S. M. Shahrtash, “Transient-based fault-location method for multiterminal lines employing s-transform,” *IEEE Trans. Power Del.*, vol. 28, no. 3, pp. 1373–1380, 2013.

[37] Y. Jiang, “Data-driven fault location of electric power distribution systems with distributed generation,” *IEEE Trans. Smart Grid*, vol. 11, no. 1, pp. 129–137, 2020.

[38] K. Chen, J. Hu, Y. Zhang, Z. Yu, and J. He, “Fault location in power distribution systems via deep graph convolutional networks,” *IEEE Journal on Selected Areas in Communications*, vol. 38, no. 1, pp. 119–131, 2020.

[39] W. Li, D. Deka, M. Chertkov, and M. Wang, “Real-time faulted line localization and pmu placement in power systems through convolutional neural networks,” *IEEE Trans. Power Syst.*, vol. 34, no. 6, pp. 4640–4651, 2019.

[40] M. F. Islam, A. M. T. Oo, and S. A. Azad, “Locating underground cable faults: A review and guideline for new development,” in *2012 22nd Australasian Universities Power Engineering Conference (AUPEC)*, 2012, pp. 1–5.

[41] T. Short, *Electric Power Distribution Handbook.* CRC Press, 2018. [Online]. Available: https://books.google.co.uk/books?id=qW_OBQAAQBAJ

[42] X. Wang, H. Zhang, F. Shi, Q. Wu, V. Terzija, W. Xie, and C. Fang, “Location of single phase to ground faults in distribution networks based on synchronous transients energy analysis,” *IEEE Trans. Smart Grid*, vol. 11, no. 1, pp. 774–785, 2020.

[43] K. Jia, T. Bi, Z. Ren, D. W. P. Thomas, and M. Sumner, “High frequency impedance based fault location in distribution system with dgs,” *IEEE Trans. Smart Grid*, vol. 9, no. 2, pp. 807–816, 2018.

[44] X. Wang, H. Zhang, F. Shi, W. Xie, P. Ling, and J. Liu, “Transient energy analysis based single-phase-to-ground fault location in distribution networks,” in *2018 2nd IEEE Conference on Energy Internet and Energy System Integration (EI2)*, 2018, pp. 1–4.

[45] “IEEE recommended practice for monitoring electric power quality,” *IEEE Std 1159-2019 (Revision of IEEE Std 1159-2009)*, pp. 1–98, 2019.

[46] “IEEE Guide for Determining Fault Location on AC Transmission and Distribution Lines - Redline,” *IEEE Std C37.114-2014 (Revision of IEEE Std C37.114-2004) - Redline*, pp. 1–128, January 2015.

[47] A. A. Girgis, C. M. Fallon, and D. L. Lubkeman, “A fault location technique for rural distribution feeders,” *IEEE Transactions on Industry Applications*, vol. 29, no. 6, pp. 1170–1175, November 1993.

[48] H. H. Skilling, *Electric transmission lines : distributed constants, theory and applications*, ser. McGraw-Hill electrical and electronic engineering series. New York: McGraw-Hill, 1951.

[49] F. H. Magnago and A. Abur, “Fault location using wavelets,” *IEEE Transactions on Power Delivery*, vol. 13, no. 4, pp. 1475–1480, Oct 1998.

[50] N. L. Johnson, *Continuous univariate distributions*, 2nd ed., ser. Wiley series in probability and mathematical statistics Applied probability and statistics. New York ; Chichester: Wiley, 1994.

[51] J. A. Martinez-Velasco, *Introduction to Electromagnetic Transient Analysis of Power Systems.* IEEE, 2015.

[52] N. Watson and J. Arrillaga, *Power Systems Electromagnetic Transients Simulation*, ser. Energy Engineering. Institution of Engineering and Technology, 2003.

[53] M. Eremia and M. Shahidehpour, *Handbook of Electrical Power System Dynamics: Modeling, Stability and Control.* John Wiley & Sons, Ltd, 2013, ch. 1, pp. 1–6.

[54] A. Semlyen and A. Dabuleanu, "Fast and accurate switching transient calculations on transmission lines with ground return using recursive convolutions," *IEEE Trans. Power App. Syst.*, vol. 94, no. 2, pp. 561–571, March 1975.

[55] J. R. Marti, "Accurate modelling of frequency-dependent transmission lines in electromagnetic transient simulations," *IEEE Trans. Power App. Syst.*, vol. PAS-101, no. 1, pp. 147–157, Jan 1982.

[56] H. V. Nguyen, H. W. Dommel, and J. R. Marti, "Direct phase-domain modelling of frequency-dependent overhead transmission lines," *IEEE Trans. Power Del.*, vol. 12, no. 3, pp. 1335–1342, July 1997.

[57] B. Gustavsen, G. Irwin, R. Mangelrød, D. Brandt, and H. Kent, "Transmission line models for the simulation of interaction phenomena between parallel ac and dc overhead lines," in *International Conference on Power Systems Transients 1999 (IPST 1999)*, June 1999, pp. 61–68.

[58] A. Morched, B. Gustavsen, and M. Tartibi, "A universal model for accurate calculation of electromagnetic transients on overhead lines and underground cables," *IEEE Trans. Power Del.*, vol. 14, no. 3, pp. 1032–1038, July 1999.

[59] B. Gustavsen and A. Semlyen, "Simulation of transmission line transients using vector fitting and modal decomposition," *IEEE Trans. Power Del.*, vol. 13, no. 2, pp. 605–614, April 1998.

[60] ——, “Rational approximation of frequency domain responses by vector fitting,” *IEEE Trans. Power Del.*, vol. 14, no. 3, pp. 1052–1061, July 1999.

[61] B. Gustavsen, “Improving the pole relocating properties of vector fitting,” *IEEE Trans. Power Del.*, vol. 21, no. 3, pp. 1587–1592, July 2006.

[62] D. Deschrijver, M. Mrozowski, T. Dhaene, and D. De Zutter, “Macromodeling of multiport systems using a fast implementation of the vector fitting method,” *IEEE Microwave and Wireless Components Letters*, vol. 18, no. 6, pp. 383–385, June 2008.

[63] A. Semlyen and A. Deri, “Time domain modelling of frequency dependent three-phase transmission line impedance,” *IEEE Trans. Power App. Syst.*, vol. PAS-104, no. 6, pp. 1549–1555, June 1985.

[64] A. Hoshmeh, “A three-phase cable model based on lumped parameters for transient calculations in the time domain,” in *2016 IEEE Innovative Smart Grid Technologies - Asia (ISGT-Asia)*, Nov 2016, pp. 580–585.

[65] J. Beerten, S. DÁrco, and J. A. Suul, “Frequency-dependent cable modelling for small-signal stability analysis of vsc-hvdc systems,” *IET Gener. Transm. Distrib.*, vol. 10, no. 6, pp. 1370–1381, 2016.

[66] P. T. Caballero, S. Kurokawa, and B. Kordi, “Accelerated frequency-dependent method of characteristics for the simulation of multiconductor transmission lines in the time domain,” *Electric Power Systems Research*, vol. 168, pp. 55 – 66, 2019.

[67] G. Antonini, “Spice equivalent circuits of frequency-domain responses,” *IEEE Transactions on Electromagnetic Compatibility*, vol. 45, no. 3, pp. 502–512, Aug 2003.

[68] Q. Huang and V. Vittal, “Advanced emt and phasor-domain hybrid simulation with simulation mode switching capability for transmission and distribution systems,” *IEEE Trans. Power Syst.*, vol. 33, no. 6, pp. 6298–6308, Nov 2018.

[69] M. Cespedes and J. Sun, “Impedance modeling and analysis of grid-connected voltage-source converters,” *IEEE Trans. Power Electron.*, vol. 29, no. 3, pp. 1254–1261, March 2014.

[70] X. Wang, L. Harnefors, and F. Blaabjerg, “Unified impedance model of grid-connected voltage-source converters,” *IEEE Trans. Power Electron.*, vol. 33, no. 2, pp. 1775–1787, Feb 2018.

[71] X. Wang and F. Blaabjerg, “Harmonic stability in power electronic-based power systems: Concept, modeling, and analysis,” *IEEE Transactions on Smart Grid*, vol. 10, no. 3, pp. 2858–2870, May 2019.

[72] S. D’Arco, J. A. Suul, and J. Beerten, “Analysis of accuracy versus model order for frequency-dependent pi-model of hvdc cables,” in *2016 IEEE 17th Workshop on Control and Modeling for Power Electronics (COMPEL)*, 2016, pp. 1–8.

[73] L. Wedepohl and D. Wilcox, “Transient analysis of underground power-transmission systems. system-model and wave-propagation characteristics,” *Proceedings of the Institution of Electrical Engineers*, vol. 120, pp. 253–260(7), February 1973. [Online]. Available: https://digital-library.theiet.org/content/journals/10.1049/piee.1973.0056

[74] J. J. Grainger, *Power system analysis.* McGraw-Hill, 1999.

[75] B. Gustavsen, “Optimal time delay extraction for transmission line modeling,” *IEEE Trans. Power Del.*, vol. 32, no. 1, pp. 45–54, Feb 2017.

[76] I. Kocar and J. Mahseredjian, “Accurate frequency dependent cable model for electromagnetic transients,” *IEEE Trans. Power Del.*, vol. 31, no. 3, pp. 1281–1288, June 2016.

[77] S. L. Varricchio, F. D. Freitas, N. Martins, and F. C. Véliz, “Computation of dominant poles and residue matrices for multivariable transfer functions of infinite power system models,” *IEEE Trans. Power Syst.*, vol. 30, no. 3, pp. 1131–1142, 2015.

[78] N. Martins, C. Portela, and S. Gomes, “Sequential computation of transfer function dominant poles of s-domain system models,” *IEEE Trans. Power Syst.*, vol. 24, no. 2, pp. 776–784, 2009.

[79] D. Karlsson and D. J. Hill, “Modelling and identification of nonlinear dynamic loads in power systems,” *IEEE Transactions on Power Systems*, vol. 9, no. 1, pp. 157–166, 1994.

[80] J. Quintero, V. Vittal, G. T. Heydt, and H. Zhang, “The impact of increased penetration of converter control-based generators on power system modes of oscillation,” *IEEE Transactions on Power Systems*, vol. 29, no. 5, pp. 2248–2256, 2014.

[81] Y. Li, L. Fan, and Z. Miao, “Wind in weak grids: Low-frequency oscillations, subsynchronous oscillations, and torsional interactions,” *IEEE Transactions on Power Systems*, vol. 35, no. 1, pp. 109–118, 2020.

[82] N. Hatziargyriou, J. V. Milanovic, C. Rahmann, V. Ajjarapu, C. Canizares, I. Erlich, D. Hill, I. Hiskens, I. Kamwa, B. Pal, P. Pourbeik, J. J. Sanchez-Gasca, A. M. Stankovic, T. Van Cutsem, V. Vittal, and C. Vournas, “Definition and classification of power system stability revisited extended,” *IEEE Transactions on Power Systems*, pp. 1–1, 2020.

[83] B. Wen, D. Boroyevich, R. Burgos, P. Mattavelli, and Z. Shen, “Analysis of d-q small-signal impedance of grid-tied inverters,” *IEEE Tran.on Power Electron.*, vol. 31, no. 1, pp. 675–687, 2016.

[84] X. Wang, L. Harnefors, and F. Blaabjerg, “Unified impedance model of grid-connected voltage-source converters,” *IEEE Tran.on Power Electron.*, vol. 33, no. 2, pp. 1775–1787, 2018.

[85] C. Li, R. Burgos, B. Wen, Y. Tang, and D. Boroyevich, “Stability analysis of power systems with multiple statcoms in close proximity,” *IEEE Tran.on Power Electron.*, vol. 35, no. 3, pp. 2268–2283, 2020.

[86] Y. Gu, Y. Li, Y. Zhu, and T. C. Green, “Impedance-based whole-system modeling for a composite grid via embedding of frame dynamics,” *IEEE Transactions on Power Systems*, vol. 36, no. 1, pp. 336–345, 2021.

[87] X. Wang, F. Blaabjerg, and P. C. Loh, “Passivity-based stability analysis and damping injection for multiparalleled vscs with lcl filters,” *IEEE Tran.on Power Electron.*, vol. 32, no. 11, pp. 8922–8935, 2017.

[88] M. Cespedes and J. Sun, “Impedance modeling and analysis of grid-connected voltage-source converters,” *IEEE Tran.on Power Electron.*, vol. 29, no. 3, pp. 1254–1261, 2014.

[89] A. Rygg and M. Molinas, “Apparent impedance analysis: A small-signal method for stability analysis of power electronic-based systems,” *IEEE Journal of Emerging and Selected Topics in Power Electronics*, vol. 5, no. 4, pp. 1474–1486, 2017.

[90] A. Rygg, M. Molinas, C. Zhang, and X. Cai, “A modified sequence-domain impedance definition and its equivalence to the dq-domain impedance definition for the stability analysis of ac power electronic systems,” *IEEE Journal of Emerging and Selected Topics in Power Electronics*, vol. 4, no. 4, pp. 1383–1396, 2016.

[91] Y. Li, Y. Gu, Y. Zhu, A. Junyent-Ferré, X. Xiang, and T. C. Green, “Impedance circuit model of grid-forming inverter: Visualizing control algorithms as circuit elements,” *IEEE Tran.on Power Electron.*, vol. 36, no. 3, pp. 3377–3395, 2021.

[92] J. Huang, K. A. Corzine, and M. Belkhayat, “Small-signal impedance measurement of power-electronics-based ac power systems using line-to-line current injection,” *IEEE Trans. Power Electron.*, vol. 24, no. 2, pp. 445–455, 2009.

[93] V. Valdivia, A. Lázaro, A. Barrado, P. Zumel, C. Fernández, and M. Sanz, “Impedance identification procedure of three-phase balanced voltage source inverters based on transient response measurements,” *IEEE Trans. Power Electron.*, vol. 26, no. 12, pp. 3810–3816, 2011.

[94] T. Roinila, T. Messo, and E. Santi, “Mimo-identification techniques for rapid impedance-based stability assessment of three-phase systems in dq domain,” *IEEE Trans. Power Electron.*, vol. 33, no. 5, pp. 4015–4022, 2018.

[95] J. Lyu, X. Zhang, X. Cai, and M. Molinas, “Harmonic state-space based small-signal impedance modeling of a modular multilevel converter with consideration of internal harmonic dynamics,” *IEEE Trans. Power Electron.*, vol. 34, no. 3, pp. 2134–2148, 2019.

[96] J. Kwon, X. Wang, F. Blaabjerg, C. L. Bak, V.-S. Sularea, and C. Busca, “Harmonic interaction analysis in a grid-connected converter using harmonic state-space (hss) modeling,” *IEEE Trans. Power Electron.*, vol. 32, no. 9, pp. 6823–6835, 2017.

[97] M. Amin and M. Molinas, “A gray-box method for stability and controller parameter estimation in hvdc-connected wind farms based on nonparametric impedance,” *IEEE Tran.on Power Electron.*, vol. 66, no. 3, pp. 1872–1882, 2019.

[98] S. Lefteriu and A. C. Antoulas, “On the convergence of the vector-fitting algorithm,” *IEEE Transactions on Microwave Theory and Techniques*, vol. 61, no. 4, pp. 1435–1443, 2013.

[99] Y. Gu, Y. Li, Y. Zhu, and T. C. Green, “Impedance-based whole-system modeling for a composite grid via embedding of frame dynamics,” *IEEE Transactions on Power Systems*, vol. 36, no. 1, pp. 336–345, 2021.

[100] [Online]. Available: https://www.pscad.com/knowledge-base/article/227

[101] E. Cotilla-Sanchez, P. D. H. Hines, C. Barrows, S. Blumsack, and M. Patel, “Multi-attribute partitioning of power networks based on electrical distance,” *IEEE Transactions on Power Systems*, vol. 28, no. 4, pp. 4979–4987, 2013.

[102] I. Tyuryukanov, M. Popov, M. A. M. M. van der Meijden, and V. Terzija, “Discovering clusters in power networks from orthogonal structure of spectral embedding,” *IEEE Transactions on Power Systems*, vol. 33, no. 6, pp. 6441–6451, 2018.

[103] ——, “Slow coherency identification and power system dynamic model reduction by using orthogonal structure of electromechanical eigenvectors,” *IEEE Transactions on Power Systems*, vol. 36, no. 2, pp. 1482–1492, 2021.

[104] [Online]. Available: https://www.pscad.com/knowledge-base/article/234

[105] S. Du, A. Dekka, B. Wu, and N. Zargari, *Modular Multilevel Converters: Analysis, Control, and Applications*, ser. IEEE Press Series on Power and Energy Systems. Wiley, 2018. [Online]. Available: https://books.google.co.uk/books?id=__tQDwAAQBAJ

[106] X. Wang and F. Blaabjerg, “Harmonic stability in power electronic-based power systems: Concept, modeling, and analysis,” *IEEE Transactions on Smart Grid*, vol. 10, no. 3, pp. 2858–2870, 2019.